Université de Montréal

Étude numérique et asymptotique d'une approche couplée pour la simulation de la propagation de feux de forêt avec l'effet du vent en terrain complexe

par

Louis-Xavier Proulx

Département de mathématiques et de statistique
Faculté des arts et des sciences

Thèse présentée en vue de l'obtention du grade de
Philosophiæ Doctor (Ph.D.) en mathématiques,
option mathématiques appliquées

Août 2016

Université de Montréal

Faculté des études supérieures

Cette thèse intitulée

Étude numérique et asymptotique d'une approche couplée pour la simulation de la propagation de feux de forêt avec l'effet du vent en terrain complexe

présentée par

Louis-Xavier Proulx

a été évaluée par un jury composé des personnes suivantes :

Jacques Bélair

(président-rapporteur)

Anne Bourlioux

(directrice de recherche)

Michel Delfour

(membre du jury)

Catherine Mavriplis

(examinatrice externe)

Olivier Blarquez

(représentant du doyen de la FAS)

Thèse acceptée le

8 décembre 2017

SOMMAIRE

L'objet central de cette thèse est le développement d'une nouvelle approche couplée pour la propagation des feux de forêt. Ce modèle est constitué d'un modèle atmosphérique basé sur une seule contrainte pour le vent. Cette contrainte donnée par une équation de divergence est dérivée d'une approximation à faible nombre de Mach. Le modèle pour le feu représente le front sur la topographie comme une interface infiniment mince qui délimite les zones brûlées. La méthode numérique «level set» permet de propager cette interface sur la topographie.

Les modèles pour le feu et l'atmosphère sont couplés à l'aide d'un terme source dans l'équation de divergence qui régit le champ de vitesse du vent. Cette source est représentée par une paire d'une source et d'un puits singuliers afin de représenter les caractéristiques principales de l'écoulement atmosphérique près du feu. Chaque singularité est supportée par une interface, une variété de codimension 2. Le calcul de l'amplitude du terme source est effectué à l'aide de la formule de Byram pour l'intensité du feu. La dérivation et les caractéristiques particulières de ce modèle couplé sont présentées dans cet ouvrage.

Une technique de régularisation et de rééchelonnage pour une fonction delta supportée par une variété de codimension 2 a été développée dans le cadre de ce modèle. Une étude de la convergence des solutions du problème elliptique, associé au modèle atmosphérique, démontre la nécessité de cette technique pour obtenir la convergence.

La thèse présente l'implémentation numérique du modèle couplé. Les simulations réalisées avec le modèle permettent de caractériser les régimes de propagation à l'aide du nombre sans dimension décrit lors de l'analyse dimensionnelle. Le modèle est finalement comparé au modèle Firetec à partir d'expériences numériques de propagation sur des topographies idéalisées.

MOTS-CLÉS : Feux de forêt, atmosphère, modèle couplé, intensité du feu, source de chaleur, plume, interface singulière, fonction delta, régularisation, régimes de propagation.

SUMMARY

The core of this thesis consists in the development of a new coupled model for wildfire spread. This model relies on an atmospheric model based on a single constraint for the wind velocity flow. This constraint given by a divergence equation is derived from a low Mach number approximation. The fire model represents the fireline on the topography as an infinitely thin interface which outlines the burned regions. The level set method allows to track the spread of this interface on the topography.

The fire and atmosphere models are coupled with a source term in the divergence equation governing the wind velocity field. This source is represented as a singular sink-source pair in order to capture the main features of the atmospheric flow near the fireline. Each singularity is supported on an interface, a codimension-2 manifold. The computation of the amplitude of the source term is achieved with Byram's formula for fire intensity. The derivation and particular characteristics of this coupled model are presented in this work.

A regularization technique combined with a rescaling algorithm for a delta function supported on a codimension-2 manifold has been elaborated for this model. A study of the convergence of the solutions of the elliptic problem, associated with the atmospheric model, demonstrates the necessity of this technique to achieve convergence with mesh refinements.

This thesis presents the numerical implementation of the coupled model. The simulations conducted with the model are used to study the fire spread regimes with a dimensionless number obtained in a dimensional analysis. The model is compared to the Firetec model with numerical experiments of fire spread over idealized topographies.

KEYWORDS : Wildfires, Atmosphere, Coupled model, Fire intensity, Heat source, Plume, Singular interface, delta function, Regularization, Spread regimes.

TABLE DES MATIÈRES

LISTE DES TABLEAUX

LISTE DES FIGURES

LISTE DES SIGLES

ANAG : Applied Numerical Algorithms Group
CAWFE : Coupled Atmosphere-Wildland Fire-Environment
DNS : Direct Numerical Simulation
EBM : Embedded Boundary Method
FDS : Fire Dynamics Simulator
HIGRAD : High Gradient flow
LES : Large Eddy Simulation
MAC : Marker-and-Cell
NCAR : National Center for Atmospheric Research
NIST : National Institute of Standards and Technology
PDE : Partial Differential Equation
UU-LES : University of Utah Large Eddy Simulation
WRF : Weather Research and Forecasting Model
WSV : net effective wind speed
WUI : Wildland-urban interface

À mon père, Luc
et ma mère, Lucie

REMERCIEMENTS

Mes premiers remerciements vont tout naturellement à Anne Bourlioux, ma directrice de recherche. Je lui suis entièrement reconnaissant pour tout le soutien académique, moral et financier qu'elle m'a offert lors de mon doctorat. Je la remercie pour ses encouragements à participer aux activités d'enseignement ainsi qu'aux ateliers et conférences. Ceux-ci ont assuré mon développement scientifique et académique.

Je remercie les organismes suivants pour tout le soutien financier sans lequel je n'aurais pu poursuivre des études au doctorat : le Fonds de recherche du Québec - Nature et technologies (FRQNT), la Faculté des études supérieures et postdoctorales (FESP) de l'Université de Montréal et le Centre de recherches mathématiques (CRM).

Je tiens à remercier tous mes collègues et amis du Département de mathématiques et de statistique (DMS) de l'Université de Montréal. J'ai eu un véritable plaisir à vous côtoyer toutes ces années. J'espère que nous resterons en contact dans les années à venir. Un merci spécial à mon ami Alexandre Desfossés Foucault pour ses conseils, sa révision linguistique et nos discussions sur les mathématiques et la programmation. Merci également au très efficace support informatique du DMS, particulièrement à Michele Nasoni pour m'avoir dépanné plus d'une fois et Damien Rioux pour les conseils techniques. Je remercie le personnel administratif du département pour son efficacité, sa compréhension et sa gentillesse. Salutations à Anne-Marie Dupuis, Julie Collette, Églantine Hontanx, Émilie Langlois-Dubois et Jean-François Angers.

J'ai eu la chance de rencontrer des modèles d'enseignants qui m'ont inspiré et partagé leur passion des mathématiques. Merci à Yvan Saint-Aubin, Christiane Rousseau et Anik Soulière pour tous les conseils prodigués. J'ai pu profiter de votre expérience pour parfaire mon enseignement à vos côtés.

J'aimerais remercier la direction de l'École de technologie supérieure de m'avoir donné l'opportunité de travailler à titre de maître d'enseignement. La compréhension et les accommodements offerts à mon embauche m'ont donné le temps et la

flexibilité de terminer ma thèse. Je suis véritablement choyé d'avoir trouver un magnifique emploi dans le milieu de l'enseignement universitaire. Merci à mes collègues du Service des enseignements généraux pour leur encouragement et l'aide apportée depuis un an.

Finalement, merci à mon plus grand complice, Marc-Kevin Daoust, pour son réconfort, sa compréhension et sa patience. Merci à mes parents Luc et Lucie qui m'ont toujours encouragé et supporté dans mes projets. Merci également à toute ma famille et tous mes amis pour leur appui et leur écoute. Vos bons mots et vos encouragements ont été une grande source d'inspiration et de motivation au cours des dernières années. J'y suis enfin arrivé.

INTRODUCTION

> Il faudrait avoir complètement oublié l'histoire de la science pour ne pas se rappeler que le désir de connaître la nature a eu sur le développement des mathématiques l'influence la plus constante et la plus heureuse.
>
> Henri Poincaré

CONTEXTE ET MOTIVATION

Au printemps 2016, le Canada a connu les pires feux de forêt de son histoire. Les feux à Fort McMurray en Alberta ont forcé l'évacuation de plus de 80 000 personnes, brûlé un total de 2 400 maisons et une superficie de près de 600 000 hectares de forêt. Les autorités ont mis plusieurs semaines à contrôler ce feu. Les coûts pour les compagnies d'assurances sont estimés à 3,58 milliards de dollars, ce qui en fait le désastre naturel le plus coûteux de l'histoire canadienne [1].

Selon plusieurs prédictions [**5**, **53**], la hausse des températures à l'échelle planétaire, due aux changements climatiques, devrait augmenter la fréquence des feux de forêt et l'étendue des aires brûlées. Les états de la côte ouest nord-américaine tels que la Colombie-Britannique, l'Alberta et la Californie ont d'ailleurs connu ces dernières années d'importants feux de forêt sur leur territoire. Le nombre de feux au Canada a diminué au cours de la dernière décennie, mais la superficie brûlée par ces feux a augmenté. Ces données sont illustrées dans le graphique de la Figure 0.1.

Pour l'année 2014, le gouvernement canadien a enregistré un total de 5 126 feux de forêt. Ils ont brûlé un total de 4,6 millions d'hectares (ha). Ce nombre d'hectares représente environ le double de la moyenne de la superficie brûlée au cours de la dernière décennie. Il est intéressant de noter que seulement 3 % des feux touchent

1. Source : CBC News (7 juillet 2016) et CBC News (5 juillet 2016)

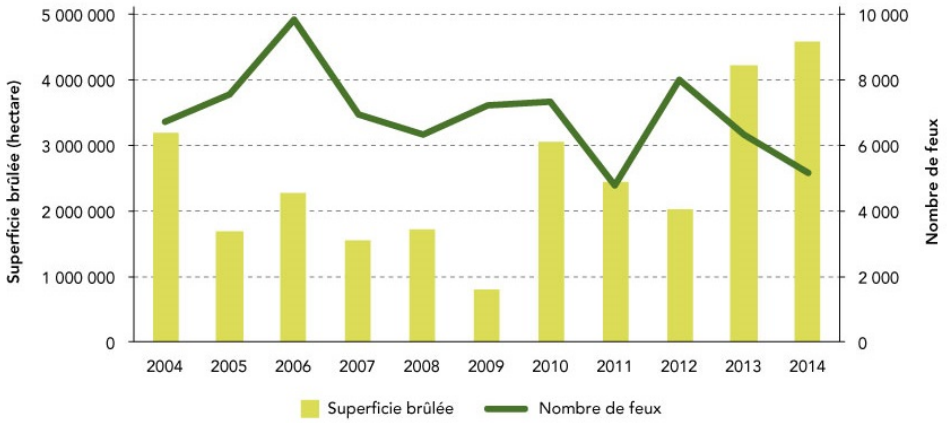

FIGURE 0.1. Superficie brûlée et nombre de feux de forêt au Canada de 2004 à 2014. Source : Ressources naturelles Canada

plus de 200 hectares et comptent pour 97 % de la superficie totale brûlée. Le gouvernement canadien estime que le coût à la lutte contre les feux de forêt se situe entre 500 millions et un milliard de dollars chaque année.

Bien que les feux permettent de préserver la santé et la diversité des écosystèmes des forêts canadiennes, ils peuvent avoir de graves conséquences sur la sécurité et la santé publique, sans oublier les pertes économiques. Afin d'élaborer des stratégies efficaces pour combattre les feux, l'utilisation de modèles mathématiques pour en faire la prédiction est maintenant courante. Des prédictions fiables et rapides permettent de prendre des décisions éclairées sur les mesures à mettre en place pour garantir la sécurité des localités.

Il s'avère que les feux de forêt constituent un phénomène environnemental très difficile à modéliser. Cette complexité découle de deux phénomènes multi-échelles qui lui sont liés, soit la dynamique de l'atmosphère et la combustion. L'élaboration de modèles de simulation pour la prédiction de la propagation des feux de forêt nécessite de résoudre des équations qui régissent l'écoulement atmosphérique et la combustion. Le développement d'un modèle pour simuler de manière précise et rapide la propagation du feu repose sur le choix approprié des variables, des équations et leurs approximations ainsi que des méthodes numériques pour les résoudre.

Les modèles mathématiques utilisés pour simuler la propagation des feux de forêt ont recours aux équations de la mécanique des fluides. La plupart des modèles représentent le feu comme une interface, une courbe, qui délimite les zones brûlées sur la topographie. Une telle simplification est pertinente pour des feux de grande superficie tels qu'illustrés à la Figure 0.2. La vitesse de déplacement du front est calculée en fonction du vent, de la topographie et du type de combustible. À ces modèles de propagation, le choix du vent aux échelles appropriées peut différer de

FIGURE 0.2. Superficie brûlée délimitée par le front d'un feu. Source : U.S. Geological Survey

manière importante. Les modèles les plus élémentaires vont considérer un champ de vitesse pour le vent horizontal et uniforme à la grandeur du domaine. D'autres vont générer un écoulement atmosphérique à l'aide d'un modèle méso-échelle basé sur les équations primitives des sciences de l'atmosphère.

La complexité du modèle utilisé va forcément influencer les résultats et le temps de calcul des simulations. Dans un contexte où le modèle doit être opérationnel et utilisable sur le terrain, il est primordial de déterminer quels paramètres et caractéristiques du modèle ont le plus d'effet sur la propagation des feux. Au cours des dernières années, plusieurs groupes de recherche ont entrepris l'étude de l'effet du feu sur l'écoulement atmosphérique. Dans les modèles opérationnels actuels tels que Prometheus [**10**] et Farsite [**44**], la contribution du feu comme source de chaleur n'est pas prise en compte. Pourtant, le feu réchauffe l'air ambiant par convection et radiation thermale et perturbe l'écoulement atmosphérique à des échelles locales près du front. Une approche couplée qui rend les modèles pour le feu et l'atmosphère interdépendants peut pallier ce problème. Plusieurs questions demeurent ouvertes sur le couplage. Comment prendre en compte les effets de la chaleur dégagée par le feu dans le calcul du vent qui contribue en retour à la vitesse de propagation du feu ? Est-ce que les effets du couplage sont plus importants que l'utilisation d'un modèle atmosphérique complet ?

OBJECTIFS

L'objectif principal de ce projet est d'élaborer un nouveau modèle couplé feu-atmosphère afin d'étudier les effets du couplage sur la propagation des feux de forêt. Ce modèle fera appel à un modèle atmosphérique plus simple que les modèles

méso-échelles utilisés actuellement. L'écoulement atmosphérique sera gouverné uniquement par une équation de divergence correspondant à une contrainte d'incompressibilité. Le temps de calcul du modèle en sera largement réduit puisque les équations primitives dont celle pour la conservation de la quantité de mouvement, ne seront pas utilisées. L'équation de divergence sera pourvue d'un terme source qui prendra en compte les effets de la chaleur dégagée par le feu. À l'aide d'une méthode numérique basée sur les volumes finis, l'effet de la géométrie du terrain sur le vent sera considéré dans la résolution du modèle atmosphérique.

La représentation du déplacement de la frontière du feu, qui délimite les zones brûlées, fera appel à la méthode numérique «level set» [**75**, **90**]. Dans le cas tridimensionnel, le terrain correspondra à une surface décrite par une fonction à deux variables. La propagation du feu sous l'action du vent sera représentée par une courbe se déplaçant à même cette surface. Puisque l'interface du feu est infiniment mince, la perturbation sur l'écoulement sera prise en compte dans l'équation de divergence pour le calcul du vent par l'introduction d'une paire source-puits représentée par des fonctions delta de Dirac. L'ajout de ces fonctions delta forcera le développement de nouvelles méthodes numériques afin de pallier les problèmes engendrés par ces singularités.

Finalement, l'expérimentation numérique jumelée à l'analyse adimensionnelle permettra de déterminer les différents régimes où cette nouvelle approche couplée pourra remplacer les modèles actuels qui sont limités par le temps de calcul pour faire la prédiction des feux de forêt. Ces régimes seront caractérisés par l'amplitude du vent initial, l'intensité du feu et la géométrie du terrain. Cette étude permettra enfin de déterminer si le vent induit par le feu permet de reproduire des caractéristiques dans la propagation du feu similaires à celles produites par des modèles plus complexes.

APERÇU DE LA THÈSE

Plusieurs approches ont déjà été envisagées pour des modèles de feux de forêt. Le chapitre 1 de cette thèse fait état des travaux effectués par le passé. Ils y sont synthétisés dans une revue de littérature de six modèles couplés pour simuler la propagation de feux de forêt. Ces modèles se regroupent en deux catégories. La première est constituée de modèles de simulation couplés qui utilisent une méthode numérique pour représenter le front et un modèle atmosphérique méso-échelle pour simuler le vent. La deuxième regroupe les modèles physiques où les équations décrivant les phénomènes de combustion et du mouvement des masses d'air sont complètement résolues. Une description de ces modèles sera donnée afin d'en connaître leurs principales caractéristiques.

Le développement de nouvelles méthodes numériques a été nécessaire afin de tirer avantage des caractéristiques particulières du modèle couplé et ainsi représenter adéquatement un terme source de chaleur défini par une singularité à l'interface. Le chapitre 2 présente une méthode de régularisation d'une fonction delta centrée sur cette interface, une variété de codimension 2. Un algorithme de rééchelonnage permet de garantir la satisfaction de la première condition de moment. L'expérimentation numérique permet de confirmer la suffisance de cette condition pour obtenir la convergence des solutions numériques à un problème elliptique.

La dérivation du modèle couplé est détaillée dans le chapitre 3. Une description du modèle atmosphérique basé sur une approximation de faible nombre de Mach est présentée. En découle une contrainte de divergence avec un terme source qui caractérise les effets de la chaleur dégagée par le feu sur l'écoulement atmosphérique. Une analyse dimensionnelle permet de caractériser, à l'aide d'un nouveau nombre sans dimension, l'intensité du couplage entre le modèle pour le feu et le nouveau modèle atmosphérique. Les régimes de propagations sont étudiés pour le modèle couplé bidimensionnel.

Le chapitre 4 présente les résultats numériques obtenus avec le modèle couplé tridimensionnel. L'implémentation des méthodes numériques est d'abord détaillée avec l'algorithme qui explique le fonctionnement du modèle. L'analyse adimensionnelle permet une classification des différents régimes selon la magnitude du vent, l'intensité du feu et l'angle de la pente du terrain. L'expérimentation numérique avec des topographies idéalisées permet de compléter l'étude qualitative des régimes de propagation des feux. Le modèle est finalement calibré afin de comparer les résultats des simulations avec le modèle Firetec. L'objectif est de déterminer quels phénomènes de propagation du feu peuvent être reproduits par le couplage sous la forme d'une paire source-puits dans l'équation de divergence pour le vent.

Chapitre 1

REVUE DES MODÈLES COUPLÉS POUR LA PROPAGATION DES FEUX DE FORÊT

De nombreux modèles pour la propagation des feux de forêt ont été élaborés au cours des 20 dernières années. Sullivan présente ces modèles dans sa revue de littérature qui détaille en trois parties les modèles conçus entre 1990 et 2008. La première partie est consacrée aux modèles physiques et quasi physiques [**96**]. Ces types de modèles tentent de représenter les phénomènes physiques lors de la combustion et de la propagation d'un feu tels que les transferts de chaleur, la turbulence et la convection. Les modèles physiques essaient également de prendre en compte les processus chimiques engendrés par le feu, comme la formation de produits ou les changements de phase de certaines substances. Deux de ces modèles, FIRETEC et WFDS sont présentés dans cette revue.

Dans la deuxième partie de la revue de Sullivan [**97**], les modèles empiriques et quasi empiriques sont présentés. Les modèles empiriques, tels que celui de McArthur [**68**], sont des modèles basés sur l'observation et l'expérimentation et non sur la théorie. Ceux-ci n'ont généralement recours à aucune théorie physique. Les modèles quasi empiriques, comme celui de Rothermel [**88**], utilisent un certain cadre physique sur lequel est construit le modèle. Dans les deux cas, ces modèles sont basés sur des données recueillies sur le terrain ou en laboratoire pour lequel un traitement statistique permet de déterminer les caractéristiques principales de certains types de feu. Il s'agit de la vitesse de propagation du front de flammes dans la direction du vent, la hauteur, l'angle et la largeur des flammes. Les variables recueillies sur le terrain sont le type de combustible, les caractéristiques du terrain, la vitesse du vent et la température. Ces variables sont ensuite traitées afin de déterminer des corrélations entre ces quantités et le comportement du feu.

Les modèles de simulation et les analogues mathématiques sont détaillés dans le troisième article de Sullivan [**98**]. Les modèles de simulation implémentent différents aspects des types de modèles précédents dans un contexte de simulation

plutôt que de modélisation. Le but ultime du développement de ces modèles est d'aboutir à un outil efficace, rapide et facile d'implémentation permettant de simuler la propagation du feu dans un contexte réel.

Papadopoulos et Pavlidou [76] font également une revue des modèles consacrés à la simulation. Ils y présentent plusieurs modèles dont le modèle canadien Prometheus, mais se concentrent davantage sur FARSITE, considéré comme le modèle le plus précis par plusieurs chercheurs à travers le monde. Les analogues mathématiques réfèrent à des modèles qui utilisent des outils mathématiques plutôt que des principes physiques pour modéliser la propagation du feu de forêt. Les modèles de percolation et les automates cellulaires en sont des exemples.

Pour le projet de recherche envisagé, une attention particulière est davantage portée à six modèles faisant le couplage du feu avec l'atmosphère. L'objectif est de déterminer les approches numériques, les équations utilisées ainsi que les échelles de simulation visées par les différents modèles.

1.1. MODÈLES DE SIMULATION

Quatre modèles de simulation sont présentés dans cette section. Chaque modèle correspond à un modèle atmosphérique couplé avec un modèle développé pour simuler la propagation du feu. Une description de la méthode numérique pour représenter le front, les approximations physiques pour modéliser l'atmosphère et les détails du couplage du feu avec l'atmosphère sont donnés pour chaque modèle.

1.1.1. CAWFE

Le modèle CAWFE (*Coupled Atmosphere-Wildland Fire-Environment*) [17, 21, 22, 23, 25, 26] a été développé par Clark, Coen et leur équipe du National Center for Atmospheric Research (NCAR). Clark *et al.* ont entrepris l'élaboration d'un modèle couplé après avoir expliqué dans deux articles parus en 1996 [19, 20] l'importance du couplage entre le feu et l'atmosphère. Le modèle atmosphérique utilisé est basé sur le modèle méso-échelle non-hydrostatique de Clark-Hall [18], tandis que les algorithmes de BEHAVE [6] sont utilisés pour estimer la vitesse de propagation du feu. Le calcul du taux de perte de masse du combustible est quant à lui fait à partir du modèle BURNUP [2].

La modélisation de la propagation du feu est faite à l'aide d'une approche inspirée de la méthode des marqueurs. Cela résulte par des coûts de calcul plus importants que la méthode des marqueurs traditionnelle, mais toutefois inférieurs à ceux nécessaires pour les approches en mécanique des fluides numérique.

Le modèle atmosphérique est une extension du modèle de la dynamique de l'atmosphère développé par Clark et Hall [18]. Le modèle résout les équations pronostiques pour la quantité de mouvement, l'énergie thermodynamique, la vapeur d'eau et les variables nécessaires à la modélisation des nuages et des précipitations. Ces variables sont mises à jour à chaque pas de temps aux points du maillage pour des domaines emboîtés.

Les équations de Navier-Stokes pour le modèle atmosphérique sont approximées par l'équation de la quantité de mouvement :

$$\bar{\rho}\frac{d\mathbf{V}}{dt} + 2\boldsymbol{\Omega}\times\mathbf{V} = -\nabla p' + g\bar{\rho}\mathbf{B} + \frac{\partial \tau_{ij}}{\partial x_j} \tag{1.1.1}$$

et par la conservation de la masse sous forme de contrainte anélastique avec laquelle les ondes du son sont filtrées :

$$\nabla\cdot\bar{\rho}\mathbf{V} = 0 \tag{1.1.2}$$

où $\mathbf{V}$ est la vitesse de l'air, $\bar{\rho} = \rho(z)$ la densité de l'air (pour un état de base) qui varie selon l'altitude z, $\boldsymbol{\Omega}$ le vecteur de rotation de la Terre, g l'accélération de la pesanteur, p' la perturbation de la pression, $\mathbf{B}$ la flottabilité (*buoyancy*) et τ_{ij} le tenseur des contraintes.

Une procédure habituelle pour traiter les variables thermodynamiques dans le contexte anélastique est de faire une expansion de la variable à partir d'un environnement de référence :

$$\phi(\mathbf{x}, t) = \bar{\phi}(z) + \phi'(\mathbf{x}, t) \tag{1.1.3}$$

où $\mathbf{x}$ correspond aux coordonnées spatiales (x, y, z) et où ϕ représente soit la densité ρ, la température potentielle θ, la température absolue T, la pression p ou la proportion de mélange de vapeur d'eau q_v. La barre signifie un état moyen ou de base et le prime dénote la déviation locale par rapport à l'état de base. Les variables telles que la proportion de mélange de nuages condensés q_c et la proportion de mélange d'eau de pluie q_r et toutes autres espèces d'eau ou de concentration de particules ne sont pas traitées de cette manière. Les variables de l'état de référence sont en balance hydrostatique où

$$\frac{\partial \bar{p}}{\partial z} = -g\bar{\rho} \tag{1.1.4}$$

et ils obéissent à la loi des gaz parfaits :

$$p = \rho R_d T \tag{1.1.5}$$

où R_d correspond à la constante des gaz pour l'air sec.

La flottabilité est approximée par

$$B = \left[\frac{\theta'}{\bar{\theta}}(1 + \epsilon q_v) + \epsilon q_v - q_c - q_r \right] \tag{1.1.6}$$

avec $\epsilon = R_v / R_d - 1$ où R_v est la constante des gaz pour la vapeur d'eau.

Le couplage entre le feu et l'atmosphère se fait à l'aide de l'équation de conservation de la variable thermodynamique ψ :

$$\frac{\partial}{\partial t}\bar{\rho}\psi + \nabla \cdot (\bar{\rho}\mathbf{V}\psi) = S_\psi + \frac{\partial}{\partial x_i} H_i^\psi \tag{1.1.7}$$

où ψ est soit θ, q_v, q_c ou q_r et où S_ψ est l'échelle locale de la grille et où H_i^ψ est le flux de sous-grille de ψ dans la direction x_i. Les flux de chaleur latente et sensible [1] associés avec le feu sont introduits dans le modèle atmosphérique en modifiant les flux verticaux H_3^θ et $H_3^{q_v}$:

$$H_3^\theta = \bar{\rho} K_H \frac{\partial \theta}{\partial z} + F_s(\mathbf{x}, t) \tag{1.1.8}$$

$$H_3^{q_v} = \bar{\rho} K_H \frac{\partial q_v}{\partial z} + F_l(\mathbf{x}, t) \tag{1.1.9}$$

où K_H est le coefficient de diffusion thermique turbulente (*eddy*). Les flux de chaleurs qui se dégagent de la zone brûlée sont absorbés par l'air en utilisant une profondeur d'extinction α tel que

$$F_s(\mathbf{x}, t) = F_s(x, y, h, t) \exp\left(-\frac{z-h}{\alpha}\right) \tag{1.1.10}$$

$$F_l(\mathbf{x}, t) = F_l(x, y, h, t) \exp\left(-\frac{z-h}{\alpha}\right) \tag{1.1.11}$$

où F_s et F_l correspondent respectivement à la chaleur sensible et latente produite par la combustion et où $h = h(x, y)$ est la hauteur de la topographie. Le terme α varie généralement entre 50 et 100 m. Un article précédent [**20**] a démontré que le modèle n'est pas très sensible à ce paramètre et les observations par imagerie infrarouge [**21**] ont permis de conclure que la hauteur est d'environ 50 m, valeur choisie pour les simulations.

Le modèle a recours à plusieurs domaines emboîtés les uns dans les autres. Ces domaines peuvent être raffinés dans les directions verticale et horizontale. Les domaines extérieurs résolvent les événements atmosphériques tels que des fronts et les systèmes convectifs méso-échelles tandis que les domaines internes résolvent les équations sur une échelle plus fine, ce qui permet de bien simuler les nuages convectifs et les vortex qui se forment à quelques mètres du feu.

1. Ces termes sont définis dans le glossaire à l'annexe B.

Le domaine le plus à l'intérieur a la résolution la mieux adaptée pour l'échelle du feu. Le modèle est couplé de sorte que l'information calculée par le modèle atmosphérique est utilisée pour propager le front du feu alors que la chaleur et l'humidité dégagées par le feu sont transférées à l'atmosphère, ce qui influence les écoulements atmosphériques. Pour chaque pas de temps dans le domaine intérieur, les vitesses du vent au plus bas niveau de la grille verticale du modèle sont transmises au modèle pour la propagation du feu. Pendant ce pas de temps, du combustible est brûlé sur le front ainsi que derrière celui-ci. La chaleur et l'humidité du combustible sont intégrées au modèle atmosphérique comme des flux près de la surface.

Après que le front ait été mis à jour, l'aire de la région brûlée pendant le pas de temps est calculée afin de déterminer la fraction de combustible brûlé. Cette procédure utilise des éléments de l'algorithme de BURNUP. En utilisant le coefficient de combustion, le combustible brûlé durant le dernier pas de temps est converti en flux de chaleur latente et sensible. Il est à noter que CAWFE a d'abord utilisé la relation empirique pour la vitesse de propagation proposée par McArthur [**68**]. Il utilise dorénavant la formule développée par Rothermel [**88**].

Clark *et al.* [**17**] font quatre simulations en utilisant trois domaines emboîtés. Le domaine total mesure $8.4 \times 8.4 \times 7.88$ km avec un maillage horizontal de 120 m. Le domaine intermédiaire mesure $3.36 \times 3.36 \times 4.08$ km avec un maillage de 40 m et le domaine intérieur est de $2.8 \times 2.8 \times 1.03$ km avec un maillage de 20 m. Les expérimentations sont faites en terrain plat et sur une colline définie par une gaussienne, et ce pour deux types de combustibles, soient le chaparral et le gazon.

Les auteurs remarquent une perte de la symétrie du front lors de la propagation du feu sur la colline. Ils attribuent ce phénomène aux erreurs de troncature et d'arrondi et peut-être aussi à des artefacts du code. Ils remarquent que la largeur de la bande du feu demeure étroite tout au long de la simulation. L'échange de chaleur net entre le feu et l'atmosphère est largement indépendant de la résolution des cellules de combustible. Finalement, les simulations montrent que la propriété d'ellipticité du feu est un résultat direct du couplage feu-atmosphère.

Coen [**21**] utilise le modèle dans un cadre plus réaliste en simulant la propagation du feu de Big Elk, survenu au Colorado en 2002. Les six domaines emboîtés sont beaucoup plus grands que dans les simulations précédentes. Le domaine total mesure 340×360 km avec un maillage de 10 km tandis que le domaine le plus petit a un maillage de 41 m. Coen arrive à des résultats convaincants et les simulations avec un maillage entre 100 et 500 m arrivent à capturer la propagation globale du feu.

1.1.2. WRF-fire

Le modèle WRF-fire [**15**, **24**, **64**, **65**, **66**, **77**, **91**, **92**] utilise le *Weather Research and Forecasting Model* et le solveur ARW (*Advanced Research WRF*) servant à faire les prévisions atmosphériques combiné à la méthode «level set» pour représenter la propagation du feu. Ce modèle a été élaboré à partir du modèle CAWFE qui utilise une méthode de marqueurs pour la propagation du feu. Bien que le code pour le calcul de la vitesse de propagation du feu et des flux de chaleur soit le même que celui de CAWFE, WRF-fire utilise un modèle atmosphérique et un algorithme pour la propagation différents.

Le modèle physique consiste à un ensemble d'équations qui régissent la vitesse de propagation du feu et les flux de chaleur. La vitesse est calculée à partir de la méthode implémentée dans *BEHAVE*. Le modèle du feu est développé dans le plan horizontal sur lequel le terrain est projeté. Une approche semi-empirique est utilisée et la vitesse est donnée par la formule de Rothermel [**88**] modifiée

$$S = R_0(1 + \phi_W + \phi_S) \tag{1.1.12}$$

où R_0 est la vitesse en absence du vent, ϕ_W est le facteur vent et ϕ_S le facteur de la pente. Ces composantes sont calculées à partir des propriétés des combustibles, de la vitesse du vent et de la pente du terrain.

Le terrain est initialisé avec une fraction de combustible $F = 1$. Une fois que le combustible est allumé, la fraction de combustible diminue en suivant une relation exponentielle :

$$F(t) = \exp\left(-\frac{(t - t_i)}{T_f}\right) \tag{1.1.13}$$

où t est le temps, t_i le temps à l'allumage et T_f le temps pour le brûlage du combustible. La fraction de combustible est approximée sur chaque cellule C du maillage pour la région du feu par

$$F(t) = 1 - \frac{1}{\text{Area}(C)} \iint_{\substack{x \in C \\ \psi(x,t) \leq 0}} 1 - \exp\left(-\frac{(t - t_i(x))}{T_f(x)}\right) dx. \tag{1.1.14}$$

Les densités de flux de chaleur moyen, sensible et latente, sont ensuite calculées à partir de la fraction de combustible avec les relations suivantes :

$$\phi_h = \frac{F(t) - F(t + \Delta t)}{\Delta t} \frac{1}{1 + M_f} w_l h \tag{1.1.15}$$

$$\phi_q = \frac{F(t) - F(t + \Delta t)}{\Delta t} \frac{M_f + 0.56}{1 + M_f} L w_l \tag{1.1.16}$$

où 0.56 est la proportion de masse d'eau émise de la combustion du combustible sec, M_f la quantité d'humidité dans la particule de combustible, w_l la quantité (masse) de combustible par aire et h la quantité de chaleur du combustible sec.

L'atmosphère est modélisée à l'aide de WRF [**93**] qui permet de faire des interpolations verticales du vent selon un profil logarithmique et d'insérer des cartes de combustibles et des topographies de haute résolution. WRF utilise des coordonnées verticales qui suivent la topographie (*hydrostatic pressure vertical coordinate*). Le modèle résout un système d'équations différentielles pour plusieurs variables telles que l'humidité de l'air, la température potentielle, la balance hydrostatique, la température thermodynamique et la pression hydrostatique. Le temps est discrétisé avec la méthode de Runge-Kutta explicite d'ordre 3. Les variables scalaires sont localisées au centre des cellules tandis que les composantes du vent sont placées au centre des faces de chaque cellule sur une grille décalée (*staggered grid*).

Le couplage du modèle pour la propagation du feu et du WRF se fait en plusieurs étapes. À chaque pas de temps, le module pour la simulation du feu est appelé. Les composantes horizontales du vent sont interpolées verticalement selon un profil logarithmique. Ces composantes sont ensuite interpolées au centre des cellules de la grille pour le feu par une interpolation bilinéaire. L'algorithme pour le feu fait alors un pas de temps. Le schéma numérique de la méthode «level set» permet d'avancer l'interface du feu au prochain pas de temps. La fraction de combustible est mise à jour et les densités de flux de chaleur sont calculées pour chaque cellule de la grille du feu. Les densités de flux sont alors moyennées sur les cellules du feu qui composent la première couche de cellule du modèle atmosphérique.

Les flux de chaleur sont insérés dans le modèle atmosphérique comme étant des termes de force dans les équations différentielles pour la couche près de la surface seulement. Une décroissance exponentielle avec l'altitude est supposée. Un tel schéma est nécessaire puisque le WRF ne supporte pas les conditions aux bords pour le flux. Le flux de chaleur sensible ϕ_h est ajouté comme un terme source dans l'équation de la température potentielle θ, égale à la divergence verticale du flux de chaleur :

$$\frac{d(\mu\theta)}{dt}(x,y,z) = R_\Theta(\Phi) + \frac{\mu(x,y)\phi_h(x,y)}{\sigma\rho(x,y,z)}\frac{\partial}{\partial z}\exp\left(-\frac{z}{z_{ext}}\right) \tag{1.1.17}$$

tandis que le flux de chaleur latente ϕ_q est inséré à l'équation de la tendance de concentration de vapeur q_m :

$$\frac{d(\mu q_m)}{dt}(x,y,z) = R_{Q_m}(\Phi) + \frac{\mu(x,y)\phi_q(x,y)}{L\rho(x,y,z)}\frac{\partial}{\partial z}\exp\left(-\frac{z}{z_{ext}}\right) \tag{1.1.18}$$

où μ est la composante hydrostatique de la pression différentielle de l'air entre la surface et le haut du domaine, $Q_m = \mu q_m$ la quantité d'humidité de l'air, σ la chaleur massique de l'air, ρ la densité de l'air, z_{ext} la hauteur d'extinction de la chaleur et L la chaleur latente massique de l'air.

Les auteurs font quelques remarques concernant la modélisation de l'atmosphère. Dans un modèle couplé, il a été remarqué que la composante horizontale du vent directement au-dessus de la ligne de front peut être nulle. Il a donc été proposé de prendre le vent à une certaine distance derrière le front pour le calcul de la vitesse de propagation du feu. De forts flux de chaleur peuvent également modifier le profil logarithmique du vent. La vitesse de propagation comme une fonction du vent à une altitude donnée peut ne pas être une bonne approximation. La propagation du feu peut ainsi dépendre plus fortement du profil complet du vent. Il est également suggéré d'utiliser une grille pour le feu dix fois plus fine que celle utilisée pour l'atmosphère afin de permettre une émission graduelle de la chaleur dans l'atmosphère. La taille du maillage de l'atmosphère ne devrait pas dépasser 60 m puisqu'un maillage trop grand entraîne des taux de propagation et une dynamique atmosphérique incorrects. Les auteurs mentionnent que le mode LES devrait être activé dès que les domaines intérieurs ont un maillage inférieur à 100 m. À cette résolution, le modèle devrait être capable de résoudre la plupart des turbulences responsables du mélange dans la couche limite et donc la paramétrisation de la couche limite dans ce cas n'est pas nécessaire.

Des méthodes d'allumage et l'utilisation d'un filtre de Kalman d'ensemble pour assimiler des données [**66**] sont également implémentées dans le modèle. Beezley *et al.* [**14**] ont utilisé ce modèle pour simuler le feu de Meadow Creek. Six domaines emboîtés étaient nécessaires pour passer de l'échelle atmosphérique initiale (32 km) à l'échelle du feu (10 m). Ils ont conclu que le modèle WRF n'était pas conçu pour les simulations micro-échelles ce qui menait à des problèmes de stabilité. Imbriquer des domaines pour passer de 32 km à 100 m ne permet pas de capturer les caractéristiques atmosphériques locales. Le feu semblait se propager trop rapidement comparativement aux observations.

1.1.3. Méso-NH/ForeFire

Filippi *et al.* [**41**, **42**] suivent la démarche entreprise par Clark *et al.* [**17**] en combinant deux modèles, Méso-NH et ForeFire, afin de comprendre les effets introduits par le flux de chaleur dans l'atmosphère sur la vitesse de propagation et le comportement du feu. Méso-NH [**54**] est un modèle méso-échelle anélastique et non-hydrostatique qui peut être utilisé aussi bien pour des simulations de grandes

échelles (synoptiques) que de petites échelles (*Large Eddy Simulation*). Contrairement au modèle de Rothermel [**88**] pour lequel la pente et les effets du vent sont pris en compte comme des coefficients empiriques dépendant du combustible et ajustés à la vitesse du vent comme si le feu n'était pas là, le modèle ForeFire proposé par Balbi *et al.* [**7**] prend explicitement ces deux facteurs en considération.

Plusieurs approximations sont utilisées afin de dériver le modèle. Parmi celles-ci, la forme de la flamme est supposée triangulaire avec sa base au sol donnée par la largeur du front dans la direction normale. La vitesse de la flamme est la somme géométrique de la vitesse du vent à la position de la flamme et de la vitesse de flottabilité. La propagation se fait dans la direction normale au front. L'angle d'inclinaison de la flamme par rapport à la normale de la pente γ, telle qu'illustrée à la figure 1.1, est calculé à l'aide d'une méthode vectorielle :

$$\tan(\gamma) = \frac{u\sin(\alpha) + U}{u\cos(\alpha)} = \tan(\alpha) + \frac{U}{u_0} \tag{1.1.19}$$

où $u_0 = u\cos(\alpha)$. Le paramètre U représente la vitesse du vent normal à la propagation du front, α est l'angle d'inclinaison de la pente et u est la vitesse verticale dans la flamme sans le vent.

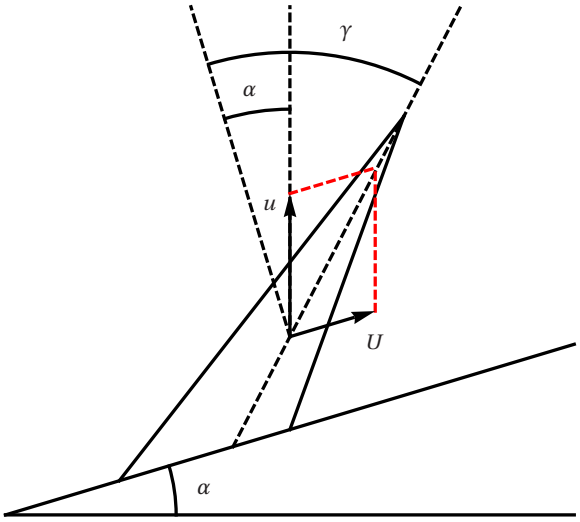

FIGURE 1.1. Schéma d'une flamme sur une pente inclinée d'un angle α.

Au final, le modèle calcule la vitesse de propagation du front à l'aide de la relation suivante :

$$R = R_0 + A\frac{R(1+\sin\gamma-\cos\gamma)}{1+\dfrac{R}{r_0}\cos\gamma} \tag{1.1.20}$$

où r_0 est le facteur de vitesse dû à la radiation, R_0 la vitesse de propagation sans le vent et la pente et A le facteur radiant (rapport de chaleur radiée par rapport à

la chaleur totale émise). Filippi *et al.* suggèrent que cette méthode pour calculer la vitesse de propagation du front serait plus appropriée pour une configuration couplée que les approches du type de Rothermel pour calculer la vitesse.

Pour représenter le front, le modèle utilise la méthode des marqueurs. Le couplage du feu avec l'atmosphère se fait à chaque pas de temps, durant lequel les matrices du vent sont mises à jour. Trois matrices de surfaces sont nécessaires pour forcer le modèle atmosphérique au niveau du sol, soient les flux de chaleur convective Q_e, le flux de vapeur d'eau $W w_e$ et la température radiative T_e. Ces matrices sont calculées à partir d'une matrice contenant le ratio de chaque cellule brûlée. La température rayonnante est calculée à l'aide de l'équation de Stefan-Boltzman :

$$T_e = \sqrt[4]{(1 - R_b) T_s^4 + R_b T_n^4} \tag{1.1.21}$$

où $R_b = S_b / S_c$ est la proportion d'aire brûlée de chaque cellule atmosphérique et où T_n est la température nominale de la flamme et T_s la température du sol. Une hypothèse importante est que le front de flamme peut être représenté comme une boîte rectangulaire émettant une radiation comme un corps noir. Ces matrices sont passées au modèle atmosphérique à chaque pas de temps, juste avant de mettre à jour la matrice du vent qui advecte le front. Le vent est interpolé par une méthode bi-cubique à l'endroit où se trouvent les marqueurs derrière le front.

Pour les trois simulations décrites dans leur premier article [**41**], le modèle couplé a été en mesure de reproduire la convection du feu et l'accélération du front due à l'accélération des vents pris par le panache de feu. L'échelle de la simulation étant un kilomètre carré pour une heure, celle-ci est encore loin de l'échelle pour des feux de forêt plus importants, soit des centaines de kilomètres carrés pour environ une journée.

Dans l'article paru en 2011 [**42**], le modèle Meso-NH/Forefire est comparé au modèle HIGRAD/FIRETEC en utilisant les mêmes cas idéalisés utilisés par Linn [**61**]. Comparé aux simulations menées par Linn, Meso-NH/Forefire sous-estime la vitesse de propagation du feu dans tous les cas. Toutefois, l'approche couplée offre une meilleure estimation de cette vitesse que l'approche non couplée. En prenant en compte les effets du feu sur l'atmosphère, le couplage permet toujours d'avoir des résultats similaires à HIGRAD/FIRETEC en ce qui est de la distance de propagation du feu. Le modèle couplé s'avère également d'une grande importance dans le cas test du canyon, où la vitesse du vent de surface au fond du canyon est fortement diminuée par les effets topographiques et où l'influence des vents induits par le feu est importante lors du calcul de la vitesse de propagation du feu. De manière générale, le comportement du feu dans la direction du vent est similaire à celui observé par Linn *et al.*

1.1.4. UU-LES

Sun *et al.* [100] présente dans leur article des simulations numériques menées à l'aide du modèle *University of Utah Large Eddy Simulation* (UU-LES) couplé à un modèle de propagation de feu de forêt basé sur CAWFE. Les modèles empiriques ne permettent pas de prédire le comportement transitoire du feu dû aux changements dans l'écoulement local. L'écoulement dans la couche limite atmosphérique est turbulent de nature, mais aucune étude n'avait pris en compte ces effets sur la vitesse de propagation et sur la taille des feux de forêt. L'objectif de l'article de Sun *et al.* était de simuler la propagation de lignes de feux sur des plaines afin d'examiner les effets de deux types de couche limite atmosphérique sur la propagation de la ligne, l'interaction du feu avec ces deux sortes d'écoulement et l'importance du couplage feu-atmosphère comparativement à l'impact de la turbulence des deux types de couches. Les simulations ont montré qu'il est plus important de bien capter l'influence du feu sur l'écoulement qui propage le feu à son tour plutôt que de s'attarder aux effets de la turbulence de la couche limite. Ceci est montré à l'aide de deux types de couche limite, une dominée par les effets convectifs où les structures principales de l'écoulement sont déterminées par quelques puissants courants ascendants et l'autre par des mouvements de rouleaux horizontaux.

UU-LES a été conçu pour examiner les écoulements atmosphériques de petites échelles tels que la convection de cumulus et la turbulence. Le modèle utilise les équations primitives non-hydrostatiques en trois dimensions. L'approximation quasi-compressible, par laquelle la vitesse du son est artificiellement réduite, permet au code d'être hautement flexible tout en restant économique en temps de calcul. La fermeture d'énergie cinétique turbulente à l'échelle sous-grille (SGS TKE) est appliquée. Les flux de quantité de mouvement et les quantités scalaires sont calculés à l'aide des viscosités turbulentes dérivées du SGS TKE. Un schéma Runge-Kutta d'ordre 2 de type *time-split* est utilisé. Le maillage est donné par une grille étirée verticalement. La théorie de similarité de Monin-Obukhov permet de donner une condition limite pour la quantité de mouvement. Une couche éponge est aussi spécifiée près du haut du domaine pour réduire la réflexion des ondes de gravité.

Les vents générés par UU-LES près de la surface sont passés au modèle opérationnel empirique développé par Hirsh [50] pour générer la vitesse de propagation. Le feu est tracé en utilisant une forme de la méthode des marqueurs de Clark *et al.* [17]. Le modèle couplé simule les feux sur des échelles où le maillage de la grille conventionnelle d'une dizaine de mètres est trop grossier pour résoudre les processus physiques dans la zone de combustion. La dégradation thermique du combustible solide n'est pas modélisée directement et la combustion est paramétrée. Tel

que décrit par Sun *et al.* [99], l'énergie de la combustion est distribuée dans les niveaux les plus bas en utilisant une profondeur d'extinction exponentielle constante.

Dans la plupart des simulations, huit feux sont allumés simultanément excepté pour une simulation où deux feux sont allumés. Un vent de base constant à 5.5 ms^{-1} a été spécifié pour chaque simulation et le vent à 5 m au-dessus du sol a été choisi pour le calcul de la vitesse de propagation du feu. Les feux sont allumés sur des surfaces planes et le combustible est réparti de manière uniforme sur le terrain. Les simulations dans la couche limite convective montrent que les feux brûlent de plus petites surfaces lorsqu'il n'y a pas de couplage. C'est le vent induit par le feu qui propage principalement le feu dans la direction du vent. La superposition de vingt-quatre feux simulés à partir d'une même ligne d'allumage suggère que la propagation du feu n'est pas déterministe dans la couche limite convective même lorsque le vent induit par le feu n'est pas considéré. Une prédiction probabiliste de la propagation du feu permettrait de prendre en compte le caractère non déterministe ou la nature aléatoire du vent qui alimente le feu. Cela aiderait à rendre la formule utilisée dans le calcul de la vitesse de propagation plus utile.

Les auteurs ont également considéré les effets de la longueur de la ligne d'allumage sur la propagation du feu. Les simulations montrent que les lignes plus longues se propagent plus rapidement que les lignes plus courtes. Un mécanisme important de l'augmentation de l'écoulement induit par le feu est la présence de forts courants descendants derrière le front du feu. Le rôle de ce courant est d'apporter de l'air du haut vers la surface où le feu se propage. Son développement est le résultat de l'interaction entre la circulation induite par le feu et la forte circulation turbulente dans la couche limite atmosphérique. Le type de couche limite affecte directement la variabilité de l'aire brûlée, la vitesse de propagation, la forme du feu et la force de la convection induite par le feu. Les lignes de feu dans la couche limite convective avaient tendance à se propager 25% plus rapidement et à brûler de plus grandes surfaces. Les types de turbulence qui dominaient la couche limite atmosphérique dans l'étude menée par Sun *et al.* étaient prescrits par l'échelle de vitesse convective w^*. Il serait intéressant d'utiliser ce paramètre pour modéliser les effets de la turbulence de la couche limite atmosphérique sur la propagation du feu.

1.2. MODÈLES PHYSIQUES

Deux modèles physiques sont présentés dans cette section, soient FIRETEC et WFDS. Ces modèles sont développés dans le but ultime de servir à la gestion des feux malgré que les échelles utilisées soient trop petites et que le temps de calcul soit trop élevé pour être considéré comme des modèles de prédiction valables. Il est

également très difficile de mesurer les paramètres et les variables au degré de précision requis par ces modèles. Les conditions aux bords sont rarement connues. Ces modèles font appel à la chimie de la combustion. Ils déterminent l'énergie relâchée par le combustible et la quantité d'énergie transmise au combustible environnant non brûlé et à l'atmosphère à partir d'un modèle de combustion.

1.2.1. HIGRAD/FIRETEC

FIRETEC [16, 29, 39, 58, 59, 60, 61, 62, 63, 64, 69, 79, 80] est un modèle basé sur une approche de transport multi-phase et utilise les équations de la conservation de la masse, de la quantité de mouvement, de l'énergie et des espèces chimiques. Développé par Linn et son équipe à Los Alamos National Laboratory, ce modèle est combiné à un modèle hydrodynamique appelé HIGRAD [86] utilisé pour résoudre des équations d'un écoulement soumis à de forts gradients (*HIgh GRADient flow*). Il utilise une formulation de transport des gaz complètement compressibles pour représenter les interactions couplées de la combustion, les transferts de chaleur convective et rayonnante et la traînée aérodynamique, ce qui permet d'incorporer les détails microscopiques du feu à une résolution macroscopique. Ce modèle atmosphère-feu tridimensionnel est complètement autodéterminé et est résolu à l'aide de la méthode des volumes finis.

Une description détaillée du modèle est disponible dans la thèse de doctorat de Linn [58]. L'ensemble des équations décrivant les réactions chimiques lors de la combustion a été simplifié qu'à une seule expression [60] décrivant la réaction solide-gaz :

$$N_{bois} + N_{O_2} \rightarrow \text{produits} + \text{chaleur} \tag{1.2.1}$$

où N_{bois} et N_{O_2} sont les coefficients stoechiométriques qui décrivent la quantité nette de bois et d'oxygène consumé lors de la pyrolyse et toutes les réactions intermédiaires lorsque qu'une unité de masse de produits est formée.

L'évolution de la température potentielle moyenne θ des gaz combinés est donnée par

$$\begin{aligned}\frac{\partial \rho_{gaz}\theta}{\partial t} + \frac{\partial \theta u_j \rho_{gaz}}{\partial x_j} &= \frac{\partial}{\partial x_j}\left(\sigma \frac{\partial \theta}{\partial x_j}\right) \\ &\quad + \frac{\theta}{c_p}\left[\frac{h a_v (T_s - T_{gaz}) + Q_{rad,gaz} + F_{bois}(1-\Theta) H_{bois}}{T_{gaz}}\right]\end{aligned} \tag{1.2.2}$$

où ρ_{gaz} est la densité des gaz combinés, u_j leur vitesse moyenne dans la direction j, σ le coefficient de diffusion turbulente, c_p la chaleur massique des gaz, h le coefficient d'échange de chaleur convective, a_v l'aire de contact par unité de volume entre le gaz et le combustible solide, T_s et T_{gaz} les températures du combustible

solide et du gaz respectivement, $Q_{rad,gaz}$ le gain net en énergie par le gaz de la radiation thermique, F_{bois} le taux de changement du bois dans un volume donné, Θ la fraction de chaleur émise du gaz en combustion qui est redéposé directement au solide et H_{bois} l'énergie de la chaleur dans le bois par unité de masse associé à un flux. Le terme source entre crochets représente l'échange de chaleur convective, de chaleur rayonnante et une source d'énergie due aux réactions chimiques.

Linn *et al.* ont produit plusieurs articles portant sur différentes simulations réalisées pour des situations idéalisées dans le but de déterminer l'effet de certains facteurs sur l'évolution de la propagation du feu. Dans un premier article [**59**], FIRETEC est utilisé afin de déterminer l'effet du vent sur la propagation du feu. Les auteurs remarquent que la vitesse de propagation dépend significativement de la longueur initiale du front et que pour une vitesse de vent donnée, la vitesse de propagation est plus rapide pour les longs fronts que les courts. De plus, non seulement la vitesse de propagation dépend du vent ambiant, mais aussi de la forme et de la taille du feu.

L'effet de la topographie sur la propagation [**61**] est également étudié à l'aide de cinq terrains idéalisés (plat, colline, canyon, entonnoir et crête) pour deux vitesses du vent ambiant (6 ms^{-1} et 12 ms^{-1}). L'objectif de ces dix simulations est de déterminer s'il y a des situations où le feu n'a pas besoin d'être couplé au champ de vitesse du vent ou encore des cas où le couplage s'avère critique. Dans certains cas, les processus dominants dans la propagation du feu peuvent être en mesure de capter les effets locaux dus à la topographie. Le couplage semble plus important lorsque les vents influencés par la topographie ne sont pas directement complémentaires aux effets de la pente sur le feu, comme l'influence du canyon sur la propagation latérale et frontale du feu. Il demeure impossible de généraliser les impacts de terrains inhomogènes sur la vitesse de propagation à partir des dix simulations.

Cunningham et Linn étudient en détail le comportement du feu dans le cas des prairies [**29**]. Dans leur plus récent article, Linn et al. [**62**] s'intéressent aux effets de la pente et de la composition du combustible (sa quantité, sa structure, son hétérogénéité et son humidité) dans la propagation du feu. Les combustibles choisis sont le chaparral, l'herbe et le pin ponderosa dans les cas d'un terrain plat et d'une colline.

1.2.2. WFDS

Le modèle WFDS [**69**, **70**, **71**, **73**, **74**] est une version du modèle FDS (Fire Dynamics Simulator) combiné à l'extension WUI (*Wildland-Urban Interface*) permettant de calculer la propagation du feu sur des combustibles végétaux. FDS a été développé au *Building and Fire Research Laboratory* au *National Institute of Standards*

and Technology (NIST) au cours des trente dernières années. La moitié des applications de ce modèle à ce jour ont été de concevoir des systèmes pour contrôler la fumée et de mener des études sur la détection du feu et l'efficacité des extincteurs automatiques à eau.

WFDS utilise des flux de chaleur transitoires plutôt qu'un flux constant. Ce flux de chaleur résulte de l'interaction entre le feu et l'atmosphère déterminé par la solution numérique des équations de conservation pour la quantité de mouvement, la masse totale, l'énergie et la quantité d'espèces. La combustion est modélisée avec une approche basée sur la fraction de mélange. WFDS peut simuler les feux en trois dimensions et en mode DNS ou LES. La végétation est vue comme une source de résistance de quantité de mouvement (*momentum drag*), de flux de chaleur et de flux de masse sur le bord inférieur du domaine pour la phase gazeuse.

Les équations pour modéliser les écoulements sont données par l'approximation à faible nombre de Mach. L'algorithme de Runge-Kutta de deuxième ordre pour la discrétisation temporelle et les différences finies de deuxième ordre sur une grille rectangulaire pour la discrétisation spatiale sont utilisés. L'équation de conservation de la masse est donnée par :

$$\frac{\partial \rho}{\partial t} + \nabla \cdot \rho \mathbf{u} = 0, \tag{1.2.3}$$

l'équation de conservation de la quantité de mouvement par :

$$\frac{\partial \rho \mathbf{u}}{\partial t} + \nabla \cdot \rho \mathbf{u}\mathbf{u} + \nabla p = \rho \mathbf{f} + \nabla \cdot \boldsymbol{\tau}_{ij} \tag{1.2.4}$$

et la conservation de l'énergie par

$$\frac{\partial \rho h}{\partial t} + \nabla \cdot \rho h \mathbf{u} = \frac{Dp}{Dt} + \dot{q}''' - \nabla \cdot \mathbf{q} + \boldsymbol{\Phi} \tag{1.2.5}$$

où $\mathbf{f}$ est un terme de force qui consiste à la gravité et d'autres types de forces, $\boldsymbol{\tau}_{ij}$ le tenseur des contraintes, h l'enthalpie sensible comme fonction de la température $h = \int_{T_0}^{T} c_p(T')dT'$, c_p la chaleur spécifique à pression constante, $\dot{q}'''$ le taux de chaleur émise de la réaction chimique par unité de volume, $\nabla \cdot \mathbf{q}$ les flux de chaleur conductive et rayonnante et $\boldsymbol{\Phi}$ une fonction de dissipation, soit le taux auquel l'énergie cinétique est transférée à l'énergie thermique due à la viscosité du fluide.

1.3. Comparaisons des modèles

Les six modèles précédents possèdent des caractéristiques différentes et peuvent être utilisés pour simuler les feux de forêt à des échelles bien précises. Cette section présente un résumé comparatif des caractéristiques et des échelles de chaque modèle.

1.3.1. Échelles de simulation

Chaque modèle utilise une taille de domaine, un maillage pour le modèle atmosphérique et du feu et un pas de temps différents. Dans le tableau 1.I, les échelles utilisées lors des simulations par chaque modèle sont données ainsi que la taille du domaine total.

Modèles	atmosphère [m]	feu [m]	domaine [km]	Δt [s]
CAWFE [**17**]	20	20	$8.4 \times 8.4 \times 7.88$	–
WRF-fire [**14, 65**]	100	10	$10 \times 12 \times 1$	0.082
Méso-NH/Forefire [**41**]	30	30	$1.2 \times 1.2 \times 1.2$	0.5
UU-LES [**100**]	10	10	$3.2 \times 3.2 \times 2$	–
HIGRAD/FIRETEC [**29**]	2	2	$0.32 \times 0.32 \times 0.615$	–
WFDS [**70**]	1.6	1.6	$1.5 \times 1.5 \times 0.2$	–

TABLE 1.I. Échelles utilisées pour les simulations des différents modèles

Il est à noter que pour les modèles de simulation, la taille du domaine total ne dépasse jamais 10 km de côté, malgré que ces modèles ont recours à des modèles atmosphériques méso-échelles valides que pour des domaines beaucoup plus grands. On peut ainsi supposer que pour les besoins de simulation, les modèles sont initialisés sur un domaine beaucoup plus grand, mais que le domaine considéré pour la propagation du feu est celui donné dans le tableau. Les échelles des modèles physiques sont beaucoup plus petites et le maillage plus fin que pour les modèles de simulations. Une telle résolution est nécessaire afin de bien prendre en compte les variables impliquées dans les réactions chimiques de la combustion.

1.3.2. Caractéristiques des modèles

Chaque modèle propose des approximations, utilise des méthodes numériques et présente des caractéristiques qui les différencient les uns des autres. Le tableau 1.II synthétise les caractéristiques de chaque modèle.

Les modèles de simulation ont tous recours à un modèle atmosphérique méso-échelle tandis que les modèles physiques résolvent les équations de Navier-Stokes sans approximations. Tous les modèles atmosphériques utilisent une grille verticale étirée, soit un maillage plus fin près de la surface du terrain et plus espacé lorsque la coordonnée verticale augmente. Les équations modélisant les phénomènes atmosphériques sont toutes basées sur les équations primitives sous forme non-hydrostatique.

Certains modèles font appel à un modèle de turbulence tel que le *Large Eddy Simulation*. La formule semi-empirique pour le calcul de la vitesse de propagation

Modèles	*«level set»*	Marqueurs	LES	DNS	Approximation
CAWFE		✓			anélastique
WRF-fire	✓		✓		compressible
Méso-NH/Forefire		✓			anélastique
UU-LES		✓	✓		quasi-incompressible
HIGRAD/FIRETEC					compressible
WFDS			✓	✓	faible Mach

TABLE 1.II. Caractéristiques des modèles

du feu change d'un modèle à l'autre. Elles découlent généralement de la formule donnée par Rothermel [**88**]. La méthode des marqueurs est différente pour chacun des trois modèles qui l'utilisent. Tous les modèles sont tridimensionnels.

Les détails du couplage entre le modèle atmosphérique et le modèle de propagation du feu varient pour chaque modèle bien que l'idée générale soit relativement la même. La première étape consiste à calculer la quantité de combustible brûlé entre deux pas de temps. Ensuite, les flux de chaleur et de vapeur, l'énergie ou toute autre quantité qui sera injectée dans le modèle atmosphérique sont calculés. Ceux-ci sont intégrés au modèle atmosphérique, soit dans l'équation de conservation de quantité de mouvement ou une équation de type conservation d'énergie. Le modèle atmosphérique fait ensuite un pas de temps, ce qui met à jour le champ vectoriel du vent. Le vent près du feu permet finalement de calculer la vitesse de propagation du feu. Le modèle du feu fait un pas de plus et la boucle recommence.

1.4. POSITIONNEMENT DU MODÈLE COUPLÉ DANS LA RECHERCHE

Le modèle couplé proposé dans cette thèse fait appel une nouvelle approche pour le couplage et un type de modèle atmosphérique différent des modèles méso-échelles utilisés actuellement. Comme pour le modèle WFDS, le modèle atmosphérique découle de l'approximation à faible nombre de Mach, mais est constitué d'une unique équation de divergence avec un terme source. Cette équation est une combinaison des équations de la conservation de la masse et de l'énergie ainsi que de l'équation d'état. La conservation de la quantité de mouvement n'est pas prise en compte directement dans le modèle. Cette contrainte sur la divergence du vent est satisfaite en résolvant un système elliptique où la topographie est intégrée explicitement comme frontière du domaine. Aucun modèle de turbulence n'est utilisé. Le modèle atmosphérique se trouve ainsi dans une classe à part, située entre les modèles «complets» qui ont recours aux équations primitives (voir l'annexe A) tels que

les modèles ci-dessus et les modèles qui ne satisfont que la conservation de la masse [47, 72, 81].

Comme dans les modèles de simulation qui ont recours au couplage, le feu est représenté par une interface infiniment mince qui délimite les zones brûlées. Contrairement à la majorité des modèles, notre modèle pour le feu utilise la méthode «level set» plutôt que la méthode des marqueurs afin de suivre la propagation du feu sur la topographie. Cette méthode a été adaptée afin d'y intégrer le modèle de l'ellipse de Richards [87] pour la propagation du feu. Tout en prenant en compte la géométrie de la topographie sur la vitesse de propagation, la méthode est restreinte à la projection de l'interface dans le plan xy plutôt que sur la topographie. Cela permet de limiter le temps de résolution numérique. Ces caractéristiques du modèle pour le feu sont présentées en détail dans la thèse de doctorat d'Alexandre Desfossés Foucault [31].

Plutôt que d'injecter des quantités ou des flux dans le modèle atmosphérique, le couplage du feu vers l'atmosphère se fait à l'aide du terme source de l'équation de divergence. Cette perturbation du feu sur l'écoulement atmosphérique est donnée par une paire source-puits définie à l'aide d'une fonction delta centrée sur l'interface. Le recours à la fonction delta est cohérent avec le modèle de propagation puisque le feu y est représenté par une interface infiniment mince. La perturbation est ainsi concentrée le long de l'interface.

L'utilisation du doublet source-puits permet de capturer les effets de la force de flottaison et de la vorticité qui seraient autrement perdues en l'absence de l'équation de la quantité de mouvement. L'écoulement généré par la perturbation locale due à la chaleur dégagée par le feu capture l'effet d'entraînement et le mouvement de recirculation caractéristiques des plumes. Finalement, l'amplitude de la perturbation est calculée à partir de la formule de l'intensité de Byram [3, 4].

Chapitre 2

RÉGULARISATION D'UNE SOURCE SINGULIÈRE SUR UNE VARIÉTÉ DE CODIMENSION 2 POUR UN MODÈLE COUPLÉ FEU-ATMOSPHÈRE.

Ce chapitre est constitué de l'article *Regularization of a Singular Source on a Codimension-2 Manifold for a Coupled Fire-Atmosphere Model*. L'objectif principal de l'article est d'adapter des méthodes de régularisation d'un delta de Dirac pour le cas particulier où le support est une variété de codimension 2 disposée au bord d'un domaine irrégulier. Dans le modèle couplé feu-atmosphère, la fonction delta représente un terme source dans le membre de droite d'une équation de divergence. Cette source est liée à la chaleur dégagée par le feu. Les contributions principales de l'article sont :

(1) la régularisation d'une fonction delta sur une variété de codimension 2 ;

(2) un algorithme de rééchelonnage pour satisfaire la condition de moment ;

(3) une étude de la convergence des solutions numériques d'un problème elliptique.

RÉSUMÉ

Cet article présente une nouvelle méthode de régularisation pour une source singulière définie par une fonction delta dont le support est une variété de codimension 2. Cette méthode a été développée pour le cas d'un problème elliptique résolu avec une approche cartésienne où la fonction delta est régularisée sur le bord inférieur d'un domaine irrégulier. Les conditions de moment établies précédemment pour les variétés de codimension 1 sont généralisées pour la codimension 2. La régularisation combinée avec un processus de rééchelonnage assure que l'approximation de la fonction delta remplit la condition de premier moment et pallie

les problèmes de convergence dus à l'irrégularité de la grille. Des expériences numériques en 2D et 3D montrent que cette condition est suffisante pour obtenir la convergence des solutions lorsque le taille de la maille tend vers zéro.

REGULARIZATION OF A SINGULAR SOURCE ON A CODIMENSION-2 MANIFOLD FOR A COUPLED FIRE-ATMOSPHERE MODEL

Louis-Xavier Proulx

ABSTRACT. This paper presents a new regularization method for a singular source given by a delta function supported on a codimension-2 manifold. This method was developed for the case of an elliptic problem to be solved with a Cartesian grid method where the delta function is regularized at the bottom boundary of an irregular domain. The moment conditions previously established for codimension-1 manifolds are generalized for the codimension-2 case. The regularization combined with a rescaling process guarantees the delta function approximation fulfills the first moment condition, needed to recover convergence on such an irregular grid. Numerical experiments in 2D and 3D indicate that this condition is sufficient for the convergence of the solutions as the mesh size goes to zero.

2.1. INTRODUCTION

In this article, we introduce a new regularization technique for a singular source. This technique has been designed to take into consideration the particular features of a novel coupled fire-atmosphere model for forecasting the spread of wildfire. In this forecast model, the fireline is represented as an infinitely thin interface moving on topography with a rate of spread that changes in time as a function of the local wind, slope and fuel bed. This fireline is referred as the manifold Γ, being either a point in 2D or a curve in 3D, as shown in Figure 2.1. Even if the dimension of the manifold changes with the dimension of the problem, its codimension is always equal to 2. This model takes on a totally novel approach for taking into account the

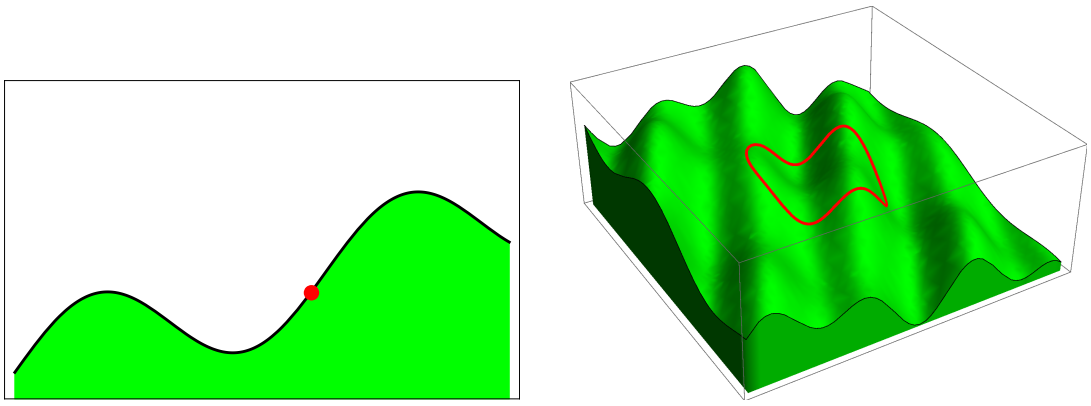

FIGURE 2.1. Fireline interface (red point/curve) lying on the topography (green surface) at the bottom boundary of the irregular computational domain in 2D (**left**) and 3D (**right**).

effect of the fire on the local wind velocity field. Rather than using a mesoscale atmospheric model, the wind model consists of a single divergence equation for the wind velocity field **u**:

$$\nabla \cdot \mathbf{u} = S. \tag{2.1.1}$$

The source term S represents the amount of heat released by the fireline which perturbs the local wind flow in return. Since the fireline is an infinitely thin manifold Γ on which the heat release is concentrated, the source S is represented as a delta function $\delta(\Gamma)$ supported on the codimension-2 manifold. A projection method is used to compute the wind velocity field **u**. It assumes that the wind velocity field can be decomposed into two parts:

$$\mathbf{u} = \mathbf{v}_d + \nabla \Phi. \tag{2.1.2}$$

where $\mathbf{v}_d$ is a divergence-free part ($\nabla \cdot \mathbf{v}_d = 0$) and Φ a potential function that accounts for the fire heat source. Hence, computing **u** satisfying the divergence equation (2.1.1) requires the solution of the following elliptic problem on the irregular domain Ω:

$$\begin{aligned} \Delta \Phi &= S = \delta(\Gamma), \\ \Phi^B &= 0 \quad \text{on the open boundaries,} \\ \frac{\partial \Phi^B}{\partial n} &= 0 \quad \text{on the topography.} \end{aligned} \tag{2.1.3}$$

The Neumann condition applied Φ^B at the bottom boundary corresponds to a slip condition for the wind velocity field **u**. The homogeneous Dirichlet conditions applied at the top and the side boundaries allow the wind to flow through these boundaries. This elliptic problem is solved with a Cartesian grid embedded boundary method [**8, 52, 57, 81, 89**]. This method was shown to be efficient for solving partial differential equations on domains with irregular boundaries. Their representation is given by the intersection (embedding) of the domain with Cartesian cells, which leads to irregular control volumes. These cut cells are the result of the intersection of the bottom boundary, the topography, and the rectangular cells of the Cartesian grid, as illustrated in Figure 2.2. A convenient discretization of the divergence operator can be performed with a finite volume approach. Special care is taken in the computation of the fluxes in the irregular cells. A marker-and-cell (MAC) grid is used: the fluxes and vector field are centered on the cell faces and the scalar quantities, such as the potential Φ and the regularized delta source, at the cell centers. The height of the topography $h(x, y)$ is assumed to be known. This allows the definition a level set function of the form $\psi(x, y, z) = h(x, y) - z$, for which the zero level curve corresponds to the terrain surface. This function is already used by the embedded

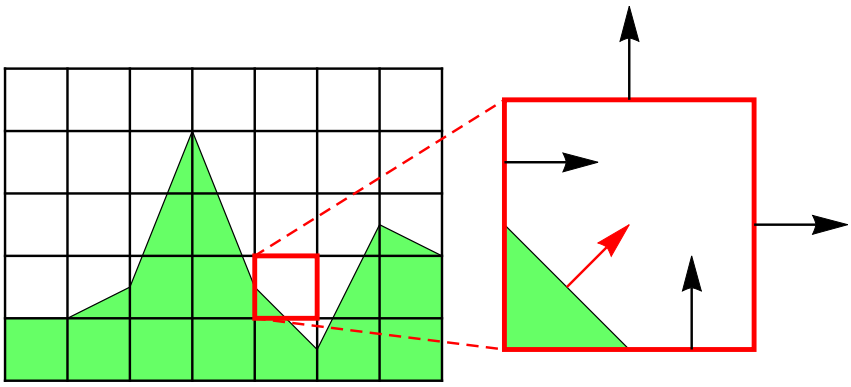

FIGURE 2.2. Embedded boundary on a Cartesian grid with fluxes at the face centroids of a given cut cell (irregular control volume).

boundary method for the mesh generation [57]. The model also uses a level set method for tracking the evolution of the fireline Γ on the topography. The manifold can therefore be represented as the intersection of the zero level set of the topography level function with the zero level set of the fireline level function. The regularization technique for the delta function takes advantage of this representation of the codimension-2 manifold with two level set functions. This paper presents a generalization of some existing regularization techniques adapted to the specific context of the coupled model for wildfire spread described above. Particular features and challenges of the regularization problem are considered here: the fireline being a codimension-2 manifold on which the delta is regularized, the singular source support lies at the bottom boundary of a complex domain and the computational domain has irregular control volumes (cut cells). After a short review of regularization techniques, a new regularization involving a rescaling process is presented. This approach palliates the numerical difficulties coming from the irregularity of the cells when smoothing the delta function. The rescaling is also a sufficient condition to ensure the convergence of the numerical solutions of the elliptic problem (2.1.3). Numerical experiments corroborate this claim.

2.2. REGULARIZATION FOR CODIMENSION-1 MANIFOLDS

Singular source terms come up in many differential equations, in particular in interface problems solved with the level set method [75, 90, 101]. In a series of papers, Tornberg *et al.* [40, 102, 103, 104, 115] have studied different regularization approaches and delta function approximations for codimension-1 manifolds. Towers [105, 106] has also worked on the regularization of delta functions supported

on manifolds of different codimensions. Smereka [**94**] derived a delta function approximation obtained as the truncation error in solving the Laplacian of the Green's function. Recently, Hosseini *et al.* [**51**] studied the convergence of a sequence of distributions to a singular term. They were able to construct regularizations of the delta distribution which generalize the methods developed in previous work. There are different approaches for regularizing a delta function supported on a codimension-1 manifold. The general idea is to replace the singular delta function by a regular function δ_ε. In one dimension, the delta function can be approximated by a continuous function $\varphi(\xi)$ of the form:

$$\delta_\varepsilon(x) = \frac{1}{\varepsilon}\varphi\left(\frac{x}{\varepsilon}\right) \tag{2.2.1}$$

where ε is half the size of the compact support. This scaling is quite natural since $\delta_\varepsilon \to \delta$ as $\varepsilon \to 0$. Classical choices for the delta function regularizations are the piecewise linear hat function:

$$\varphi^L(\xi) = \begin{cases} (1-|\xi|) & \text{if } |\xi| \le 1 \\ 0 & \text{if } |\xi| > 1 \end{cases} \tag{2.2.2}$$

and the cosine approximation:

$$\varphi^C(\xi) = \begin{cases} \frac{1}{2}(1+\cos(\pi\xi)) & \text{if } |\xi| \le 1 \\ 0 & \text{if } |\xi| > 1 \end{cases} \tag{2.2.3}$$

as illustrated in Figure 2.3. Tornberg and Engquist [**104**] discuss the link between the

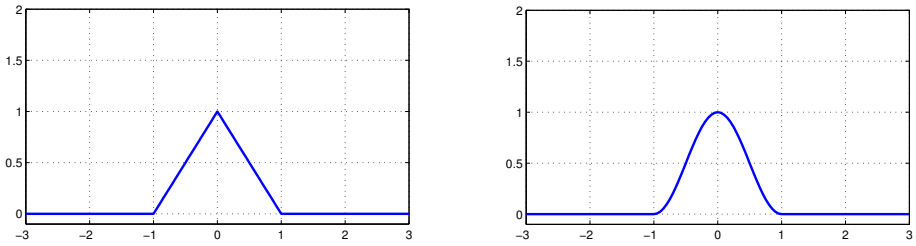

FIGURE 2.3. Hat $\varphi^L(\xi)$ (**left**) and cosine $\varphi^C(\xi)$ (**right**) approximation functions for the delta function.

discretization error and the discretized moment condition. The moment condition plays an important role in the regularization of the delta function.

2.2.1. Moment condition for a codimension-1 manifold

The moment conditions for the one-dimensional delta function are defined in the following way:

Definition 2.2.1. [104] *A function δ_ε satisfies q discrete moment conditions if for all $x^* \in \mathbb{R}$,*

$$M_r(\delta_\varepsilon, x^*, h) = h\sum_{i\in\mathbb{Z}} \delta_\varepsilon(x_i - x^*)(x_i - x^*)^r = \begin{cases} 1, \ \text{if } r = 0 \\ 0, \ \text{if } 1 \le r < q \end{cases} \tag{2.2.4}$$

where $x_i = ih$, $h > 0$, $i \in \mathbb{Z}$.

If the function δ_ε satisfies q moment conditions, then we say that it has a moment order q. The first moment condition ensures that the mass of the delta function δ_ε is one, independent of shifts in the grid. The higher moment conditions are important when the delta approximation is multiplied by a non-constant function. The hat (2.2.2) and cosine (2.2.3) approximations above fulfill the first moment condition and they are of order 1 and 2 respectively. It is possible to construct one-dimensional delta functions with any number of correct moments depending on the size of the support. In one dimension, the numerical accuracy of a regularized delta function is determined by the number of satisfied discrete moment conditions as stated by the following proposition.

Proposition 2.2.1. [104] *Assume δ_ε satisfies q discrete moment conditions and has compact support in $[-Mh, Mh]$. Assume also that $f(x) \in C^q(\mathbb{R})$ and that all derivatives of f are bounded, then*

$$E = \left| h\sum_{i\in\mathbb{Z}} \delta_\varepsilon(x_i - x^*) f(x_i) - f(x^*) \right| \le Ch^q \tag{2.2.5}$$

and $E = 0$ if f is constant.

The proof is provided by Tornberg and Engquist in [104] and uses Taylor expansion. These authors had shown in [103] that for $\varepsilon = ph$, the common approximation of the delta function by the hat function will satisfy the mass condition if p is an integer while the cosine function satisfies the mass condition when $2p$ is an integer. If this is not the case, then there is an $O(1)$ error in the approximation. The one-dimensional delta function approximations δ_ε above can be generalized to the multivariable $\delta-$function, in higher dimensions as the product of one-dimensional $\delta-$functions for each variable:

$$\delta_\varepsilon(x, y, z) = \frac{1}{\varepsilon^3}\varphi\left(\frac{x}{\varepsilon}\right)\varphi\left(\frac{y}{\varepsilon}\right)\varphi\left(\frac{z}{\varepsilon}\right). \tag{2.2.6}$$

It was shown by Tornberg and Engquist [104] that this extension technique is consistent and that the result given by the proposition above can be extended to the multidimensional case. This technique is, however, only applicable when an explicit representation of the curve or the surface which supports the delta function is available.

Tornberg *et al.* [**40, 104, 115**] also worked on a delta approximation on codimension-1 manifolds defined by a level set function. Define $\delta(\Gamma, g, \mathbf{x})$ as a delta function of variable strength supported on $\Gamma \subset \mathbb{R}^n$ a $(n-1)-$dimensional closed, continuous, and bounded surface such that:

$$\int_{\mathbb{R}^d} \delta(\Gamma, g, \mathbf{x}) f(\mathbf{x}) d\mathbf{x} = \int_{\Gamma} g(s) f(\mathbf{X}(s)) ds \tag{2.2.7}$$

where the variable s is a parameterization of Γ, $\mathbf{x} = (x^{(1)}, \ldots, x^{(d)})$ and $\mathbf{X}(s) = (X^{(1)}(s), \ldots, X^{(d)}(s)) \in \Gamma$. Then, one possibility for the regularization of the delta is the product formula which yields

$$\delta_{\boldsymbol{\varepsilon}}(\Gamma, g, \mathbf{x}) = \int_{\Gamma} \prod_{k=1}^{d} \delta_{\varepsilon_k}(x^{(k)} - X^{(k)}(s)) g(s) ds \tag{2.2.8}$$

where δ_{ε_k} is a one-dimensional regularized delta function. In level set methods, a curve is represented implicitly as being a level curve of a higher dimensional function. A major drawback of the product definition is that it requires the explicit parameterization of the interface. Tornberg and Engquist [**104**] also pointed out that the most common technique for regularization of Dirac delta functions in level set simulations, which is to extend a regularized one-dimensional delta function to higher dimensions using a distance function, is not consistent. They give analytical and numerical examples which result in $O(1)$ errors.

To overcome the lack of consistency that became apparent with the work presented in [**104**], Engquist *et al.* [**40**] have developed two new techniques: an approximate product formula and a variable regularization parameter. With these new regularization methods, the delta function approximations are consistent with level set methods. The first technique is an approximation of the product rule using the distance function and its gradient. The second one is based on the linear hat function but uses a variable regularization parameter ε along the zero level set. Consistent approximations, for which the level set function and its gradient are needed, have also been introduced by Towers [**105**]. The advantage of these methods is that the supports of the delta function approximations are very small.

Zahedi and Tornberg [**115**] have shown that a one-dimensional delta function approximation can be extended to higher dimensions by a distance function and be made accurate with a different class of one-dimensional delta function approximations. This is possible if we can allow a wider support of the delta function approximations. It is possible to construct delta function approximations that obey the mass condition for a wide range of dilations if they have compact support in

Fourier space. One of these function is the Gaussian function:

$$\varphi^G(\xi) = \sqrt{\frac{\pi}{9}} e^{-\pi^2 \xi^2 / 9} \tag{2.2.9}$$

also illustrated in Figure 2.4.

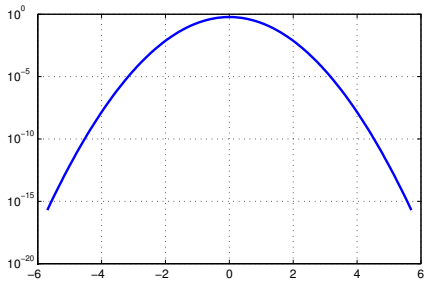

FIGURE 2.4. Gaussian $\varphi^G(\xi)$ approximation function for the delta function in log scale.

2.2.2. Moment condition for a codimension-2 manifold

The literature on regularizing delta function on a codimension-2 manifold is scarce. Zhang and Zheng [**116**] have worked on the representation of a line delta function along a space curve. An interesting study for different codimension values of the manifold has also been made in an article by Towers [**106**] which is an extension of his work [**105**] on codimension-1 manifold. He studied the regularization of delta functions supported on a manifold of codimension higher than one. Towers was particularly interested in approximating the integral:

$$I = \int_{\mathbb{R}^n} f(\mathbf{x}) \prod_{i=1}^{m} \delta(u^i(\mathbf{x})) \| \wedge_m \nabla \mathbf{u}(\mathbf{x}) \| d\mathbf{x} \tag{2.2.10}$$

with the wedge product $\wedge_m \nabla \mathbf{u}(\mathbf{x}) := \nabla u^1(\mathbf{x}) \wedge \nabla u^2(\mathbf{x}) \wedge \cdots \wedge \nabla u^m(\mathbf{x})$. This integral is an equivalent representation of the integral:

$$\int_\Gamma f(\mathbf{x}) dV^r \tag{2.2.11}$$

where $\mathbf{x} = (x^1, \ldots, x^n) \in \mathbb{R}^n$, $f : \mathbb{R}^n \mapsto \mathbb{R}$ and Γ is a manifold of dimension $r = n - m$ defined by the intersection of the zero level sets of m smooth functions $u^i : \mathbb{R}^n \mapsto \mathbb{R}$, $i = 1, \ldots, m$ with $1 \leq m \leq n$. The differential dV^r denotes a $r-$dimensional volume. The codimension is simply $n - r$. The integral I in equation (2.2.10) can be written in the context of codimension-1 manifolds, i.e. $m = 1$ and $n \leq 3$:

$$\int_{\mathbb{R}^n} f(\mathbf{x}) \delta(u(\mathbf{x})) \| \mathbf{u}(\mathbf{x}) \| d\mathbf{x}. \tag{2.2.12}$$

where $u(\mathbf{x}) = u^1(\mathbf{x})$. This integral corresponds to the integral of the left-hand side of equation (2.2.7). For the case of codimension-2 manifolds, the integral becomes

$$\int_{\mathbb{R}^2} f(\mathbf{x})\delta(u^1(\mathbf{x}))\delta(u^2(\mathbf{x}))|\det \nabla \mathbf{u}(\mathbf{x})|d\mathbf{x}. \tag{2.2.13}$$

when the dimension is $n = 2$ and where the manifold of dimension $r = 0$ is the intersection of $m = 2$ level set functions. If both level functions are signed distance functions whose gradients are orthogonal, the matrix $\nabla \mathbf{u}$ is orthogonal and therefore $|\det \nabla \mathbf{u}| = 1$. When the space has dimension $n = 3$, there are still $m = 2$ level set functions that intersect into a manifold of dimension $r = 1$, a curve. The integral I then becomes

$$I = \int_{\mathbb{R}^3} f(\mathbf{x})\delta(u^1(\mathbf{x}))\delta(u^2(\mathbf{x}))\|\nabla u^1(\mathbf{x}) \times \nabla u^2(\mathbf{x})\|d\mathbf{x}. \tag{2.2.14}$$

If $f \equiv 1$, the integral I gives the arc length of the curve Γ. Figure 2.5 presents two examples of regularized deltas on codimension-2 manifolds in space of dimension $n = 2$ and $n = 3$. In the left picture, the manifold is a single point given as the inter-

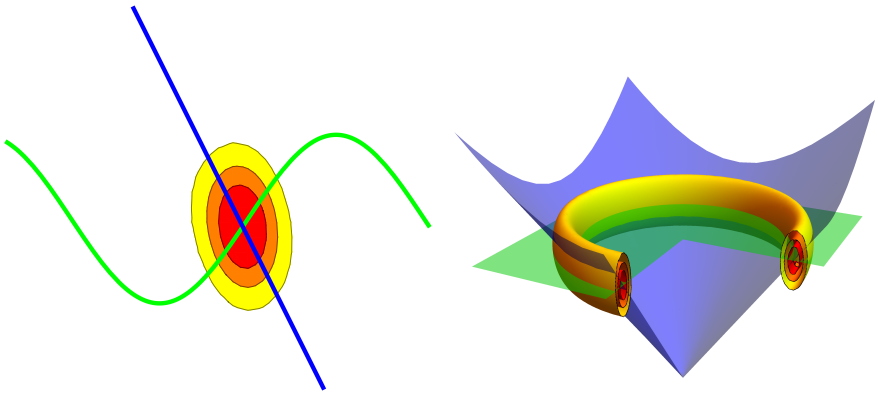

FIGURE 2.5. Examples in 2D (**left**) and 3D (**right**) of the regularized delta function with a Gaussian approximation on a codimension-2 manifold given as the intersection of the two zero level sets.

section of two zero level sets: a green sinusoidal curve and blue straight line. The red and yellow contours of the ellipse correspond to the value of the regularized delta function at this point. The contours would be circular only if the two level curves intersect with a right angle. The right picture shows a different example in 3D. The zero level sets are surfaces: the blue cone and the green horizontal plane. Their intersection is a circle on which the delta function is regularized. In this case, the value of the smoothed delta function are pictures as red and yellow concentric tubes. In one-dimensional space, the moment condition of definition 2.2.1, previously stated by Tornberg *et al.*, is a sufficient condition for consistency when the level function

$u(\mathbf{x})$ is a signed distance function. In this case, the moment condition becomes:

$$h\sum_{i\in\mathbb{Z}}\delta^h(x_i;u)=1+O(h^\mu),\qquad \mu>0. \tag{2.2.15}$$

This definition can be extended for the two-dimensional case. Assume that the delta function is supported on the intersection of $m=2$ level functions $u^1(x,y)$ and $u^2(x,y)$, its discrete approximation $\delta^h(x_i,y_j;u^1,u^2)\approx\delta(u^1(x_i,y_j))\delta(u^2(x_i,y_j))$ which is the product of delta functions $\delta(u^1)\delta(u^2)$. The moment condition is then

$$h^2\sum_{i\in\mathbb{Z}}\sum_{j\in\mathbb{Z}}\delta^h(x_i,y_j;u^1,u^2)=1+O(h^\mu),\qquad \mu>0. \tag{2.2.16}$$

Towers [**106**] explains that this last condition is *a priori* hard to satisfy. A natural approach is to consider the discrete delta approximation δ by using a product of codimension-1 approximations:

$$\delta^h(x_i,y_j;u^1,u^2)=\delta(x_i,y_j;u^1)\delta(x_i,y_j;u^2). \tag{2.2.17}$$

This approach is generally inconsistent if the level functions happened not to be aligned with the mesh. This lack of consistency due to misalignment in the codimension one case has been studied thoroughly by Tornberg *et al* [**40, 103, 104**]. Towers [**106**] overcomes this problem by considering the discretization of the wedge product formulation of the delta function. In the next section, we will show that we can enforce this moment condition and generalize it to the three-dimensional space $n=3$.

2.3. A NEW REGULARIZATION TECHNIQUE

This section presents a regularization technique combined to a rescaling process that ensures the moment condition is satisfied. It also presents an extension of the moment condition to the case where the manifold of codimension-2 is embedded in a space of dimension $n=3$. Then, these conditions are adapted to two particular characteristics of our initial elliptic problem (2.1.3): irregular mesh (cut cells) and manifold lying at the bottom boundary of the domain.

2.3.1. Generalized moment conditions

The next definition is an extension of the moment condition given in definition 2.2.1 to the space of dimension $n=2$. Its generalization is given for an explicit representation of a codimension-2 manifold in 2D space which is simply a point $\mathbf{x}^*=(x^*,y^*)$. The extension could also have been worked out from the condition given in equation (2.2.16) where the manifold is represented implicitly by the intersection of two level curves. For instance, consider the level functions u^1 and u^2 that

intersect at the single point $\mathbf{x}^* = (x^*, y^*)$. Consider also the vector $\mathbf{v} = (u^1, u^2)$ with $\mathbf{v}(x^*, y^*) = 0$ and the first terms of the Taylor series centered at (x^*, y^*):

$$\mathbf{v}(\mathbf{x}) \approx \mathbf{v}(\mathbf{x}^*) + \mathbf{D}_{\mathbf{x}}(\mathbf{v})\,|_{\mathbf{x}=\mathbf{x}^*} \cdot (\mathbf{x} - \mathbf{x}^*). \tag{2.3.1}$$

Assuming that both level functions are signed distance functions and that they are also orthogonal at their point intersection (x^*, y^*), the Jacobian matrix $\mathbf{D}_{\mathbf{x}}(\mathbf{v})\,|_{\mathbf{x}=\mathbf{x}^*}$ is then the identity matrix. The following approximation of (u^1, u^2) is then valid for $(x_i, y_j) \approx (x^*, y^*)$:

$$\mathbf{v}_{ij} = (u^1(x_i, y_j), u^2(x_i, y_j)) \approx (x_i - x^*, y_j - y^*). \tag{2.3.2}$$

Hence,

$$\delta^h(x_i, y_j; \mathbf{v}_{ij}) = \delta(u^1(x_i, y_j))\delta(u^2(x_i, y_j)) \approx \delta(x_i - x^*)\delta(y_j - y^*). \tag{2.3.3}$$

Thus a good approximation of equation (2.2.16) is

$$h^2 \sum_{i\in\mathbb{Z}} \sum_{j\in\mathbb{Z}} \delta(x_i - x^*)\delta(y_j - y^*). \tag{2.3.4}$$

Using this remark above, we can generalize the definition of the moment condition for a regularized delta supported on a point in the 2D irregular grid.

Definition 2.3.1. *A function δ_ε satisfies q discrete moment conditions if for all $\mathbf{x}^* \in \mathbb{R}^2$,*

$$M_{p,r}(\delta_{\boldsymbol{\varepsilon}}, \mathbf{x}^*; h_1, h_2) = h_1 h_2 \sum_{i\in\mathbb{Z}} \sum_{j\in\mathbb{Z}} \kappa_{ij}\delta_\varepsilon(x_i - x_1^*)\delta_\varepsilon(x_j - x_2^*)(x_i - x_1^*)^p (x_j - x_2^*)^r$$

$$= \begin{cases} 1, \ \text{if } p = r = 0 \\ 0, \ \text{if } 1 \le p, r < q \end{cases}$$

where κ_{ij} is the volume fraction of the cell (i, j), $\mathbf{x}^* = (x_1^*, x_2^*)$ is the point where the delta function is centered and $(x_i, x_j) = (ih_1, jh_2)$ with $h_1, h_2 > 0$ and $i, j \in \mathbb{Z}$.

Proposition 2.3.1 is also generalized for our given problem. The proof is based on the same idea of Taylor expansion as for the original proposition.

Proposition 2.3.1. *Assume δ_ε satisfies q discrete moment conditions and has compact support in $[-Mh_1, Mh_1] \times [-Mh_2, Mh_2]$. Assume also that $f(x) \in C^q(\mathbb{R}^2)$ and that all derivatives of f are bounded, then*

$$E = \left| h_1 h_2 \sum_{i\in\mathbb{Z}} \sum_{j\in\mathbb{Z}} \kappa_{ij}\delta_\varepsilon(x_i - x_1^*)\delta_\varepsilon(x_j - x_2^*) f(x_i, x_j) - f(x_1^*, x_2^*) \right| \le Ch^q \tag{2.3.5}$$

with $h = \max_{1\le k\le 2}(h_k)$ and $E = 0$ if f is constant.

Proof 2.3.1. *By Taylor expansion follows*

$$
\begin{aligned}
&h_1 h_2 \sum_{i\in\mathbb{Z}}\sum_{j\in\mathbb{Z}} \kappa_{ij}\delta_\varepsilon(x_i - x_1^*)\delta_\varepsilon(x_j - x_2^*) f(x_i, x_j) \\
&= h_1 h_2 \sum_{i\in\mathbb{Z}}\sum_{j\in\mathbb{Z}} \kappa_{ij}\delta_\varepsilon(x_i - x_1^*)\delta_\varepsilon(x_j - x_2^*) \times \\
&\left[\sum_{p=0}^{q-1}\sum_{r=0}^{q-1} \frac{h_1^p}{p!}(x_i - x_1^*)^p \frac{h_2^r}{r!}(x_j - x_2^*)^r D^\beta f(x_1^*, x_2^*) + O(h^q)\right] \\
&= \sum_{p=0}^{q-1}\sum_{r=0}^{q-1} \frac{h_1^p}{p!}\frac{h_2^r}{r!} D^\beta f(x_1^*, x_2^*)\left(h_1 h_2 \sum_{i\in\mathbb{Z}}\sum_{j\in\mathbb{Z}} \kappa_{ij}\delta_\varepsilon(x_i - x_1^*)\delta_\varepsilon(x_j - x_2^*)(x_i - x_1^*)^p (x_j - x_2^*)^r\right) \\
&+ O(h^q) \\
&= M_{0,0}(\delta_{\boldsymbol{\varepsilon}}, \mathbf{x}^*; h_1, h_2) f(x_1^*, x_2^*) + \sum_{p=1}^{q-1}\sum_{r=0}^{q-1} \frac{h_1^p}{p!}\frac{h_2^r}{r!} D^\beta f(x_1^*, x_2^*) M_{p,r}(\delta_{\boldsymbol{\varepsilon}}, \mathbf{x}^*; h_1, h_2) + O(h^q)
\end{aligned}
$$

where $D^\beta f = \dfrac{\partial^{p+r} f}{\partial x_1^p \partial x_2^r}$. *Since* $\delta_{\boldsymbol{\varepsilon}}$ *satisfies* q *discrete moment conditions,* $M_{0,0}(\delta_{\boldsymbol{\varepsilon}}, \mathbf{x}^*; h_1, h_2) = 1$ *and* $M_{p,r}(\delta_{\boldsymbol{\varepsilon}}, \mathbf{x}^*; h_1, h_2) = 0$ *for* $p, r = 1, \ldots, q-1$. *From this, the proposition follows.*

The last thing to do is to define the first moment condition for the case $n = 3$ and $m = 2$, which means that the delta support is a curve embedded in a space of dimension 3. The generalization follows the idea that the first moment condition corresponds to the mass of the delta function. Hence, it should be equal to the length of the curve Γ since the first moment condition is the discrete counterpart of equation (2.2.14) with $f = 1$.

Definition 2.3.2. *The first moment condition of a function* δ^h *supported on a codimension-2 manifold* Γ *in* $\mathbb{R}^3$ *is*

$$
h_1 h_2 h_3 \sum_{i\in\mathbb{Z}}\sum_{j\in\mathbb{Z}}\sum_{k\in\mathbb{Z}} \kappa_{ijk}\delta^h(x_i, y_j, z_k; u^1, u^2) = \mathit{arclength}(\Gamma) \tag{2.3.6}
$$

where κ_{ijk} *is the volume fraction of the cell* (i, j, k), Γ *is the intersection of the level functions* u^1 *and* u^2 *with* $h_1, h_2, h_3 > 0$ *and* $i, j, k \in \mathbb{Z}$.

This definition will be used in the rescaling process. Numerical experiments to be described later show that without enforcing the delta approximation to satisfy this condition the convergence of the solutions of the elliptic problem cannot be guaranteed.

2.3.2. Rescaling process

The irregularity of the computational domain leads to convergence issues when solving the elliptic problem (2.1.3) on finer meshes. This is partly caused by the embedding of a complex geometry in the Cartesian grid at the bottom boundary. The codimension-2 manifold also lies on this irregular boundary rather than on the regular cells elsewhere in the domain. A direct application of previously known delta function regularization techniques of the singular source term cannot achieve the fulfillment of the first moment condition. Using any classical approximation, the delta support will lie partially outside the computational domain as illustrated in Figure 2.6. Some cells of the uniform Cartesian grid will also be partially cut off by

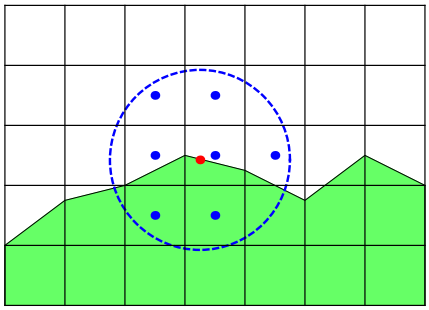

FIGURE 2.6. Delta approximation with compact support (blue dots) supported on a codimension-2 manifold (red dot) lying on the bottom boundary of a 2D irregular domain.

the embedded bottom boundary. Their volume fraction $\kappa \in [0,1]$ will play an important role in the rescaling process since the bottom topography representation changes with mesh refinement. Hence, not only part of the delta support is lost outside the computational domain, but because of its irregularity the amount of lost mass changes with the mesh refinement. This inconsistency in the delta approximation can compromise the convergence of the numerical solution of the elliptic problem. The basic idea of the rescaling process will be first introduced for the two-dimensional case. Its generalization in the 3D case will be given thereafter.

2.3.2.1. *Direct 2D rescaling*

Recall that the first moment condition in 2D is computed on a mesh with cut cells with this formula:

$$M_{0,0}(\delta_\varepsilon, \mathbf{x}^*, h) = h^2 \sum_{i\in\mathbb{Z}} \sum_{j\in\mathbb{Z}} \kappa_{ij}\, \delta_\varepsilon(x_i - x^*, y_j - y^*) = 1 \tag{2.3.7}$$

where $\mathbf{x}^* = (x^*, y^*)$ is the delta position and κ_{ij} is the volume fraction of the cell with the cell-centered value (x_i, y_j). For the elliptic problem described previously,

the regularized delta function δ_ε is located on the bottom boundary. It will not satisfy the first moment condition (2.3.7) since its support lies partially outside the domain. The mass condition $M_{0,0}(\delta_\varepsilon, \mathbf{x}^*, h)$ will not equal one, but some positive real constant $C_h < 1$. It depends on the mesh size h, since the bottom boundary representation changes with mesh refinement. The constant value also changes according to the choice of the delta function approximation. With this constant C_h, the regularized delta function is rescaled in this fashion:

$$\hat{\delta}_\varepsilon = \frac{\delta_\varepsilon}{C_h}, \tag{2.3.8}$$

so that the mass condition for the rescaled delta function $\hat{\delta}_\varepsilon$ is $M_{0,0}(\hat{\delta}_\varepsilon, \mathbf{x}^*, h) = 1$. This rescaling process ensures that the first moment condition is fulfilled and the global shape of the approximation is preserved since it is scaled by a constant only. For each mesh refinement, the value of this constant will change and the above procedure must be repeated.

2.3.2.2. *Local piecewise line segment 3D rescaling*

The 2D rescaling idea does not generalize directly in 3D, since the dimension of the manifold changes, but not its codimension. The main idea is to consider the manifold Γ on which the delta is supported as the intersection of two level functions ; one representing the bottom boundary of the domain $u^1(\mathbf{x})$ and another one $u^2(\mathbf{x})$. From the perspective of the coupled model for wildfire spread, the zero level set of $u^1(\mathbf{x})$ is simply the topography and the zero level set of $u^2(\mathbf{x})$ corresponds to the fireline. The regularization of the delta function is defined as a product of two delta functions supported on these two level functions $\delta(\Gamma, \mathbf{x}) = \delta(u^1(\mathbf{x}))\delta(u^2(\mathbf{x}))$ for which its approximation is

$$\delta^h(x_i, y_j, z_k; u^1, u^2) = \delta_{\varepsilon_1}(x_i, y_j, z_k; u^1)\delta_{\varepsilon_2}(x_i, y_j, z_k; u^2) \tag{2.3.9}$$

where δ_{ε_1} and δ_{ε_2} are the delta function approximations supported on the level set surfaces of u^1 and u^2 with half-support sizes ε_1 and ε_2 respectively. In order to achieve convergence for the numerical solutions of the elliptic problem, a piecewise line segment rescaling has been elaborated so that the delta approximation is at least moment order 1 (see definition 2.3.2). A description of the algorithm is given below. Convergence tests will be performed in the next section in order to test the rescaling technique.

Algorithm:

(1) Compute the regularized delta function $\delta^h(x_i, y_j, z_k; u^1, u^2)$ on the interface, which corresponds to the intersection of the two level-set functions u^1 and

u^2, using equation (2.3.9). This initial approximation does not satisfy the mass condition of definition 2.3.2 since the delta support partially stands outside the computational domain, below the bottom boundary. The first moment condition will not be equal to the length of the curve since a portion of the delta support occurs in zero volume cells or cut cells.

(2) Compute the "projection" of the delta approximation $\delta^h(x_i, y_j, z_k; u^1, u^2)$ in the $xy-$plane as follows:

$$\delta^h_{proj}(x_i, y_j) = h \sum_{k\in\mathbb{Z}} \kappa_{ijk} \delta^h(x_i, y_j, z_k; u^1, u^2) \tag{2.3.10}$$

where κ_{ijk} is the volume fraction of the cell (i, j, k). For one point (x_i, y_j), the value of δ^h_{proj} at this point is computed in summing the contribution of the 3D delta function in the z direction times the volume fraction of each cell. Since $\kappa_{ijk} = 0$ for cells completely below the bottom boundary, the delta contribution will not be taken into account. It is easier to rescale the delta function using the interface projection in the $xy-$plane. The projected delta function $\delta^h_{proj}(x_i, y_j)$ is computed at the blue grid points in the $xy-$plane as shown in Figure 2.7.

(3) The zero level curve of the projected level set function is represented by the union of N line segments. Using the closest line to point algorithm, described in appendix 2.B, each point of the 2D grid in the $xy-$plane is assigned to a line segment as illustrated in Figure 2.8. If for a given line segment the distance of the closest grid point to the line segment is greater than the mesh size h, then this line segment is combined with an adjacent line segment and will be considered as one line segment for the rescaling process. This case usually occurs when a line segment is very small as the green segment in the right picture of Figure 2.8.

(4) For a given line segment ℓ of the interface projection, compute the following local "mass" condition:

$$M_\ell = h^2 \sum_{i\in\mathscr{L}} \sum_{j\in\mathscr{L}} \delta^h_{proj}(x_i, y_j) \tag{2.3.11}$$

where $\mathscr{L}$ is the set of the closest grid points for a given line segment ℓ.

(5) For the same line segment, compute the length of the segment L_ℓ on the bottom boundary surface (not its projection in the $xy-$plane) using a linear approximation.

(6) Locally rescale the delta function δ^h_ℓ for this line segment ℓ:

$$\hat{\delta}^h_\ell(x_i, y_j, z_k; u^1, u^2) = \frac{L_\ell}{M_\ell} \delta^h_\ell(x_i, y_j, z_k; u^1, u^2) \tag{2.3.12}$$

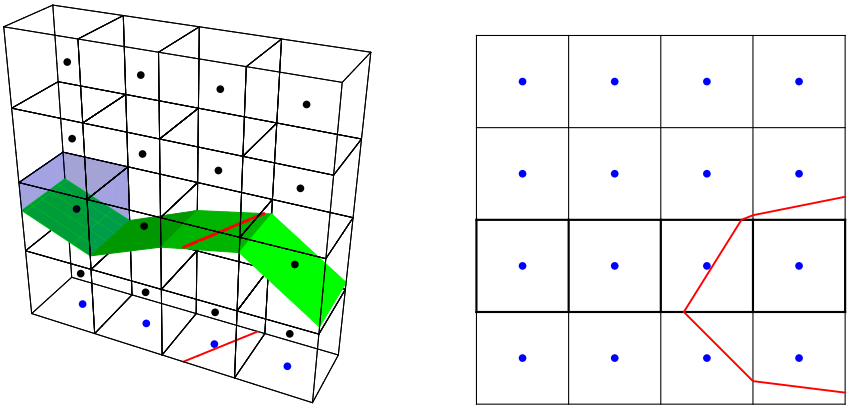

FIGURE 2.7. **Left:** 4×4 vertical grid cells of the computational domain. The bottom boundary is represented by the green polygons. The interface on which the delta is smoothed is pictured by the red line which sits on the green boundary. The red line below is its projection in the $xy-$plane. The delta function is discretized at the center of the grid cells pictured by the black dots. The projection which is computed with equation (2.3.10) will be computed at the center of grid cells in the $xy-$plane represented by the blue dots. The blue volume represents the volume fraction of a cut cell when $0 < \kappa_{ijk} < 1$. **Right:** 4×4 horizontal grid cells of the computational domain. The third row is the projection of the 3D grid cells of the left figure. The red curve is the projected interface in the $xy-$plane represented by line segments and the blue dots hold the value of the projected delta function.

where the points (x_i, y_j, z_k) correspond to all points of the 3D grid assigned to the line segment ℓ.

(7) Steps 4 to 6 of the procedure are repeated for all N line segments.

This algorithm will ultimately lead to the fulfillment of the integral property (2.3.6). Combining equations (2.3.10) and (2.3.11), one can find the local first moment condition M_ℓ for a regularized delta function:

$$M_\ell = h^2 \sum_{i\in\mathcal{L}} \sum_{j\in\mathcal{L}} \left(h \sum_{k\in\mathbb{Z}} \kappa_{ijk} \delta^h(x_i, y_j, z_k; u^1, u^2) \right) \tag{2.3.13}$$

$$= h^3 \sum_{i\in\mathcal{L}} \sum_{j\in\mathcal{L}} \sum_{k\in\mathbb{Z}} \kappa_{ijk} \delta^h(x_i, y_j, z_k; u^1, u^2). \tag{2.3.14}$$

If the local moment condition M_ℓ is computed for the local rescaled delta function $\hat{\delta}^h_\ell$, step 6 of the algorithm guarantees that $M_\ell = L_\ell$. Adding these local moment conditions for each ℓ of the N line segments:

$$\sum_{\ell\in N} M_\ell = \sum_{\ell\in N} L_\ell = \text{arclength}(\Gamma) \tag{2.3.15}$$

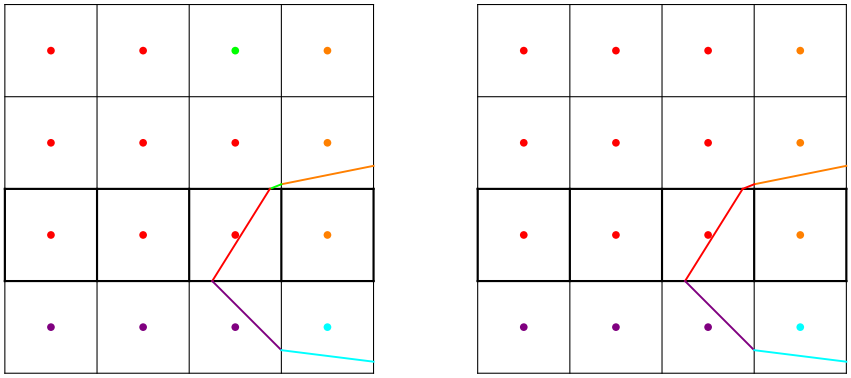

FIGURE 2.8. **Left:** The projection of the interface is represented by line segments. For each line segments, the closest grid points are assigned to it. The set of these points for a given line segment ℓ is denoted by $\mathscr{L}$. For the orange segment, $\mathscr{L}$ corresponds to the three orange grid points. Note that the number of grid points for each line segment is not the same for all. **Right:** In some cases, particularly for very short line segment as the green line segment in the left pictures, its closest assigned points are further than the mesh size. This can lead to bad behavior in convergence test. Hence, for these line segments, we merge them with their assigned points with the nearest line segment. In this case, the green line segment is merged with the red line segment.

leads to the global first moment condition (definition 2.3.2) which should be equal to the length of the curve at the bottom boundary of the domain. The merging condition for rescaling in step 3 is necessary as it ensures the delta function remains concentrated along the manifold. Figure 2.9 shows the delta regularized on a circle manifold which is the intersection of a cone level curve with the plane $z = 0$ on a grid of 34^3 cells. When the problematic segments are not merged with the neighboring segment in the rescaling process, the final regularized delta loses its regularity on the compact support. If not treated appropriately, these problematic segments can affect the convergence of the error as the mesh size goes to zero. The local rescaling algorithm in 3D is analog to the 2D rescaling technique for the particular case of the manifold being a straight horizontal line perpendicular to the mesh grid. Let's assume that the line is aligned with the $y-$axis corresponding to index j. For this particular case, each line segment ℓ matches a unique index j. The local moment condition M_ℓ used in step 6 is then computed with the delta regularized at points contained in the grid plane perpendicular to index j in the same fashion as in the direct 2D rescaling. Only, it is not exactly a plane since the grid cells have a depth h in the $y-$axis. The reason for projecting the regularized delta in the $xy-$plane is that

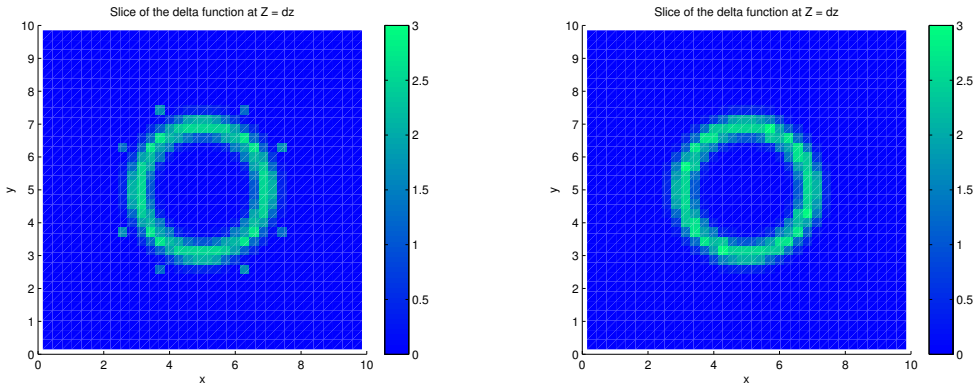

FIGURE 2.9. Regularization of the delta function on a circle manifold without (**left**) and with (**right**) treatment of the problematic segments. Plane slice at $z = h = 10/34$.

the fireline interface, the codimension-2 manifold, in the coupled fire-atmosphere model is projected by default. The level set method for spreading the manifold (interface) considers only the projection of the fire in the $xy-$plane (see Foucault's thesis [**31**]).

2.4. NUMERICAL RESULTS

Convergence tests of the numerical solution of the elliptic problem (2.1.3) are conducted to study the efficiency of the rescaling process. The tests will allow the corroboration of the claim that the use of the rescaling algorithm guarantees the convergence of the numerical solution of our particular problem. The convergence rates are studied for different geometries of the bottom boundary on which sits the delta function. It will also be tested for particular shapes of the codimension-2 manifold Γ. With the exception of the 2D rectangular domain (see appendix 2.A), it is in general not possible to find an explicit analytical solution for this problem. Hence the reference solution in all other cases will be obtained by computing a numerical solution on a very fine grid. In order to perform convergence tests, the reference solution must be averaged to the coarser grids. We used the volume-weighted average defined as

$$Av(\xi^f) = \frac{1}{V^c} \sum_{v_f \in \mathscr{F}} V^f \xi_{v_f} \tag{2.4.1}$$

where $\mathscr{F}$ is the set of cells of the fine grid v_f contained in the cell of the coarse grid v_c and where V^f and V^c are the volume of cells v_f and v_c respectively. The grids have the same number of cells N in each direction and the coarsest grids are defined with $N = 16$. The error between the numerical and reference solutions is computed

on each grid at the center of the cells. The convergence is studied in different norms. For a cell-centered variable ξ, the max norm is defined as:

$$\|\xi\|_\infty = \max_{\mathbf{i}\in\Omega} |\xi_\mathbf{i}|. \tag{2.4.2}$$

and the $p-$norm as:

$$\|\xi\|_p = \left(\sum_{\mathbf{i}\in\Omega} |\xi_\mathbf{i}|^p \kappa_\mathbf{i} h^n \right)^{1/p} \tag{2.4.3}$$

where Ω is the computational domain, $\mathbf{i}$ the index of the control cell, $\kappa_\mathbf{i}$ the volume fraction of cell $\mathbf{i}$, h the mesh size and n the space dimension. The norms of the error will be studied for $p = 1$ and $p = 2$.

2.4.1. 2D convergence analysis

Two tests are presented for the 2D convergence analysis. The first one is done on a regular domain for which the analytical solution of the elliptic problem is known. The Appendix 2.A shows how to find such a solution by considering an analog eigenvalue problem. The second test presents the results in the case of an irregular domain with a sinusoidal bottom boundary.

2.4.1.1. *Analytical solution on a rectangular domain*

The delta function is regularized with the hat function $\varphi^L(\xi)$ approximation (2.2.2) and the product rule (2.2.6) supported on a point manifold of coordinates (x^*, y^*):

$$\delta^L_\varepsilon(x - x^*, y - y^*) = \frac{1}{\varepsilon^2} \varphi^L\left(\frac{x - x^*}{\varepsilon}\right) \varphi^L\left(\frac{y - y^*}{\varepsilon}\right) \tag{2.4.4}$$

with the half-width support $\varepsilon = 2h$. It lies at the bottom boundary $y^* = 1.33$ and centered at $x^* = 5.33$. These values of the delta position make sure that the regularized delta function is not aligned with the grid at each mesh refinement. Note that the product rule (2.3.9) defined with level set functions would lead to the same results. This will be discussed later for the 3D case. The analytical and numerical solutions are computed on a 512×512 grid and are shown in Figure 2.10. The numerical solution computed with the rescaling algorithm is already in good agreement with the analytical solution. Figure 2.11 shows the error in log scale when the regularized delta function δ^L_ε is not rescaled. This error remains large at each consecutive mesh refinement and does not converge in any of the three norms. Since the delta function is not aligned with the grid and since the first moment condition is not conserved through the mesh refinement, the numerical solution does not converge to the analytical solution. Using the direct 2D rescaling, the delta approximation satisfies the first moment condition. The convergence of the numerical solution converges

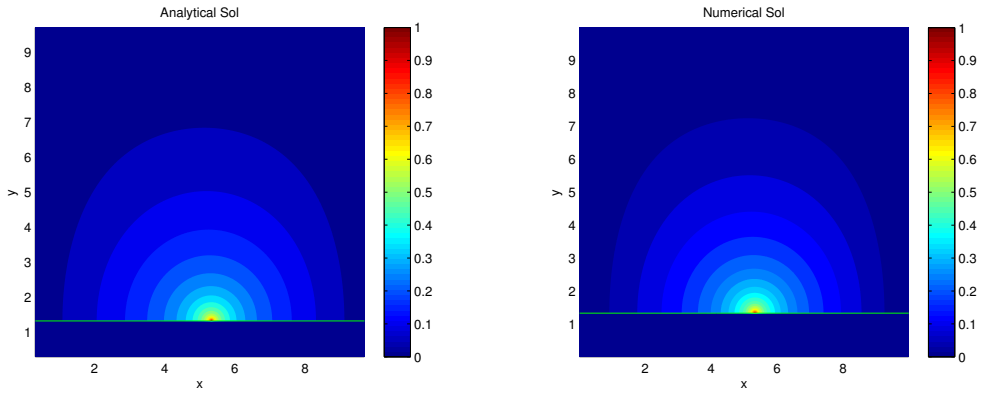

FIGURE 2.10. Contours of the analytical (**left**) and numerical (**right**) solutions of the elliptic problem on the rectangular domain on 512×512 grid with the delta function centered at $(5.33, 1.33)$ on the bottom boundary (horizontal green line $y = 1.33$). The numerical solution is computed using a rescaled hat function approximation ($\varepsilon = 2h$).

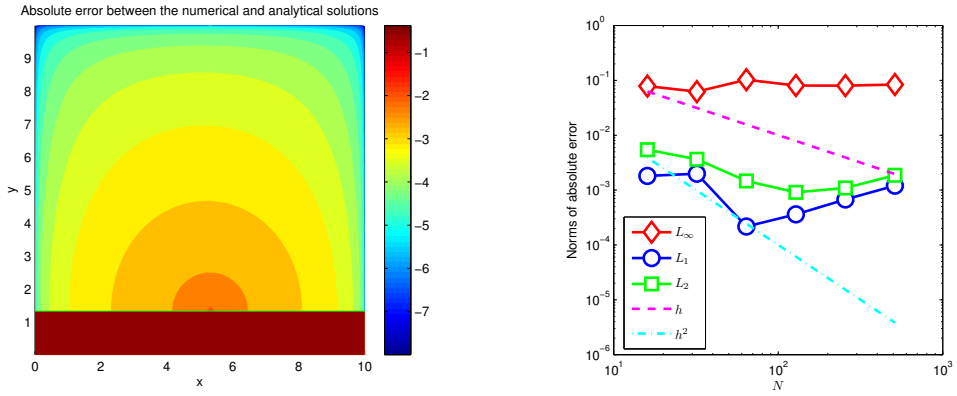

FIGURE 2.11. **Left:** Contours of the error in log scale between the analytical and numerical solution for the delta hat function approximation ($\varepsilon = 2h$) without rescaling. **Right:** Convergence of the error in 3 norms as the number of cells N increases (mesh size h goes to zero) for the hat delta approximation without rescaling.

to the analytical solution as shown in Figure 2.12. From the contours of the logarithm of the error in the left picture of Figure 2.12, it is clear that the main source of error remains in the neighborhood of the delta support here at $(5.33, 1.33)$. The error will always remain large where the singularity is which explains why the error does not converge in the max norm. On the other hand, the L_1-norm and the L_2-norm converge as h^2 and h respectively. These are the order of convergence we expect from the Embedded boundary method.

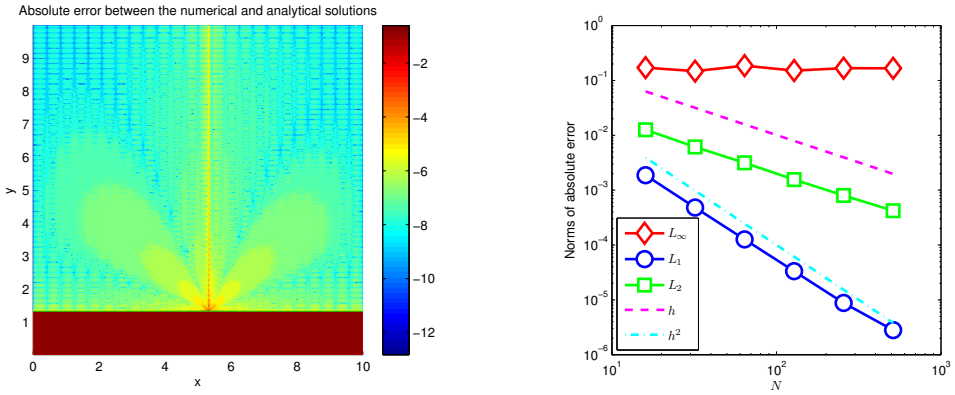

FIGURE 2.12. **Left:** Contours of the error in log scale between the analytical and numerical solution for the delta hat function approximation ($\varepsilon = 2h$) with rescaling. **Right:** Convergence of the error in 3 norms as the number of cells N increases (mesh size h goes to zero) for the hat delta approximation with rescaling.

2.4.1.2. *Irregular domain with sinusoidal bottom boundary*

In a second test, the domain is irregular and its bottom boundary is defined by a sinusoidal function:

$$h(x) = 2\sin\left(\frac{11x}{10} + 4\right) + 3 \tag{2.4.5}$$

Figure 2.13 presents the convergence of the numerical solutions to a reference solution computed on a 512×512 grid when the delta is positioned at $x^* = 4$ and $y^* = h(4)$. In both cases the delta was regularized with a Gaussian approximation (2.2.9) with $\varepsilon = 2h$. Clearly, the numerical solution converges for the regularization of the delta function with a Gaussian approximation in both cases, with and without rescaling. This might be explained by the fact that the support of the Gaussian approximation is much wider than for the hat approximation hence the regularization is less sensitive to the irregularity of the bottom boundary. The misalignment with the grid does not lead to order 1 error as for the hat approximation. The rescaling process allows to recover one order of convergence (from to h to h^2) in the L_1-norm.

2.4.2. 3D convergence analysis

The efficiency of the 3D rescaling algorithm is studied in the case of the elliptic problem. The convergence rate of the numerical solutions will be analyzed for different test setups. The first test is designed to compare the 2D numerical solution of the elliptic problem with a slice of the 3D solution of the extended problem. The purpose of this test is to show that the 3D rescaling process is analog to the 2D process

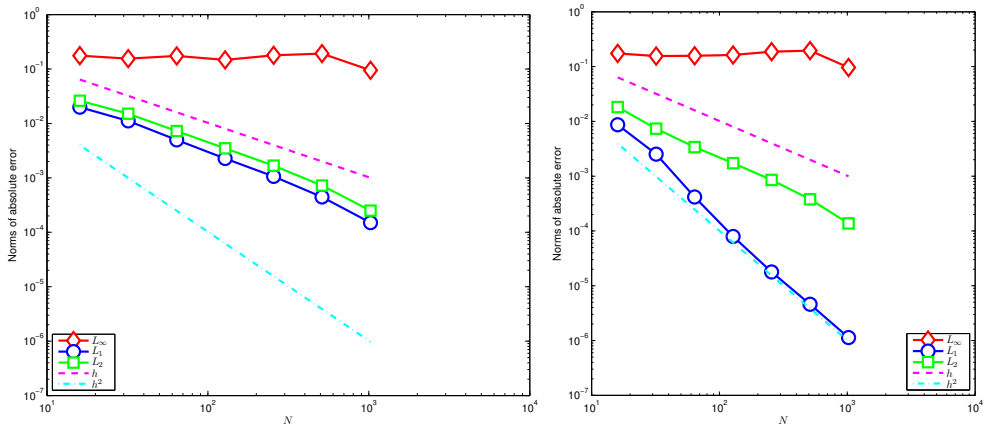

FIGURE 2.13. Convergence of the numerical solution of the Poisson problem on an irregular domain with sinusoidal bottom boundary. The numerical solution is computed with the delta Gaussian approximation $\varphi^G(\xi)$ without (**left**) and with (**right**) rescaling. The half-width of the support is $\varepsilon = 2h$.

for a particular setup. The second part presents the use of the rescaling algorithm in order to ensure the convergence of the numerical solution. The results are presented for two different codimension-2 manifolds and for two different geometries of the bottom boundary of the computational domain.

2.4.2.1. *Pseudo-3D test for 2D comparison*

This experiment is designed to show that the line segment 3D rescaling algorithm is in fact a generalization of the 2D rescaling process. Consider a straight horizontal line which can be seen as a natural extension of the codimension-2 manifold in 2D. A cross-section of a line is simply a point. A rectangular domain (without an embedded irregular bottom boundary) is used in both cases. For the 3D case, the codimension-2 manifold is a straight horizontal line, lying at the bottom boundary of the domain ($y^* = 0$), such that it is aligned at $x^* = 5.33$. The manifold is defined as the intersection of the level functions

$$u^1(x,y,z) = x - 5.33, \tag{2.4.6}$$

$$u^2(x,y,z) = z. \tag{2.4.7}$$

The hat approximation $\varphi^L(\xi)$ for the delta function is used with a half-support of $\varepsilon = 2.1h$, since a non-integer factor of the mesh size is problematic for the convergence. Figure 2.14 shows the volumetric plot of the discretized delta function supported on the horizontal line for a uniform mesh grid. The delta function has zero value (dark blue) everywhere in the domain but on the line (yellow and turquoise). A 2D perpendicular slice to this manifold will correspond to the 2D case, where the

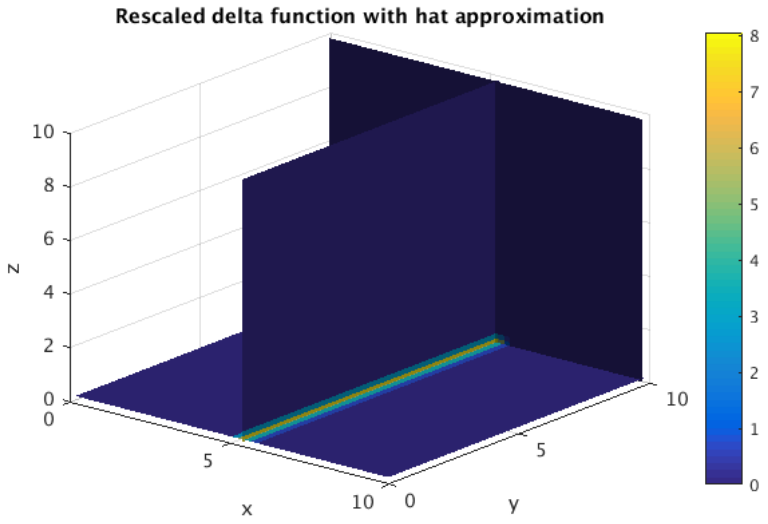

FIGURE 2.14. Regularized delta function supported on a horizontal line on a $N = 50$ mesh grid defined by equation (2.3.9) with half-width supports $\varepsilon_1 = \varepsilon_2 = 2.1h$. Plane slices at $x = 5$, $y = 10$ and $z = h = 0.2$.

manifold is simply a point centered at $(5.33, 0)$. This choice of the x coordinate of the manifold makes sure it is not aligned with the grid as the mesh is refined. The boundary conditions for the elliptic problem (2.1.3) in 2D and 3D are the same on top and bottom but periodic boundary conditions are applied to the two sides of the domain that are crossed by the horizontal line. This particular setup guarantees that a slice of the 3D solution of the elliptic problem will correspond to the 2D solution where the delta is centered at the point $(x^*, y^*) = (5.33, 0)$. Figure 2.15 shows the solution of the 3D elliptic problem with the periodic boundary conditions applied. The 3D rescaling algorithm lead to the same results as the 2D rescaling for this particular setup of the horizontal line manifold with appropriate periodic boundary conditions. This is shown in Figure 2.16. A cross section slice of the 3D solution is shown in the left picture. The difference between the 2D solution and a slice of the 3D solution obtained with their respective delta rescaling algorithm is presented in the right picture. Note that the error between the two solutions is of order 10^{-10} which is the same order as the tolerance for the iterative solver of the 3D problem.

The convergence of the error can be compared for solutions of the 2D problem and a slice of the solutions of the 3D problem. The reference solutions used for the convergence tests were computed on a $N = 256$ grid. Results for the regularized delta functions with and without rescaling are shown in Figure 2.17. The blue curves represent the convergence rate of the regularized delta function with rescaling for both the 2D and sliced 3D solutions (they coincide). The same stands for the orange curves in Figure 2.17. This can be expected since a $xy-$slice of the solution

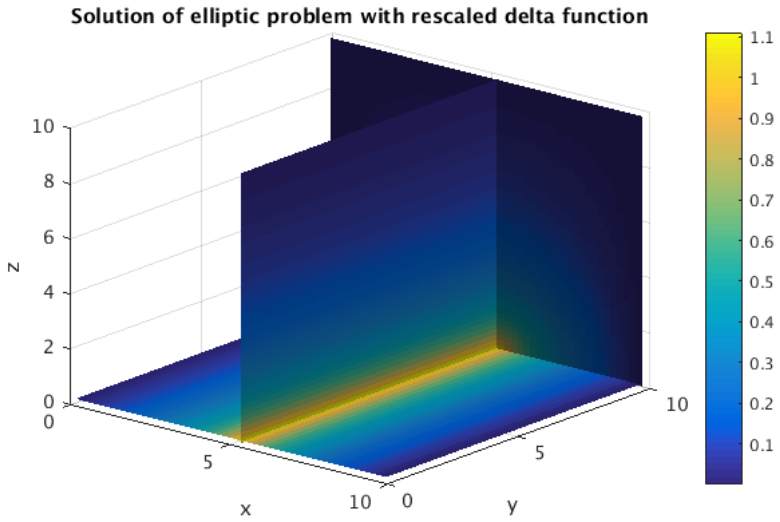

FIGURE 2.15. Solution of the elliptic problem in 3D on a $N = 50$ mesh grid with periodic boundary conditions applied on domain sides crossed by the line source. Plane slices at $x = 5$, $y = 10$ and $z = h = 0.2$.

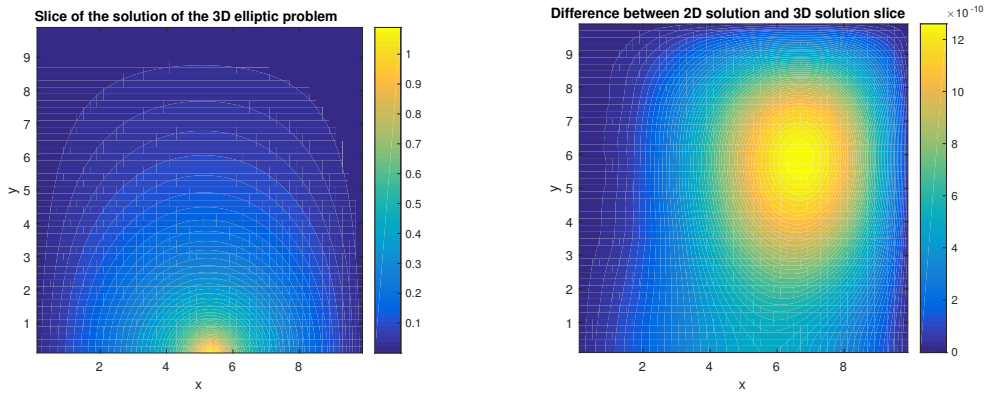

FIGURE 2.16. Cross section of the 3D solution (**left**) and error between the 2D solution and a slice of the 3D solution (**right**).

for the 3D problem is the same as the solution of the 2D problem. Note that there is no convergence in the L_1 and L_2 norms for the case where the rescaling is not applied on the delta. The rescaling algorithm allows the convergence in both the 2D and 3D cases for these two norms as shown by the blue curves. There is a small gain also in the max norm which is slightly decreasing with the mesh refinement. The rate of convergence of the error is order h in the L_2 norm and about order h^2 in the L_1 norm.

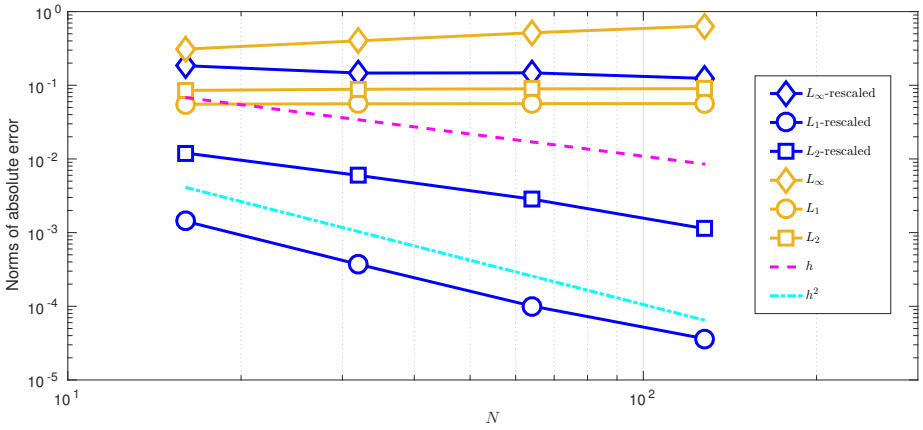

FIGURE 2.17. Plot of the convergence of the error between the numerical solution and the reference (numerical) solution ($N = 256$) for the 2D case and (slice of) the 3D case for hat approximations of the delta function with and without rescaling.

2.4.2.2. *Tests setup*

The rescaling algorithm is now tested in a more general setting. The tests are conducted with two different codimension-2 manifolds and two bottom boundary geometries on a cubic domain of sides $[0,10]$. The bottom boundary is given as a height function $h(x,y)$, but it can be defined as a level set function in this manner:

$$u^1(x,y,z) = z - h(x,y). \tag{2.4.8}$$

The irregular bottom boundary is defined as the sine function:

$$h_{sine}(x,y) = 1.666\sin(x+4)+2; \tag{2.4.9}$$

which does not depend on y. This function is pictured in Figure 2.18. The regular domain is defined with a horizontal plane for the bottom boundary:

$$h_{regular}(x,y) = 0. \tag{2.4.10}$$

The projection in the $xy-$plane of the first manifold is a circle of radius 2, centered in the middle of the domain at $(x,y) = (5,5)$. It is defined by the following level set function which is a signed distance function:

$$u^2_{circle}(x,y,z) = \sqrt{(x-5)^2+(y-5)^2}-2. \tag{2.4.11}$$

The second level set function is a "deformation" of the circle case. Its projected zero level set has a smooth "shoe" shape. It is defined by the following function which is

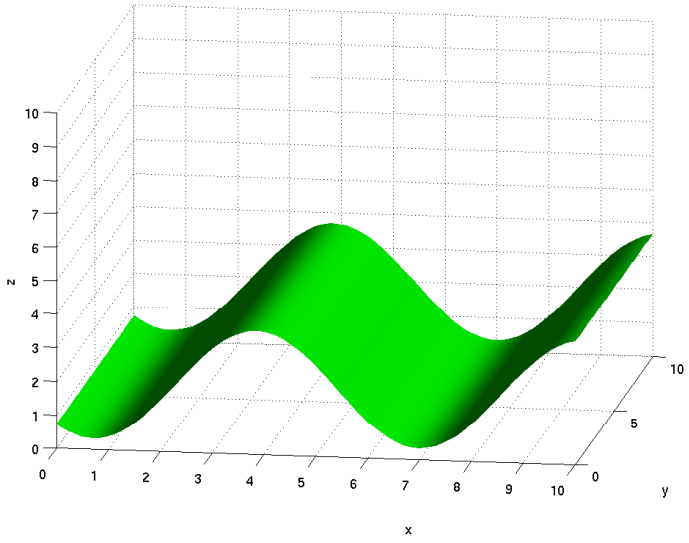

FIGURE 2.18. 3D plot of the sine function defined by equation 2.4.9.

not a signed distance function:

$$u^2_{shoe}(x,y,z) = \sqrt{(x-5)^2 + \frac{x}{3}(y-5)^2 + 5\sin(x)\sin(y)} - 2. \tag{2.4.12}$$

The zero level curves of these two functions are plotted in Figure 2.19. The motivation for using these two curves is to be able to compare the behavior of the rescaling algorithm when it is used on a symmetric and convex curve (circle) and on a curve with concavities and no symmetry (shoe). It is important to note that the

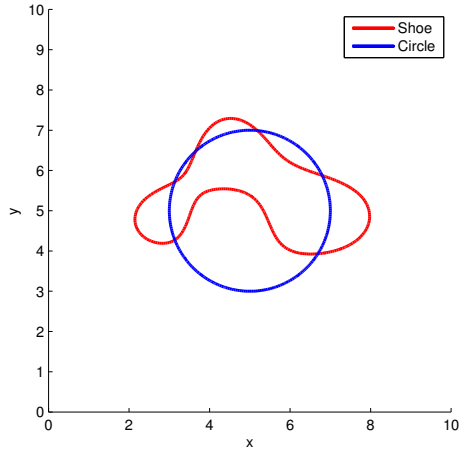

FIGURE 2.19. Contour of the "shoe" and circle codimension-2 manifolds in the xy-plane.

codimension-2 manifold, for the circle and sine level function case, will not have

the designated form when the level function u^1 defined with the sine height function h_{sine} is used. Only their projection in the $xy-$plane will always correspond to the shape of their name. In order to be able to define the delta function correctly, the circle and shoe curve will be projected back to the bottom boundary (topography). The level set function $u^2(x,y,z,t)$ is projected back onto the bottom boundary $h(x,y)$. This leads to an analog level set function
$u_h^2(x,y,z=h(x,y),t)$. The intersection of the zero level set of the functions u_h^2 and u^1 will define the codimension-2 manifold on the bottom boundary of the irregular domain. The delta will be regularized either with the Gaussian approximation (2.2.9) or the hat approximation (2.2.2) with $\varepsilon = 2h$ using the product formula (2.3.9). For different combinations of the delta approximation, manifold and bottom geometry, the convergence will be tested using the rescaling algorithm.

2.4.2.3. *Circle curve*

This subsection presents the study when the delta function is regularized on a codimension-2 manifold for which the projection is a circle in the $xy-$plane. The first convergence test is done on the regular bottom boundary with the delta regularized with the Gaussian approximation. Figure 2.20 shows the volumetric plot of the reference solution $N = 256$ for this setup. The codimension-2 manifold has the circle shape since it lies on the horizontal plane and the slice in the x and y plane crossing the center of the domain are perfectly symmetric. Figure 2.21 shows the

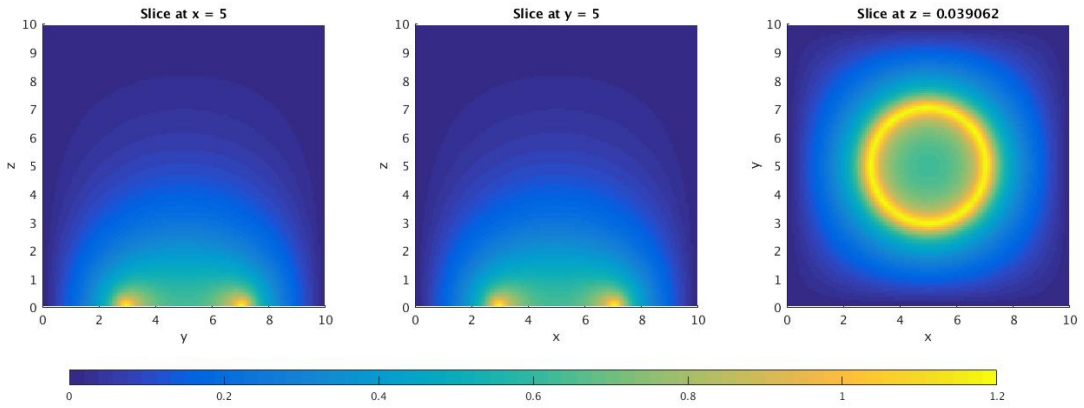

FIGURE 2.20. Slices of the numerical solution of the elliptic problem with the rescaled delta source supported on a manifold which has a circle projection. The bottom boundary is defined by a horizontal plane and the delta approximation is the Gaussian $\varphi^G(\xi)$.

convergence rates in the L_1 and L_2 norms are slightly better than h. The max norm decreases slowly but not as h. Figures 2.22 and 2.23 present the reference solutions

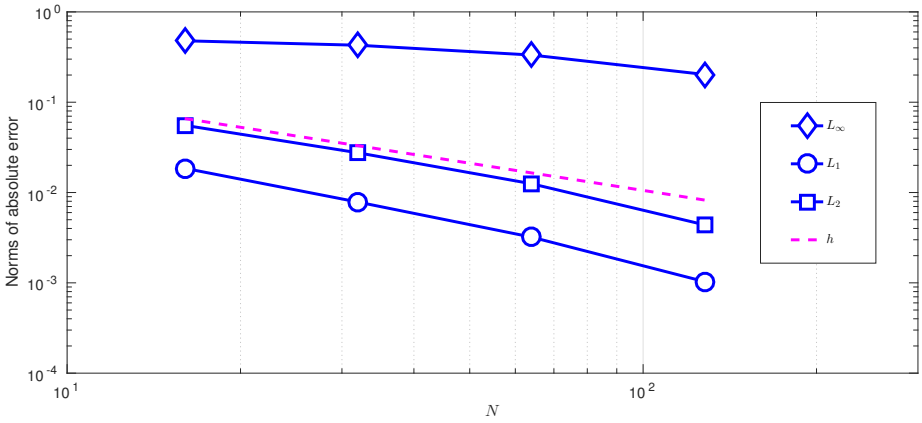

FIGURE 2.21. Convergence of the error between the reference numerical solution and the numerical solution of the elliptic problem with the rescaled delta source supported on a manifold which has a circle projection. The bottom boundary is defined by a horizontal plane and the delta approximation is the Gaussian $\varphi^G(\xi)$.

for the irregular sine bottom boundary when the delta is regularized with the hat and Gaussian approximation respectively. The slices in the x of the solution show that the symmetry has been preserved in that direction since the topography does not change in the y direction. The slice in the y plane shows that the 3D representation of the manifold is not a circle anymore. The main difference between the two figures is the value of the solution near the manifold. Since the Gaussian approximation has a stronger smoothing of the delta function, the final solution in this case has a lower value near the manifold than the solution in the hat approximation case. The convergence rates of the error between the reference solution and the numerical solutions of the elliptic problem with the hat and Gaussian approximations for the delta function are shown in Figures 2.24 and 2.25. One can note that, in both cases, the error converges in the L_1 and L_2 norms when the rescaling algorithm is applied. The order of the error and the convergence rates are the same for both the hat and Gaussian approximations. The convergence rate as a function of h is pictured by the magenta line. The L_1 norm converges at this rate and the L_2 norm converges almost at the same rate. The rates in these two norms for the Gaussian case are a little less than what was observed in Figure 2.21 for the regular domain case. The changes in the grid representation of the bottom sine boundary at each mesh refinement might cause this little discrepancy with the regular domain. The major difference is in the L_∞ norm. In Figure 2.21 for the regular domain case, the max norm is decreasing. Its rate is less than h, but there was an improvement with the mesh refinement. In Figures 2.24 and 2.25, the max norm remains constant as

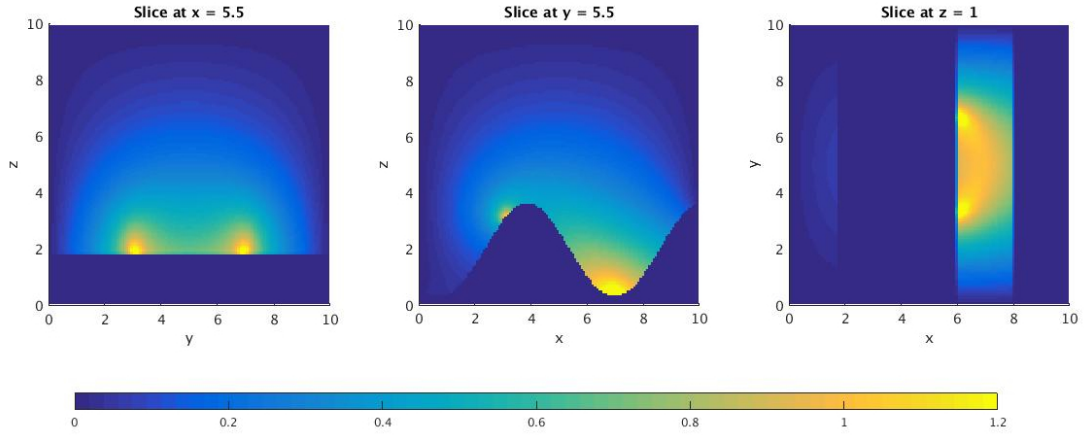

FIGURE 2.22. Slices of the numerical solution of the elliptic problem with the rescaled delta source supported on a manifold which has a circle projection. The bottom boundary is defined by a sine function and the delta approximation is the hat $\varphi^L(\xi)$.

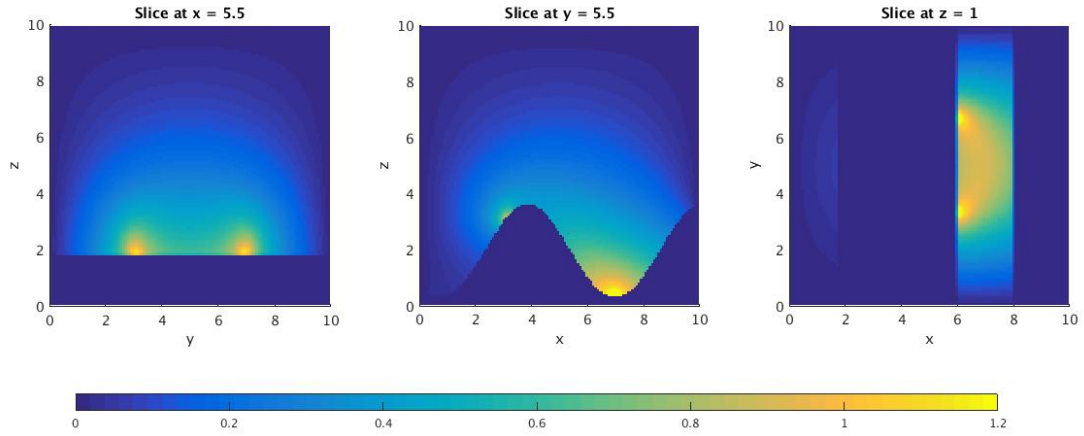

FIGURE 2.23. Slices of the numerical solution of the elliptic problem with the rescaled delta source supported on a manifold which has a circle projection. The bottom boundary is defined by a sine function and the delta approximation is the Gaussian $\varphi^G(\xi)$.

h goes to zero. The changes in the representation of geometry are the most plausible explanation for this behavior. As in the pseudo-3D case, these tests show that the rescaling algorithm, which forces the delta function to satisfy the first moment condition of equation 2.2.16, ensures the convergence of the error in the L_2 and L_1 norms.

2.4.2.4. *Shoe curve*

The same experiments conducted in the previous subsection are now presented for the case where the projection of the codimension-2 manifold has a shoe shape

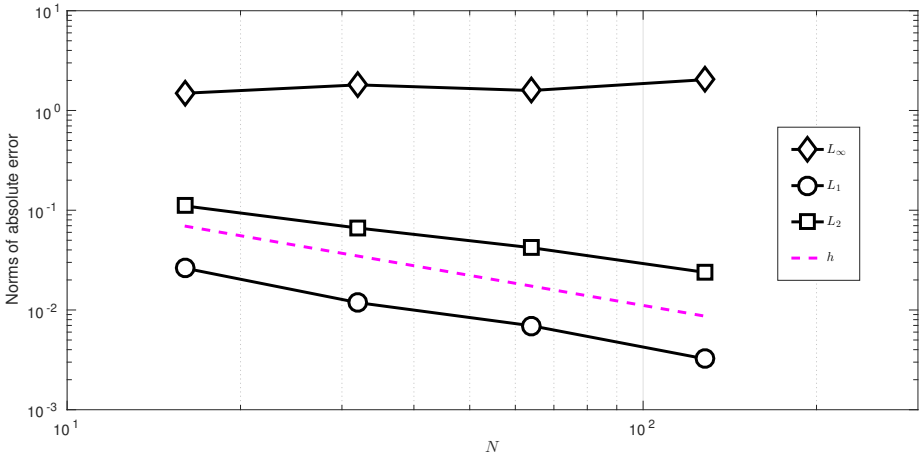

FIGURE 2.24. Convergence of the error between the reference numerical solution and the numerical solution of the elliptic problem with the rescaled delta source supported on a manifold which has a circle projection. The bottom boundary is defined by a sine function and the delta approximation is the hat $\varphi^L(\xi)$.

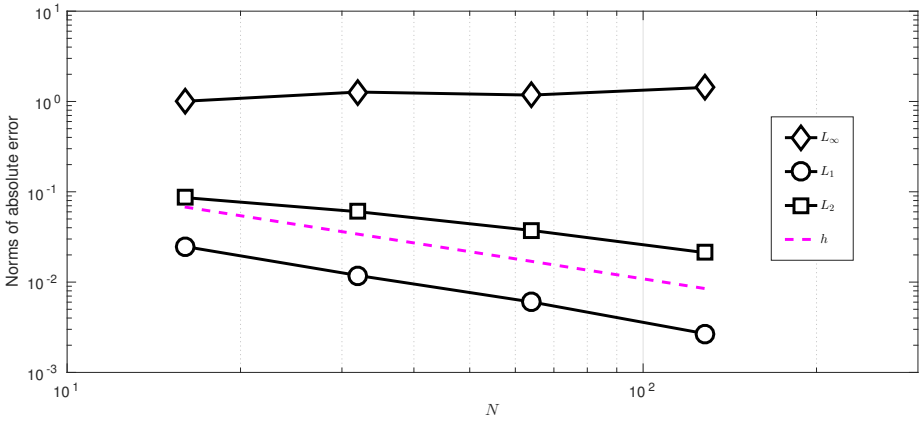

FIGURE 2.25. Convergence of the error between the reference numerical solution and the numerical solution of the elliptic problem with the rescaled delta source supported on a manifold which has a circle projection. The bottom boundary is defined by a sine function and the delta approximation is the Gaussian $\varphi^G(\xi)$.

in the $xy-$plane, a deformation of the circle. The first experiment is conducted in a regular domain where the bottom boundary is a horizontal plane and the delta function is regularized with the Gaussian approximation. Figure 2.26 shows the volumetric plot of the reference solution $N = 256$ for this setup. The codimension-2 manifold has a shoe shape on the horizontal plane which can be seen in the z slice.

The slices in the x and y plane crossing the domain center do not have any symmetry. The loss of symmetry of the codimension-2 manifold with the grid does not

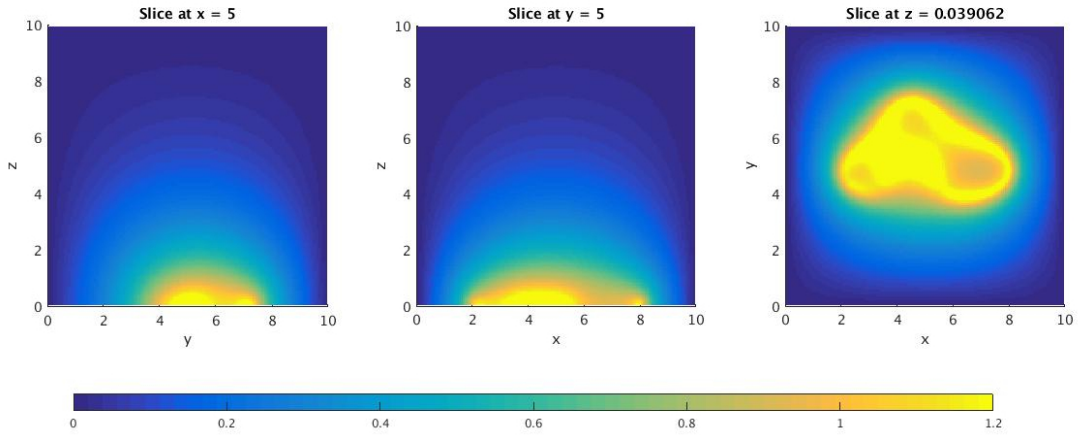

FIGURE 2.26. Slices of the numerical solution of the elliptic problem with the rescaled delta source supported on a manifold which has a *shoe* projection. The bottom boundary is defined by a horizontal plane and the delta approximation is the Gaussian $\varphi^G(\xi)$.

alter the convergence rates nor the order of the error between the reference and numerical solutions. The results shown in Figure 2.27 are almost identical to the curves presented in Figure 2.21. The error converges as h in the L_1 and L_2 norms and the max norm slowly decreases as h tends to zero. The reference solutions for

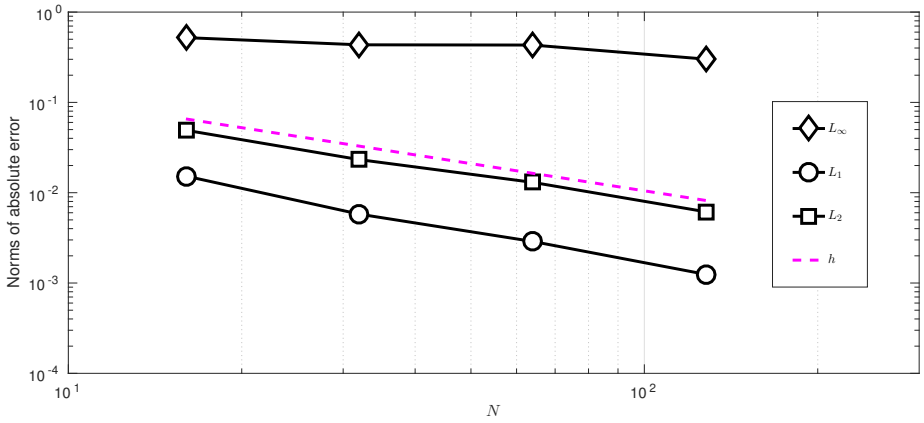

FIGURE 2.27. Convergence of the error between the reference numerical solution and the numerical solution of the elliptic problem with the rescaled delta source supported on a manifold which has a *shoe* projection. The bottom boundary is defined by a horizontal plane and the delta approximation is the Gaussian $\varphi^G(\xi)$.

the irregular sine bottom boundary when the delta is regularized with the hat and

Gaussian approximation are shown in Figures 2.28 and 2.29 respectively. The three slices show that the manifold on which the delta function is regularized has no symmetry. There is a slight difference between the two solutions of the elliptic problem obtained with the two delta approximations. The hat approximation with its narrow support keeps the delta function more concentrated along the manifold than the Gaussian approximation. This explains the higher value near the manifold of the elliptic solution obtained with the hat approximation.

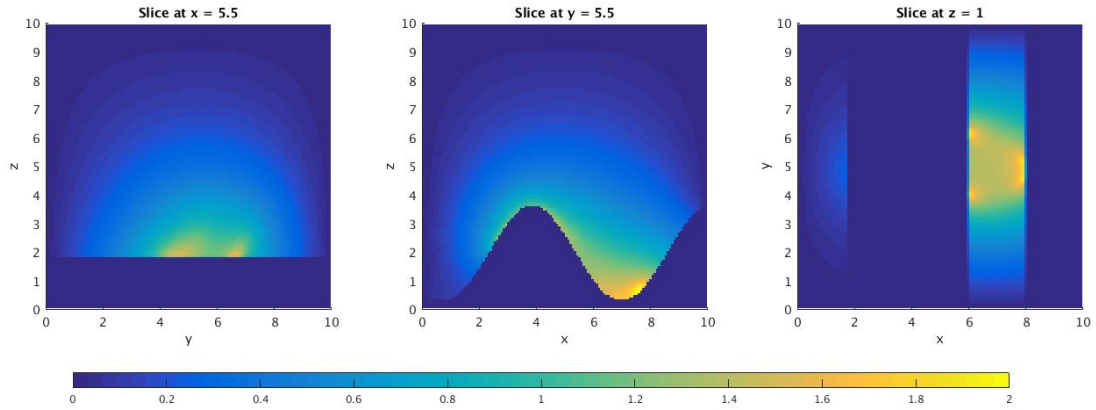

FIGURE 2.28. Slices of the numerical solution of the elliptic problem with the rescaled delta source supported on a manifold which has a *shoe* projection. The bottom boundary is defined by a sine function and the delta approximation is the hat $\varphi^L(\xi)$.

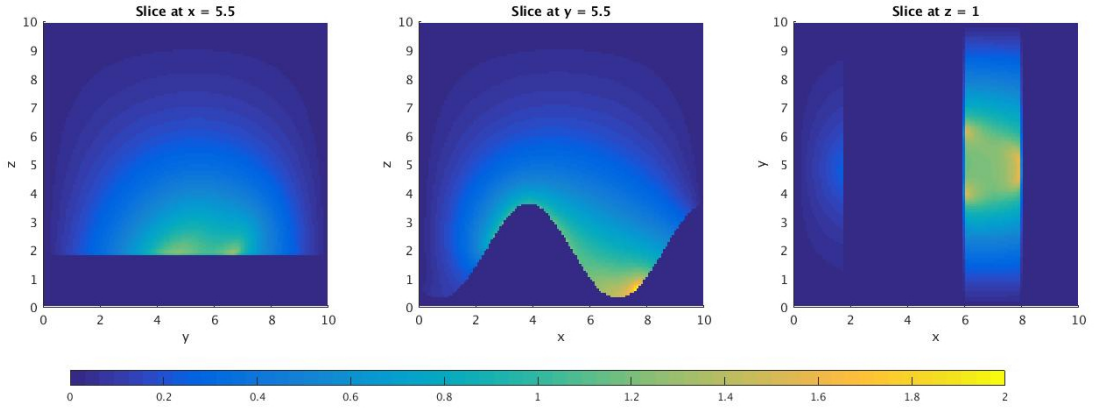

FIGURE 2.29. Slices of the numerical solution of the elliptic problem with the rescaled delta source supported on a manifold which has a *shoe* projection. The bottom boundary is defined by a sine function and the delta approximation is the Gaussian $\varphi^G(\xi)$.

Figures 2.30 and 2.31 show the convergence rate of the error between the reference solution and the numerical solution of the elliptic problem when the delta

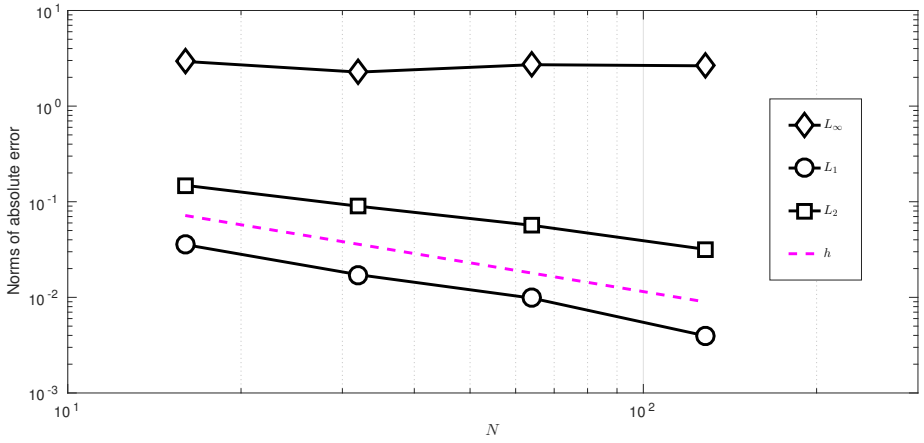

FIGURE 2.30. Convergence of the error between the reference numerical solution and the numerical solution of the elliptic problem with the rescaled delta source supported on a manifold which has a *shoe* projection. The bottom boundary is defined by a sine function and the delta approximation is the hat $\varphi^L(\xi)$.

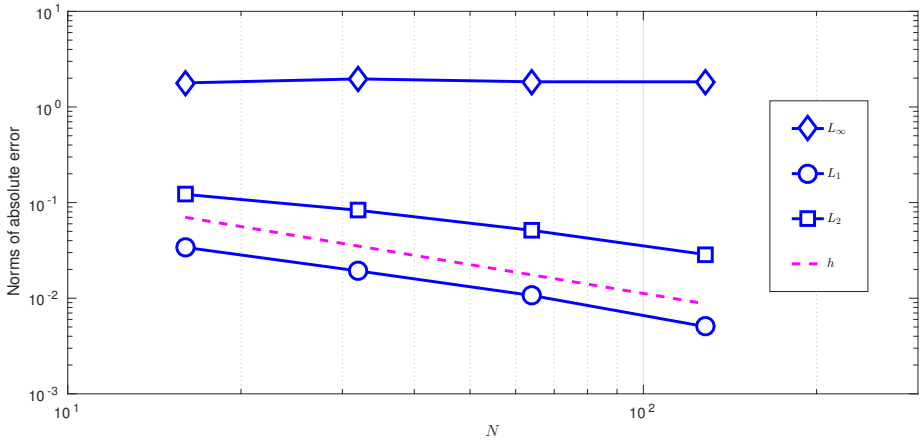

FIGURE 2.31. Convergence of the error between the reference numerical solution and the numerical solution of the elliptic problem with the rescaled delta source supported on a manifold which has a *shoe* projection. The bottom boundary is defined by a sine function and the delta approximation is the Gaussian $\varphi^G(\xi)$.

function is regularized with the hat and Gaussian approximations respectively. There are some analogies with the circle case. First, the convergence rates of the error in the three norms are almost the same with both approximations of the delta function. They have the same order for the error and the same rates of convergence. The convergence rate in the L_1 norm is of order h and slightly slower in the L_2 norm. The error in the max norm remains constant with mesh refinement. The order of

the error in Figure 2.31 is higher than in Figure 2.27 for all three norms. The irregular geometry of the domain with the sine bottom boundary explains this difference. The convergence rates remain the same in the L_1 and L_2 norms between the circle and shoe cases. The main difference between Figures 2.31 and 2.25 is the value of the error. For a given mesh refinement, the order of the error is bigger for the shoe curve than for the circle curve. There are some general remarks that can be stated. The rescaling algorithm always ensures the convergence of the error in the L_1 and L_2 norms. For the circle and shoe cases, the convergence rate in these two norms is of order h. There are two factors that can explain the small variations in the order of the error. First, the elliptic problem can have an irregular bottom boundary. The error is dependent on the accuracy of the geometry representation which can introduce an error of order h^2. The second factor is the symmetry of the codimension-2 manifold. For instance, the circle on the horizontal plane bottom boundary. This symmetry can help the order of the error because of potential error cancellations. This cannot happen in the case of the shoe curve. Regardless of the factor, neither change the rates of convergence of the error. A look at the convergence rates of the pseudo-3D test (Figure 2.17) and the 2D irregular domain test (Figure 2.13) shows that the L_1 norm has a rate of order h^2 rather than order h in the more complex test cases. This is explained by the line segment representation of the manifold, the support of the delta function. In 2D, the codimension-2 manifold is only a point, hence its discrete representation does not change with grid refinement. The same logic applies for the pseudo-3D case, where the straight horizontal line is aligned with the mesh grid. Because of the mesh refinement in 3D, the line segments of the discretized curves will differ on each mesh. This directly affects the regularization of the delta function since the rescaling algorithm uses the length of each line segment to rescale the local amplitude of the delta function.

2.5. Conclusions

This article dealt with the regularization of delta functions on codimension-2 manifolds. Particularities of the considered elliptic problem are the irregularity of the computational domain and the delta function lying on the irregular bottom boundary. The regularization of the delta function on the codimension-2 manifold took advantage of the representation of the manifold as the intersection of two level set functions. The delta function is then defined as the product of two delta functions, each one supported on a level set function. The regularized delta function must fulfill the first moment condition. This property is sufficient to guarantee the convergence of the numerical solutions of an elliptic problem. This condition was first enforced for the 2D problem by using a direct rescaling process. This rescaling

was then extended in 3D using a local line segment rescaling. After assigning each grid point of the domain to the closest line segment of the projected manifold, the delta weights at these points for a given segment were rescaled such that their sum equals the length of the segment. A pseudo-3D test showed that this algorithm was a natural extension of the 2D process and could achieve the same convergence rates. The algorithm was tested in a more general setting for three-dimensional domains. Convergence of the error between the reference and numerical solutions was achieved in all cases for the L_1 and L_2 norms when applying the rescaling algorithm. The irregularity of the bottom boundary and the change of the line segment representation of the codimension-2 manifold decrease the convergence rate in the L_1 norm from h^2 to h. The assignment of the points to the closest line segment is basically brute force. One could improve this algorithm by using the signed distance property of the level set functions to assign the point to the closest segment. Since most delta approximations have compact supports (one can truncate the support of the Gaussian approximation since it decreases rapidly), only these points need to be taken care of the rescaling process and not the points in the whole domain.

APPENDIX 2.A. ANALYTICAL SOLUTION OF THE ELLIPTIC PROBLEM ON A RECTANGULAR DOMAIN

It is possible to construct an analytical solution of the following elliptic problem on a rectangular domain Ω in 2D:

$$\Delta\Phi = \delta(x-\xi, y-\eta) \quad \text{in } \Omega \tag{2.5.1}$$

$$\Phi = 0 \quad \text{on } \partial\Omega. \tag{2.5.2}$$

This elliptic problem is known as the fundamental problem. The method of eigenfunctions is used in order to find an analytic Green function that satisfies this problem with Dirichlet boundary conditions. We consider the associated eigenvalue problem:

$$\Delta\phi + \lambda\phi = 0 \quad \text{in } \Omega \tag{2.5.3}$$

$$\phi = 0 \quad \text{on } \partial\Omega. \tag{2.5.4}$$

Let ϕ_{mn} be the eigenfunctions and λ_{mn} the eigenvalues. We can then expand $\Phi \equiv G$ and δ in terms of the eigenfunctions:

$$G(x,y;\xi,\eta) = \sum_m \sum_n a_{mn}(\xi,\eta)\phi_{mn}(x,y) \tag{2.5.5}$$

$$\delta(x-\xi, y-\eta) = \sum_m \sum_n b_{mn}(\xi,\eta)\phi_{mn}(x,y) \tag{2.5.6}$$

where

$$b_{mn} = \frac{1}{\|\phi_{mn}\|^2} \iint_\Omega \delta(x-\xi, y-\eta)\phi_{mn}(x,y)\,dx\,dy \tag{2.5.7}$$

$$= \frac{\phi_{mn}(\xi,\eta)}{\|\phi_{mn}\|^2} \tag{2.5.8}$$

in which

$$\|\phi_{mn}\|^2 = \iint_\Omega \phi_{mn}^2\,dx\,dy. \tag{2.5.9}$$

Substituting in the equation of the Green function and knowing that

$$\Delta\phi_{mn} + \lambda_{mn}\phi_{mn} = 0, \tag{2.5.10}$$

$$-\sum_m \sum_n \lambda_{mn} a_{mn}(\xi,\eta)\phi_{mn}(x,y) = \sum_m \sum_n \frac{\phi_{mn}(x,y)\phi_{mn}(\xi,\eta)}{\|\phi_{mn}\|^2}. \tag{2.5.11}$$

Hence,

$$a_{mn}(\xi,\eta) = \frac{\phi_{mn}(x,y)}{\lambda_{mn}\|\phi_{mn}\|^2} \tag{2.5.12}$$

and the Green function is given by

$$G(x,y;\xi,\eta) = -\sum_m \sum_n \frac{\phi_{mn}(x,y)\phi_{mn}(\xi,\eta)}{\lambda_{mn}\|\phi_{mn}\|^2}. \tag{2.5.13}$$

We can thereafter use this to find the Green function on a rectangular domain. Let's consider the domain $\Omega = \{0 < x < L, \quad 0 < y < H\}$. We assume that the solution $\Phi(x,y)$ can be found using the separation of variables, i.e. $\Phi(x,y) = X(x)Y(y)$. Substituting in the eigenvalue problem, we find the two following equations:

$$X'' + \alpha^2 X = 0 \tag{2.5.14}$$

$$Y'' + (\lambda - \alpha^2)Y = 0 \tag{2.5.15}$$

where α^2 is a separation constant and with the homogeneous boundary conditions $X(0) = X(L) = 0$ and $Y(0) = Y(H) = 0$. The functions X and Y are then

$$X_m(x) = A_m \sin\left(\frac{m\pi x}{L}\right) \tag{2.5.16}$$

$$Y_n(y) = B_n \sin\left(\frac{n\pi y}{H}\right). \tag{2.5.17}$$

The eigenvalues are

$$\lambda_{mn} = \pi^2\left(\frac{m^2}{L^2} + \frac{n^2}{H^2}\right) \tag{2.5.18}$$

and the eigenfunctions are

$$\phi_{mn}(x,y) = \sin\left(\frac{m\pi x}{L}\right)\sin\left(\frac{n\pi y}{H}\right). \tag{2.5.19}$$

We can compute the norm of the eigenfunctions:

$$\|\phi_{mn}\|^2 = \int_0^L \int_0^H \sin^2\left(\frac{m\pi x}{L}\right)\sin^2\left(\frac{n\pi y}{H}\right)dxdy = \left(\frac{LH}{4}\right). \tag{2.5.20}$$

Substituting everything in the formula for the Green function, we find

$$G(x,y;\xi,\eta) = -\frac{4LH}{\pi^2}\sum_{m=1}^{\infty}\sum_{n=1}^{\infty}\frac{\sin\left(\frac{m\pi x}{L}\right)\sin\left(\frac{n\pi y}{H}\right)\sin\left(\frac{m\pi\xi}{L}\right)\sin\left(\frac{n\pi\eta}{H}\right)}{m^2H^2+n^2L^2}. \tag{2.5.21}$$

This Green function is valid for the domain $\Omega = \{0 < x < L, \quad 0 < y < H\}$. If the delta function is located at the bottom boundary, i.e. $\eta = 0$, then the Green function $G(x,y;\xi,\eta = 0) = 0$. Hence, we need to shift the domain in order to have the Green function defined over $\Omega = \{0 < x < L, \quad -H/2 < y < H/2\}$. This corresponds only in a shift of the eigenfunctions in y, so the Green function we are looking for is

$$G(x,y;\xi,\eta) = -\frac{4LH}{\pi^2}\sum_{m=1}^{\infty}\sum_{n=1}^{\infty}\frac{\sin\left(\frac{m\pi x}{L}\right)\sin\left(\frac{n\pi}{H}\left(y+\frac{H}{2}\right)\right)\sin\left(\frac{m\pi\xi}{L}\right)\sin\left(\frac{n\pi}{H}\left(\eta+\frac{H}{2}\right)\right)}{m^2H^2+n^2L^2}. \tag{2.5.22}$$

This solution is defined on a domain such as in Figure 2.32. In this article, the solution was needed only in the top half of this domain. The solution plotted in Figure

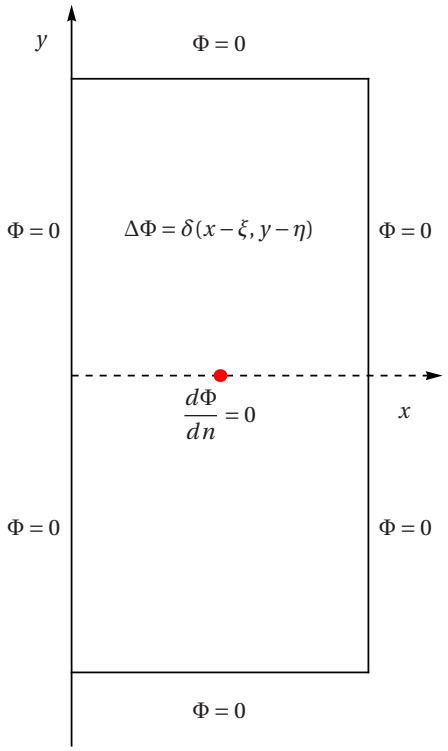

FIGURE 2.32. Poisson problem with delta function near the boundary (red dot).

2.33 is symmetric with respect to the $x-$axis and the homogeneous Neumann boundary condition will therefore be satisfied along this axis.

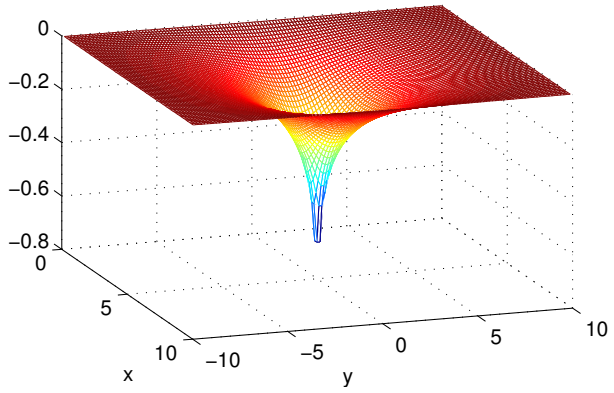

FIGURE 2.33. Analytical solution of the Poisson problem on the extended domain of Figure 2.32.

APPENDIX 2.B. CLOSEST LINE SEGMENT TO POINT ALGORITHM

The following brute-force algorithm is used for assigning each grid point to a line segment of the level curve. This algorithm can be easily implemented. In order to improve the computational efficiency, another algorithm could use the signed distance property of the level set function or the fact that delta function support is numerically compact. Given s_1 and s_2 two endpoints of a line segment s and a grid point p. Define the vectors $\mathbf{u} = \overrightarrow{s_1 s_2}$ and $\mathbf{v} = \overrightarrow{s_1 p}$. The orthogonal projection of p on span$\{\mathbf{u}\}$ written p_s is given by

$$p_s = s_1 + \frac{\mathbf{u}\cdot\mathbf{v}}{\mathbf{u}\cdot\mathbf{u}}\mathbf{u}. \tag{2.5.23}$$

Three cases are possible for computing the distance d between the point p and line segment s, depending on the value of the term $\alpha = \frac{\mathbf{u}\cdot\mathbf{v}}{\mathbf{u}\cdot\mathbf{u}}$:

(1) If $\alpha \in [0,1]$, then $p_s \in [s_1, s_2]$ and compute $d(p, p_s)$.

(2) If $\alpha < 0$, then $p_s \in [-\infty, s_1]$ and compute $d(p, s_1)$.

(3) If $\alpha > 1$, then $p_s \in [s_2, +\infty]$ and compute $d(p, s_2)$.

Once the distances between the point p and all the line segments have been computed, find the line segment for which the distance is minimal and assign the point p to this segment. The algorithm is applied to a blue curve in Figure 2.34. Each color band represents the points assigned to a line segment of the tooth-shaped curve.

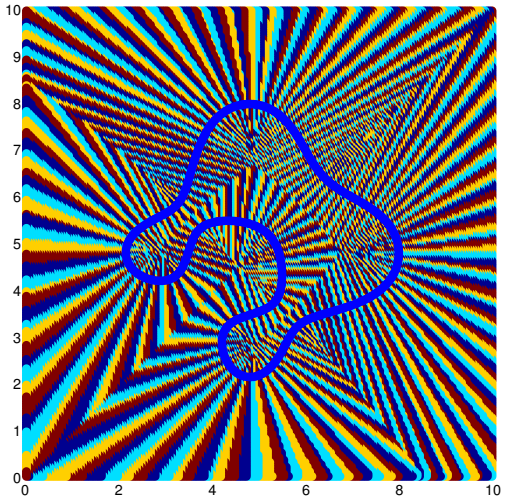

FIGURE 2.34. Illustration of the algorithm on a 200×200 grid for the blue tooth-shaped curve.

Chapitre 3

UN NOUVEAU MODÈLE COUPLÉ FEU-ATMOSPHÈRE POUR LA SIMULATION DE LA PROPAGATION DES FEUX DE FORÊT

Ce chapitre est constitué de l'article *A Novel Coupled Fire-Atmosphere Model for the Forecast of Forest Fire Spread*. L'objectif principal est de présenter un nouveau modèle couplé feu-atmosphère pour la prédiction des feux de forêt et d'étudier les régimes pour le cas en deux dimensions. Les contributions principales de l'article sont :

(1) un modèle atmosphérique basé sur une unique équation de divergence avec un terme source découlant d'une approximation à faible nombre de Mach ;

(2) un terme source représenté par une paire source-puits définie par des deltas de Dirac centrés sur des courbes ;

(3) une magnitude du terme source liée à la formule d'intensité de Byram ;

(4) une analyse adimensionnelle du modèle et une étude de cas en deux dimensions.

RÉSUMÉ

Cet article présente un modèle couplé feu-atmosphère pour la prévision de la propagation des feux de forêt. Le modèle atmosphérique est constitué d'une seule équation de divergence qui découle d'une approximation à faible nombre de Mach. Cette équation a un terme source qui prend en compte le taux de quantité de chaleur émise par le feu. Ce terme est représenté par une paire source-puits définie par des fonctions delta supportées sur des courbes. La paire permet de reproduire les principales caractéristiques d'un écoulement atmosphérique telles que les mouvements de circulation et les courants descendants près du panache de feu. La magnitude de la source est calculée localement avec le modèle de Byram pour l'intensité du feu. Le modèle pour le feu suit l'évolution du front à l'aide la méthode «level set».

Celle-ci est combinée au modèle de l'ellipse de Richards pour calculer la vitesse de propagation du feu. Une analyse dimensionnelle est effectuée afin de déterminer les différents régimes de propagation du feu.

A NOVEL COUPLED FIRE-ATMOSPHERE MODEL FOR THE FORECAST OF FOREST FIRE SPREAD

Louis-Xavier Proulx

ABSTRACT. This paper presents a coupled fire-atmosphere model for the forecast of wildfire spread. The atmosphere model is based on a single divergence equation derived from a low Mach number approximation. This equation has a source term which accounts for the fire heat release rate. This source term is represented as a singular sink-source pair perturbation defined with delta functions supported on level curves. The pair enables the reproduction of the core features of the wind flow such as downdraft and circulation motion near the fire plume. The source magnitude is computed locally with Byram's model for fire intensity. The fire model tracks the evolution of the fireline using the level set method. It is combined with Richards' ellipse model for computing the fire rate of spread. A dimensional analysis is conducted in order to determine the different regimes for the fire spread.

3.1. INTRODUCTION

Numerical models are an efficient tool for studying and forecasting the spread of wildland fires. Sullivan has shown in an extensive review [**96**, **97**, **98**] the diversity of the approaches for modeling the spread of wildfires. Recently, the study of the interactions and feedback between the fire front and the atmosphere has emerged as a major research topic. This has led to the development of coupled fire-atmosphere models. These models have established the necessity of coupling in order to achieve better predictions of wildfire spread.

Coupled fire-atmosphere models combine two sub-models, one governing the atmospheric flow and one for spreading the fire over the topography. These sub-models exchange information: the fire-induced wind influences the propagation of the fire and the fire feeds back into the wind flow with heat and combustion products.

The CAWFE model [**17**, **21**, **22**, **23**, **25**, **26**] developed by Clark *et al.* was among the first coupled models. This model was elaborated after the publication of two core papers [**19**, **20**] regarding the importance of fire-atmosphere coupling. They used the Clark-Hall non-hydrostatic mesoscale model [**18**] for the wind flow. The algorithms in model BEHAVE [**6**] are used for computing the fire rate of spreads. The model BURNUP [**2**] computes the burned fuel mass and the heat release by the fire. CAWFE uses a marker method for tracking the fire front.

The WRF-fire model [**15**, **24**, **64**, **65**, **66**, **77**, **91**, **92**] uses the *Weather Research and Forecasting Model* for atmospheric predictions. It is combined with the level set

method for the propagation of the fireline. Heat fluxes are computed using the difference in burned region areas between each time step. These fluxes are then injected in the atmospheric model in order to include the effects of the fire in the computation of the wind field. After some experiments, Beezley *et al.* [**14**] came to the conclusion that the mesoscale atmospheric model used by WRF-Fire to compute the wind flow over the topography was *"not designed for microscale simulations"*. They also noted that *"nesting initial atmospheric conditions from 32 km to 100 m cannot capture accurate local atmospheric features"*.

Filippi *et al.* [**41**, **42**] took an approach similar to Clark *et al.* [**17**] by combining two models: the mesoscale atmosphere model MesoNH [**54**] and ForeFire [**7**], a fire spread model. They studied the effects of the fire heat flux onto the atmosphere and the perturbed wind flow on the fire rate of spread. Using a fire spread model based on CAWFE, Sun *et al.* [**100**] coupled the model with the *University of Utah Large Eddy Simulation* (UU-LES) model. UU-LES includes turbulence in the resolution of the coupled model. Sun *et al.* showed with numerical experiments that *fire-induced convection appears to be the main contributor to the variability in the fire rate of spread and area burned.*

Physics models such as FIRETEC-HIGRAD [**16**, **29**, **39**, **58**, **59**, **60**, **61**, **62**, **63**, **64**, **69**, **79**, **80**] are convenient for studying specific characteristics in coupled models. The multi-phase transport approach coupled with a hydrodynamic atmosphere model brings precision to the modeling of wildfire spread. The complexity of this class of models makes them unusable for forecasting in a short period of time and the fine-scale data required by the model is usually not available.

Even if the use of a mesoscale atmospheric model might not seem appropriate in the context of prediction, previous coupled models have shown that fire-atmosphere interactions have a huge impact on forest fire spread and should not be neglected. This article presents a novel approach for coupling fire and atmosphere models. Mesoscale atmospheric models are computationally expensive and inefficient in reproducing the most important features of the flow. These reasons justify the development of a new atmospheric model. A divergence equation is derived from a low Mach number approximation for fire plumes. This single equation for the wind velocity field combines the continuity, energy and state equations.

The atmosphere model takes into account the heat feedback from the fireline. The approach taken for the inclusion of the feedback is consistent with the infinitely thin curve of the fireline. It is expressed as a singular source term in the divergence equation of the wind model. The local flow is perturbed by a sink-source pair given

by delta functions supported on the fireline interface. The amplitude of the pair depends locally on Byram's definition of the fire intensity. The fire model is based on Richard's ellipse model which uses the Huygens principle.

A dimensional analysis is conducted in order to find non-dimensional numbers characterizing the regimes of the propagation of the fire between plume-dominated and wind-dominated flow. The aim of this proposed model is to assess the importance of coupling in forecasting models to be used for fast predictions. A central question arising from this work is to what extent an appropriate coupling combined with a mass-consistent wind model can reproduce results similar to those of a full-atmosphere model. A better understanding of the parameters that affect the coupling will enable the development of more efficient and accurate simulation models for forest fires.

3.2. THE FIRE MODEL

The coupled model is designed as a forecasting tool for the spread of large-scale wildfires. In order to have a computationally time efficient model, some simplifications are made over the set of governing equations. For instance, the fine spatial and temporal resolutions of the flames are not required for spread purposes. This means that the equations governing the combustion and its chemical processes can be omitted by the fire model and larger time steps can be used for the simulations.

The common approach in wildfire forecasting models is to represent the fireline as an interface, which is an infinitely thin curve that outlines the burned and unburned fuel regions of the terrain. A numerical method tracks the evolution of the interface in time and its rate of spread is computed according to an empirical formula using local wind velocity, fuel bed type, topography slope and humidity. There are many different approaches for tracking interfaces, such as marker methods used in CAWFE [**17, 18, 20**], ForeFire [**42, 43**] and Prometheus [**112**]. The main drawback of these methods is that they cannot deal properly with topological changes of the fireline, such as the merging of two distinct fire fronts.

The model here is implemented with the level set method which was originally developed by Sethian [**90**] et Osher [**75**]. This method was successfully adapted by Foucault [**31**] and Barber *et al.* [**10**] for forest fire applications. The core idea behind the level set method consists of embedding the fireline interface as the zero level set of a higher dimensional function ϕ. Let $\mathbf{x}(t)$ be the trajectory of a particle on this interface. We require that the particle remain on the zero level set of the function ϕ at all time:

$$\phi(\mathbf{x}(t), t) = 0. \tag{3.2.1}$$

Differentiate this equation with respect to time t using the chain rule so that

$$\frac{\partial \phi}{\partial t} + \frac{d\mathbf{x}(t)}{dt} \cdot \nabla \phi = 0. \tag{3.2.2}$$

For a given time t, the term $\dfrac{d\mathbf{x}(t)}{dt}$ corresponds to the rate of spread $\mathbf{v}$ of the interface level set. Using the same argument for all the level sets of function ϕ, the equation becomes

$$\frac{\partial \phi}{\partial t} + \mathbf{v} \cdot \nabla \phi = 0. \tag{3.2.3}$$

Note that the level set equation (3.2.3) needs an initial condition in order to be solved. A signed distance function is used to initialize the function ϕ at time $t = 0$. If the velocity $\mathbf{v}$ is known, the level set describing the fireline can easily be spread over time.

Foucault adapted the level set method so that it combines Richards' ellipse model, also used by the Canadian model Prometheus [**10**] and the American model FARSITE [**44**]. Richards [**87**] has developed a model to compute the rate of spread for the propagation of wildfires based on Huygens' principle. Assume that each point of the fireline is in fact a newly ignited fire which grows as an ellipse aligned with the wind direction. The fireline at the next time step corresponds to the envelope of the ellipses as illustrated in Figure 3.1.

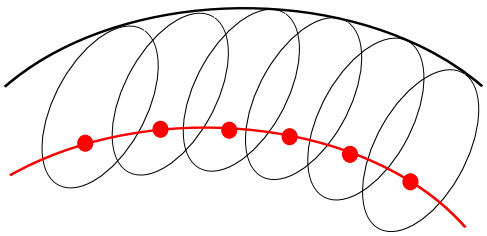

FIGURE 3.1. Fireline as the envelope of ellipses.

The ellipse model uses the parameters a, b and c, shown in Figure 3.2, that prescribe the growth of each ellipse. These parameters are computed locally and across the domain from the wind velocity magnitude. The wind feedback onto the fire rate of spread occurs with these parameters. The rate of spread in the wind direction is given by $a + c$, the back rate of spread is given by $a - c$ and the flank rate of spread, perpendicular to the wind direction, by b.

The matrix A below stores the propagation speeds a and b:

$$A = \begin{pmatrix} b & 0 \\ 0 & a \end{pmatrix} \cdot R_\theta \tag{3.2.4}$$

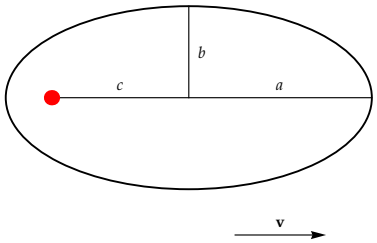

FIGURE 3.2. Parameters of the fire ellipse aligned in the wind direction.

and the vector C is the advection speed in the wind direction:

$$\mathbf{C} = R_\theta \begin{pmatrix} 0 \\ c \end{pmatrix} \tag{3.2.5}$$

where

$$R_\theta = \begin{pmatrix} \cos\theta & -\sin\theta \\ \sin\theta & \cos\theta \end{pmatrix} \tag{3.2.6}$$

is the matrix of rotation and θ is the wind direction with respect to the $y-$axis. Using this notation, the velocity field $\mathbf{v}$ is written as

$$\mathbf{v} = \frac{A^T A \nabla\phi}{\left|A\nabla\phi\right|} + \mathbf{C}. \tag{3.2.7}$$

The general level set equation (3.2.3) becomes the level set equation for the fire spread:

$$\frac{d\phi}{dt} + \left\|A\nabla\phi\right\| + \mathbf{C}\cdot\nabla\phi = 0. \tag{3.2.8}$$

A particular feature of this level set method adapted to wildfire spread is that it only requires the solution of the 2D problem for spreading the fire in the three-dimensional space. Rather than looking at the evolution of the curve over topography, the method looks at the projection of this curve in the $xy-$plane as shown in Figure 3.3. This enables a great improvement in the computational time for solving the level set equation. The details of this simplification are presented in Foucault's PhD thesis [**31**]. Techniques for dealing with obstacles and the narrow-band method for computational efficiency are described in Foucault's Master's thesis [**30**].

3.3. THE ATMOSPHERE MODEL

Many recent coupled models, such as Meso-NH/ForeFire [**41**, **42**, **54**], WRF-Fire [**64**, **65**, **93**] and HIGRAD-FIRETEC [**28**, **29**, **59**, **60**], use a mesoscale atmospheric model to generate the wind flow that propagates the fireline. Unfortunately, these

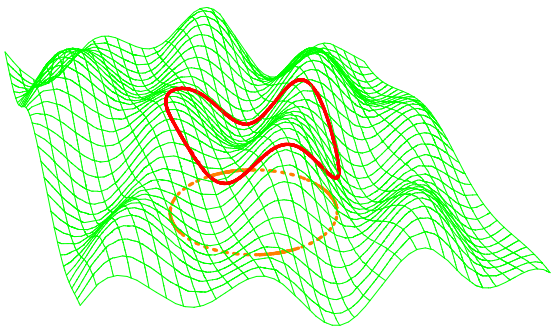

FIGURE 3.3. The level set method for tracking the fireline (red curve) on the topography is reduced to a 2D problem by looking at the fireline projection (orange circle) in the $xy-$plane.

models have two major drawbacks. First, the required computational time for solving the equations governing the atmospheric flow, particularly the conservation of momentum, is too intensive. Moreover, the computational domain mesh grid is too coarse for capturing small-scale features that might affect the wildfire spread. These issues mean that the current coupled models are not appropriate for short-term predictions.

Another approach is to use a simpler wind model, such as the mass-consistent models developed by Forthofer [**47**] and Proulx [**81**]. This class of models generates a divergence-free wind vector field that is tangent to the complex terrain and satisfies the continuity equation. This non-coupled approach is fast and numerically efficient, but the simplicity of the wind model cannot capture the local phenomena due to the lack of fire feedback on the flow.

The proposed wind model falls in-between the mass-consistent and mesoscale atmospheric wind models. This section details a quasi mass-consistent wind model with a fire feedback source. This model is based on a divergence equation with a source term derived from a low Mach number approximation. A projection method computes a wind velocity field satisfying this divergence equation. The geometric features of the topography are represented in the computational grid so that they may affect the wind flow. This atmosphere model is quasi-stationary, where the solution is assumed to readjust itself to the feedback.

3.3.1. A low Mach number approximation

The atmospheric flow generated by the model relies only on a divergence equation with a source term. The derivation of the divergence equation follows the work of Rehm and Baum [**11**, **12**, **13**, **84**, **85**] for a fire induced flow field. Mell *et al.* [**70**] have also used this approach. Trelles [**108**, **109**, **110**, **111**] pursued the same avenue

in his PhD thesis [**107**] for *Mass Fire Modeling of the 1991 Oakland Hills Fire*. He represented each fire zone as an individual plume.

The model is based on an approximation of a low Mach number M. The pressure p is decomposed into two terms:

$$p(\mathbf{x}, t) = p_0(z) + \tilde{p}(\mathbf{x}, t) \tag{3.3.1}$$

where p_0 is a far field ambient pressure and $\tilde{p}$ a small pressure perturbation such that $p_0/\tilde{p} = O(M^2)$. For this model, it is assumed that p_0 depends on the vertical z coordinate only and not on time t. A quantitative analysis of the general turbulent combustion equations was done by Trelles [**107**]. After some simplifications, the approximate plume equations reduce to:

$$\frac{D\rho}{Dt} + \rho(\nabla \cdot \mathbf{u}) = 0 \tag{3.3.2}$$

$$\rho \frac{D\mathbf{u}}{Dt} = -\nabla p + \rho g \hat{\mathbf{e}}_\mathbf{z} \tag{3.3.3}$$

$$\rho c_p \frac{DT}{Dt} + \frac{Dp}{Dt} = \dot{q}''' \tag{3.3.4}$$

where ρ is the density, $\mathbf{u}$ the velocity of the flow, g the gravitational constant, c_p the specific heat coefficient at constant pressure, T the temperature and $\dot{q}'''$ is the fire heat release rate per unit volume [1]. These three equations are respectively the continuity equation, momentum equation and energy equation. Trelles' dimensional analysis [**107**] showed that the diffusive terms $\Delta\mathbf{u}$ and ΔT in the momentum and thermodynamic equations respectively could be neglected in the case of a fire plume. The pressure decomposition (3.3.1) is substituted in the previous set of equations. Neglecting the small contributions of the pressure work in the energy equation and identifying p_0 as the hydrostatic pressure $\frac{dp_0}{dz} = \rho_0 g$, the equations become:

$$\frac{D\rho}{Dt} = -\rho(\nabla \cdot \mathbf{u}) \tag{3.3.5}$$

$$\rho \frac{D\mathbf{u}}{Dt} = -\nabla \tilde{p} + (\rho - \rho_0) g \hat{\mathbf{e}}_\mathbf{z} \tag{3.3.6}$$

$$\rho c_p \frac{DT}{Dt} = \dot{q}''' \tag{3.3.7}$$

$$p_0 = \rho R T \tag{3.3.8}$$

where the last equation is the equation of state. Since wildfires evolve in a large open domain, p_0 can be assumed to be constant. Therefore, the equation of state

1. The notation for $\dot{q}'''$ is taken from the literature where the dot symbol ($\dot{}$) denotes the time dependence and the triple prime ($'''$) symbol refers to the volume.

becomes

$$\rho T = \rho_0 T_0. \tag{3.3.9}$$

This set of equations can be simplified by combining the continuity equation (3.3.5), the energy equation (3.3.7) and the equation of state (3.3.9) into a single divergence equation. Computing the material derivative on each side of equation (3.3.9) leads to

$$\rho \frac{DT}{Dt} + T \frac{D\rho}{Dt} = 0. \tag{3.3.10}$$

Substituting the material derivatives for T and ρ with Equations (3.3.7) and (3.3.5) respectively to find:

$$\rho \frac{\dot{q}'''}{\rho c_p} - T\rho(\nabla \cdot \mathbf{u}) = 0. \tag{3.3.11}$$

Isolating the divergence term and using again Equation (3.3.9) yields

$$\nabla \cdot \mathbf{u} = \frac{\dot{q}'''}{c_p \rho_0 T_0}. \tag{3.3.12}$$

The equation governing the wind flow given by Equation (3.3.12) is directly related to the fire heat release rate per unit volume $\dot{q}'''$ [W/m^3]. The other parameters are the specific heat coefficient at constant pressure c_p [J kg^{-1}K^{-1}], the ambient density ρ_0 [kg/m^3] and the ambient temperature T_0 [K]. The wind flow is constrained by a simple divergence equation (3.3.12) of the form $\nabla \cdot \mathbf{u} = S$, where S is a source term. This source takes into account the effect of the heat released by the fireline and will affect the wind flow locally. Far away from the fire, the wind velocity field will be divergence free since the source term S is equal to zero.

3.3.2. A projection method

A projection method is used to extract the velocity field $\mathbf{u}$ that satisfies the divergence equation (3.3.12) of the form $\nabla \cdot \mathbf{u} = S$ from a given background wind velocity $\mathbf{v}$. It involves the resolution of an elliptic problem.

The projection method uses the Hodge decomposition which states that any vector field $\mathbf{v}$ defined on a simply connected domain Ω with a smooth boundary $\partial\Omega$ can be decomposed into a solenoidal part $\mathbf{v}_d$ and a curl-free part written as a potential gradient $\nabla\varphi$:

$$\mathbf{v} = \mathbf{v}_d + \nabla\varphi \tag{3.3.13}$$

with $\nabla \cdot \mathbf{v}_d = 0$ on Ω and $\mathbf{v}_d \cdot \mathbf{n} = 0$ on $\partial\Omega$. The following approach was inspired by previous work of Hilditch [**49**], Lay [**55, 56**] and Pember [**78**]. It is in fact an extension of the classical projection method. The decomposition adds a third term accounting

for heat perturbation. Assume that an initial velocity field $\mathbf{v}$ can be decomposed into three parts:

$$\mathbf{v} = \mathbf{v}_d + \nabla\varphi + \nabla\chi \tag{3.3.14}$$

where $\mathbf{v}_d$ is a divergence-free part ($\nabla \cdot \mathbf{v}_d = 0$), φ a potential function and χ another potential function that takes into account the fire heat release. Applying the divergence operator on Equation (3.3.14) leads to

$$\nabla \cdot \mathbf{v} = \Delta\varphi + \Delta\chi. \tag{3.3.15}$$

Substitute $\Delta\chi = S$ in Equation (3.3.15) to get a Poisson equation:

$$\Delta\varphi = \nabla \cdot \mathbf{v} - S. \tag{3.3.16}$$

Once this equation is solved for φ, the final vector field is obtained with the projection:

$$\mathbf{u} = \mathbf{v} - \nabla\varphi. \tag{3.3.17}$$

By the decomposition (3.3.14), one can check that $\mathbf{u}$ can also be written as

$$\mathbf{u} = \mathbf{v}_d + \nabla\chi. \tag{3.3.18}$$

Applying the divergence operator on the previous equation and using the identities $\nabla \cdot \mathbf{v}_d = 0$ and $\Delta\chi = S$ yields to $\nabla \cdot \mathbf{u} = S$.

Solving the Poisson equation (3.3.16) and correcting the initial vector field $\mathbf{v}$ with Equation (3.3.17) yields the required vector field $\mathbf{u}$. The Poisson equation (3.3.16) for the potential φ requires appropriate boundary conditions to be solved. Since the wind flow is assumed to be inviscid, a slip condition $\mathbf{u} \cdot \mathbf{n} = 0$ is applied at the bottom boundary of the computational domain. This forces the wind field to be tangent to the topography. This is translated to a homogeneous Neumann boundary condition for the function φ. As for the side and top boundaries of the domain, the wind is allowed to flow through these open boundaries, hence a homogeneous Dirichlet condition is used. The elliptic problem to be solved can be stated as:

$$\begin{aligned} \Delta\varphi &= \nabla \cdot \mathbf{v} - S, \\ \varphi^B &= 0 \quad \text{on the open boundaries,} \\ \frac{\partial\varphi^B}{\partial n} &= 0 \quad \text{on the topography,} \end{aligned} \tag{3.3.19}$$

where S is a source term coming from the heat released by the fireline.

3.4. THE FIRE FEEDBACK

Current models such as ForeFire and WRF-fire take advantage of the fireline representation as an interface when computing the fire feedback into the atmospheric flow. The coupling between the fire and atmosphere models is typically done in the following steps:

(1) The fireline is evolved for one time step by the wind generated by the atmospheric model.

(2) The area of the burned region during this time step is computed. For instance, the red area between t_0 and t_1 in Figure 3.4.

(3) Some quantities due to combustion such as heat fluxes, temperature and water vapor are computed.

(4) These quantities are injected in the lowest layer of the atmospheric model as source terms in the primitive equations.

(5) The atmospheric model updates the wind flow.

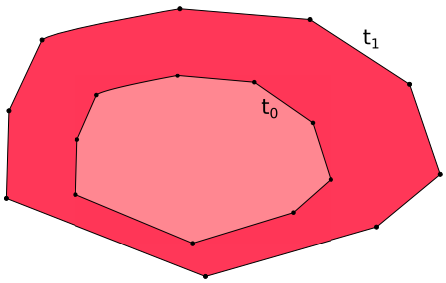

FIGURE 3.4. Burned region (red area) by the interface between time t_0 and t_1.

In our new model, rather than injecting different quantities in the primitive equations, the atmospheric model consists of a single divergence equation of the form $\nabla \cdot \mathbf{u} = S$. This single equation combines the continuity, energy and state equations. The fire feedback is directly integrated in this equation as a source term S. A novel feature of this model is the approach taken to compute the source term S in the divergence equation. The key idea is to make use of the fireline representation. In the fire model, the combustion at the fireline is assumed to be infinitely fast. It means that the fireline is not a region band where the fuel burns over some time. The fireline can therefore be described as an infinitely thin curve.

As seen in Section 3.3, the source term S in the divergence equation (3.3.12) for the velocity field is given by

$$S = \frac{\dot{q}'''}{c_p \rho_0 T_0}. \tag{3.4.1}$$

The fire heat release rate $\dot{q}'''$ is the only variable since c_p, ρ_0 and T_0 remain constant across the domain. The source term must be integrated in the numerical model in such a way that it remains consistent with the representation of the fireline Γ in the fire model. The fireline is represented by an interface that corresponds to the zero level set of a function ϕ. For consistency with this representation, the fire heat release source must be concentrated along this interface. Such a representation of the source can be achieved with a delta function supported on the interface Γ:

$$S = \mathscr{M}(\mathbf{x}, t)\delta(\Gamma)$$

where $\mathscr{M}(\mathbf{x}, t)$ is the amplitude of the delta source that will change along the curve Γ and through time. The relation of this amplitude with the fire heat release rate $\dot{q}'''$ must be defined locally. For that matter, the notion of fire intensity I [kW/m] introduced by Byram [**3, 4**] is useful. The fire intensity is defined as the heat release per unit time per unit length of fire front, regardless of its depth. It can be computed as the product of the fire rate of spread R [m/s], the combustion energy H [kJ/kg] released of the fuel load m [kg/m^2]:

$$I = H\,m\,R. \tag{3.4.2}$$

Hence, a proper definition of the fire heat release rate $\dot{q}'''$ $[W/m^3]$ from a singular source is:

$$\dot{q}''' = I\,\delta(\Gamma) = H\,m\,R\,\delta(\Gamma). \tag{3.4.3}$$

Knowing that the units of the delta $\delta(\Gamma)$ are $1/\mathrm{m}^2$, we can see that this substitution for $\dot{q}'''$ makes sense with the units:

$$\frac{\mathrm{W}}{\mathrm{m}^3} = \frac{\mathrm{W}}{\mathrm{m}} \cdot \frac{1}{\mathrm{m}^2}. \tag{3.4.4}$$

One can interpret this way of defining $\dot{q}'''$ with the delta function as if the heat release is constricted along the fireline in the normal directions to the curve.

Combining equations (3.3.12) and (3.4.3), the divergence equation can now be written as

$$\nabla \cdot \mathbf{u} = \frac{HmR(\mathbf{x}, t)}{c_p \rho_0 T_0}\delta(\Gamma). \tag{3.4.5}$$

The amplitude of the delta function $\delta(\Gamma)$ will vary in time and along the fireline Γ according to the normal rate of spread $R(\mathbf{x}, t)$. The fireline rate of spread is computed with equation (3.2.7) which depends on the ellipse parameters a, b and c.

3.5. THE WIND FEEDBACK

The wind model is governed by equation (3.3.12) only, a divergence constraint with a source term accounting for the heat release rate by the fireline. The divergence equation was derived from a set of equations coming from the low Mach number approximation used in plume theory. The main features of a fire plume are the updraft and the entrainment of air at the baseline of the buoyant plume. A parcel of fluid above the fireline will be heated up by the fire which will make the parcel move upward, hence the updraft. The space "emptied" by the warmed parcel is then replaced by cooler air surrounding the fire which leads to a sucking effect at the baseline of the fire. This effect was studied by Dold *et al.* [**37**] in the case of a fireline with a fixed elliptical shape. These characteristics of the local flow near the fireline are sketched in Figure 3.5.

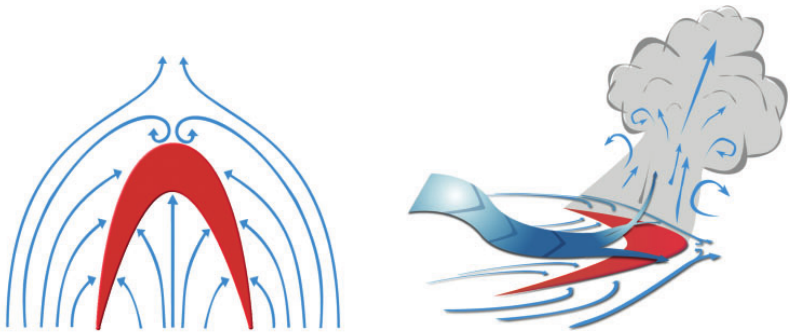

FIGURE 3.5. Conceptual model of the airflow around the fire plume. Source: Werth *et al.* [**114**].

Another important feature of a fire plume is the circulation pattern as shown in Figure 3.6. This phenomenon can be reproduced by the pressure gradient and the

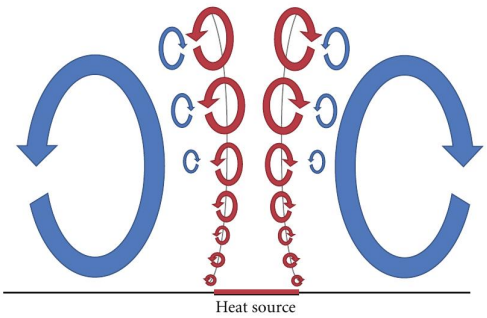

FIGURE 3.6. Sketch of the fire induced wind (Source: Forthofer [**48**]).

buoyancy force of the momentum equation (3.3.6), but this particular equation does not intervene in the atmospheric model. There is an efficient way to recover these features of the flow using the divergence equation only.

Trelles [**107**] converted the momentum equation into a rotational constraint with a vorticity source:

$$\nabla \times \mathbf{u} = \boldsymbol{\omega}_p \tag{3.5.1}$$

where $\boldsymbol{\omega}_p$ denotes the vorticity in the plume. Using this constraint in our model would require the computation of the rotational part of the wind vector field. It would then lead to the resolution of a vectorial Poisson equation. For efficiency reasons, another approach was taken. From the results of the simulations in Trelles' thesis, it appeared that the global features of the flow could be generated with a sink-source pair in the divergence equation. The sink is located at the base of the fireline while the source is positioned at some vertical distance d_δ above the fireline. The sink and source are given as delta functions of the same amplitude but opposite sign. The delta function accounting for the sink will be supported on the interface Γ and the source will be supported on a vertical translation Γ_T of the fireline interface. The divergence equation (3.4.5) with the delta source decouples in a sink-source pair as follows

$$\nabla \cdot \mathbf{u} = \frac{HmR(\mathbf{x}, t)}{c_p \rho_0 T_0} \left(\delta(\Gamma_T) - \delta(\Gamma)\right). \tag{3.5.2}$$

Note that the amplitude remains the same as in Equation (3.4.5), only the form of the source has changed to a sink-source pair.

Figure 3.7 shows the flow generated by equation (3.5.2) for the two-dimensional case in which the fireline is a single point. The flow is induced by a point sink-source pair in the picture on the left. Combining the results with a background wind $\mathbf{v}_d$ lead to the picture on the right. The induced flow is presented without and with an initial background wind. The circling motion in the picture on the left reproduces the situation in the sketch of Figure 3.6. Above the fireline, the wind is moving downwards which represents a downdraft in contrast to the updraft occurring in plume fire. This part does not affect the model since the wind has only a non-zero vertical component and thus does not contribute to the fire rate of spread.

A 3D version of the wind flow induced by a sink-source pair is shown in Figure 3.8. In this case, the fireline is represented by a circle of diameter 50. The top pictures showing slices in the xz planes can be seen as a generalization of the flow of Figure 3.7. In the top-right picture, it is possible to see the rear downdraft as in the conceptual model of Figure 3.5. Another important feature of this model captured with the sink-source pair is the convergence of streamlines downwind in the bottom-right picture. Such convergence in the head fire has been observed in numerical simulations with WRF-fire in Peace's thesis [**77**]. Recall that not only the magnitude of the wind flow has an incidence on the fire spread, but the wind direction too.

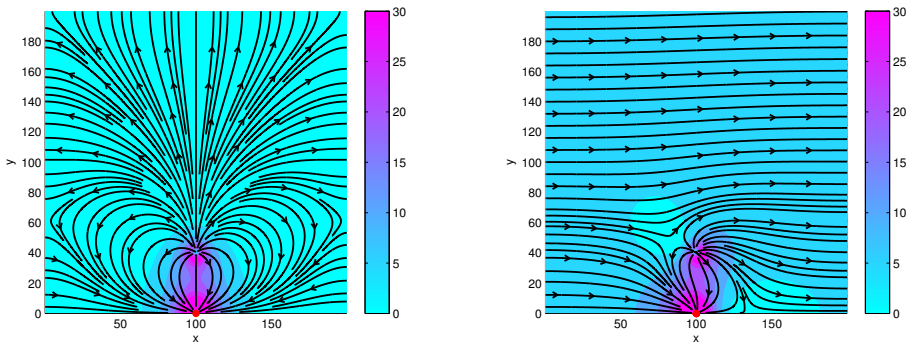

FIGURE 3.7. Streamlines and magnitude of a 2D wind velocity field induced by a point sink-source pair at the fireline (red dot) with no background wind (**left**) and with a horizontal background wind (**right**).

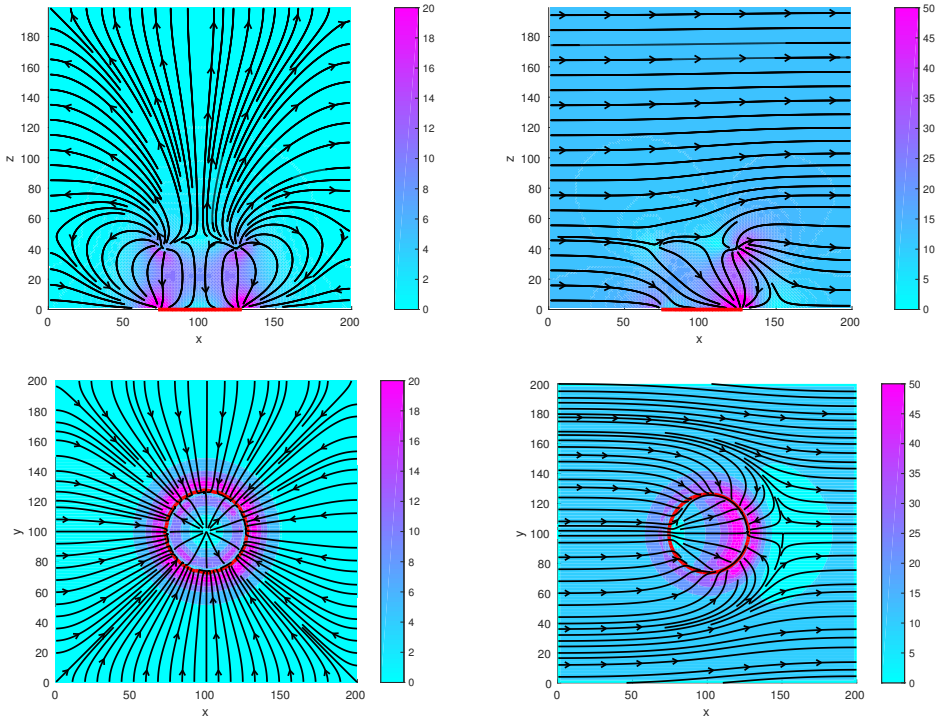

FIGURE 3.8. Slices of the streamlines and magnitude of a 3D wind velocity field induced by a curve sink-source pair at the fireline (50 diameter red circle) with no background wind (**left**) and with a horizontal background wind (**right**) in the $y = 100$ plane (**top**) and the $z = 2$ plane (**bottom**).

Figures 3.7 and 3.8 show two possible case scenarios for the local wind flow near the fireline. If the magnitude of the wind induced by the fireline is sufficiently stronger than the background wind, then the generated pattern of the wind flow should

have plume-like features. In the opposite case, the background wind will have the strongest contribution to the flow. This idea relates to the attached (wind dominated) flow and separated (plume dominated) flow also studied by Dold in a series of papers [**32**, **33**, **34**, **35**, **36**, **38**].

After these considerations of the features of the flow, the contribution of the wind flow on the fire rate of spread remains to be determined. It remains an open question and an important challenge encountered by coupled fire-atmosphere models. Coen *et al.* [**24**] pointed out that "*the mechanisms through which wind affects a fire's rate of spread and therefore how it should be incorporated in models remain an active area of research*". Finney *et al.* [**45**] recalled that to this date, there is still "*no verifiable physical theory of spread available*". There is no consensus in the modeling community on which part of the wind velocity field and to which extent this one affects the fire spread. Most models are well aware that, due to the updraft structure, the wind velocity field above the fireline has a zero horizontal component. They use a wind vector chosen at an arbitrary distance behind the fire spread direction and at some height above ground. Sometimes this wind vector is even interpolated to the *mid-flame* position before computing the fire rate of spread.

Many models such as WRF-fire compute the wind contribution onto the fire rate of spread with formulas based on empirical data. A popular formula is Rothermel's [**88**] which computes the normal rate of spread R with the following linear relation:

$$R = R_0(1 + \phi_W + \phi_S) \tag{3.5.3}$$

where R_0 is the velocity without wind but that accounts for fuel and humidity, ϕ_W is a wind velocity factor and ϕ_S is a slope factor.

The fire model in Section 3.2 is based on Richards' ellipse model [**87**] which originally used complex empirical spread relationships. The computation of the ellipse parameters a, b et c involved in the fire rate of spread is detailed in the literature of the model Prometheus [**112**]. The Forestry Canada Fire Danger Group (FCFDG) [**46**] has categorized the main types of fuel of the boreal forest of Canada into 16 types. For each type of fuel, empirical relationships have been elaborated in order to describe the fire behavior. These formulas have been established using correlations obtained with more than 400 experimental wildfire observations. A vectorial technique is used in order to take into account the effect of the wind and terrain slope. The slope is converted to a fictional wind which is added to the local wind speed in order to get an effective wind. Figure 3.9 shows the parameters a, b and c as functions of the wind magnitude for a Ponderosa pine fuel bed. As the net effective wind speed (WSV) reaches 14 m/s, the coefficients for the rate of spread become constant. These formulas are rather complicated and can make difficult the analysis

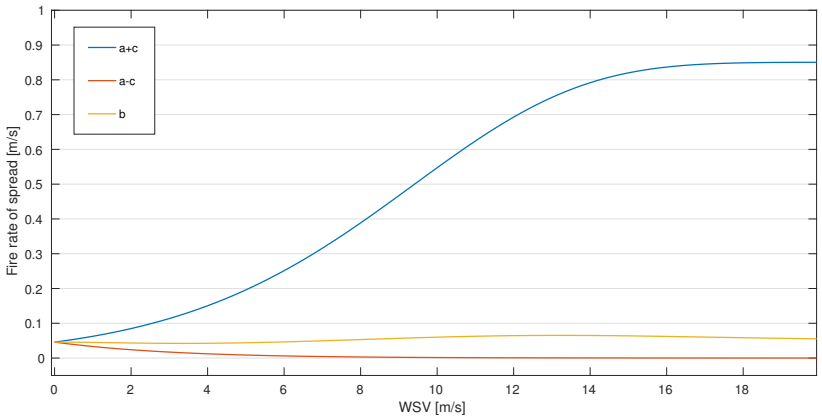

FIGURE 3.9. Values of the rate of spread $a+c$, back rate of spread $a-c$ and flank rate of spread b as functions of the net effective wind speed (WSV) for a Ponderosa pine fuel bed from the FCFDG empirical model.

of the fire regimes. A simpler cubic model derived from plume dynamics [**34, 38**] is used in our coupled model.

Using the conservation of mass, energy and momentum and some simplifications for plume dynamics, Dold [**34**] derived the following relation between the vertical component of the wind flow in the plume, v, and the intensity of the fire, I:

$$v^3 \approx \frac{gI}{2\alpha c_p \rho_e T_e} \tag{3.5.4}$$

where α is an entrainment constant, g the acceleration due to gravity, c_p the specific heat of the fireline and T_e and ρ_e the temperature and the density of the fresh environmental air respectively. Assuming that the entrainment velocity $v_e = \alpha v$ must be supplied by the incoming wind w relative to the fire rate of spread R, one can assume that $v_e \approx w - R$ and hence

$$(w-R)^3 \approx \frac{\alpha^2 gI}{2c_p \rho_e T_e}. \tag{3.5.5}$$

Dold used this relation to derive a qualitative description of plume-driven and wind-driven regimes of propagation. When the fire is driven by a steady wind w, a transition between the attached flow (at low intensity) and a separated buoyant plume flow (at high intensity) arises around a critical intensity $I_c(w)$. These different forms of airflow lead to different spread rates R. At low intensities (below I_c), the spread rate should increase. Dold claimed that an equilibrium spread rate is possible if the spread rate intensity relationship intersects Byram's formula.

In this model, the local wind flow is computed using the intensity in a divergence equation. Hence, a linear change of I leads to a linear change of $\mathbf{u}$ which does not

reproduce the cubic relationship observed in plume fires. Albini [1] suggested the interesting formula

$$\frac{R}{R_0} = 1 + \frac{(U-R)^3}{R_A^3}\frac{I}{I_0} \tag{3.5.6}$$

for relating spread rate to unsteady intensity over horizontal terrain in a supporting wind of speed U, having $U \geq R_0$. In this formula R_0 is the basic steady spread rate in light wind (specifically, when $U = R_0$ in the formula) ; I_0 is the corresponding steady basic fireline intensity, namely $I_0 = QmR_0$; and R_A is a vegetation-dependent spread rate factor that would typically be much greater than R_0. Dold [38] shows that the dependence of R on I in Albini's formula can be expressed as:

$$\frac{R}{R_s} = \left(\frac{I}{I_s}\right)^{\nu} \tag{3.5.7}$$

where R_s and I_s are the steady-state fire rate of spread and intensity respectively. This formula is valid for $\nu < 1$. Since, the fire induced wind $u(\mathbf{x}, t)$ is linearly dependent on the fire intensity I, this power law can therefore be used to express the relationship between the local wind u and the fire rate of spread $R(\mathbf{x}, t)$. For this model, the fire rate of spread is computed as:

$$R(\mathbf{x}, t) = R_0(\mathbf{x}) + (u(\mathbf{x}, t))^{\frac{1}{3}} \tag{3.5.8}$$

where R_0 is a vegetation and slope dependent spread rate in the absence of wind and the contribution of the local wind flow u on the rate of spread follows an inverse cubic law. Viegas [113] used a similar formula in which the spread rate R is a power-law function of the local wind U:

$$\frac{R}{R_0} = 1 + \left(\frac{U}{U_0}\right)^{\mu} \tag{3.5.9}$$

for some power μ. Rothermel [88] also used a power law function in the same fashion.

In order to use this equation with the ellipse model of the fire model, a, b and c parameters must be defined. The rate of spread is given by $R = a + c$, the back rate of spread is $a - c$ and flank rate of spread b. Assuming R_0 is sufficiently bigger than zero, the parameters are defined as follows:

$$a = R_0 + \frac{9}{20}\sqrt[3]{u(x,t)}, \tag{3.5.10}$$

$$b = R_0 + \frac{1}{5}\sqrt[3]{u(x,t)}, \tag{3.5.11}$$

$$c = \frac{11}{20}\sqrt[3]{u(x,t)}. \tag{3.5.12}$$

The spread values are shown in Figure 3.10 with $R_0 = 1$. The calibration of the parameters was done in such a way that the three curves in this figure would reproduce the qualitative behavior of Figure 3.9.

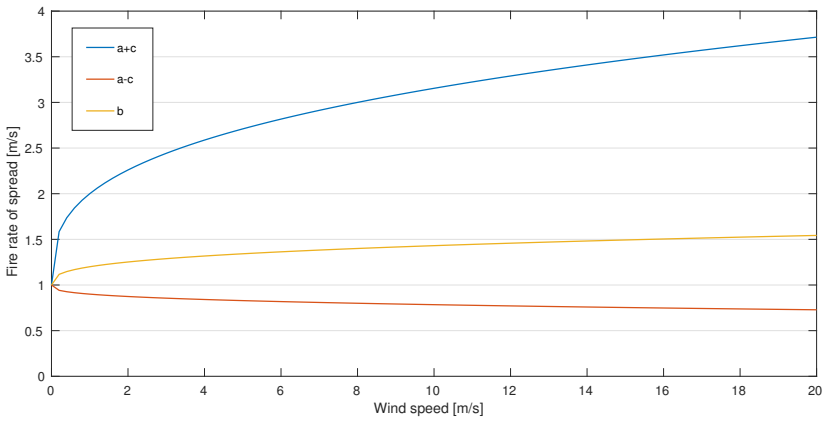

FIGURE 3.10. Values of the rate of spread $a + c$, back rate of spread $a - c$ and flank rate of spread b as a function of the wind speed with the cubic model when $R_0 = 1$.

Adding a and c leads to the chosen equation (3.5.8) for the rate of spread. The slope has an impact on the rate of spread even in the absence of wind and this effect is taken by R_0.

3.6. DIMENSIONAL ANALYSIS

A dimensional analysis is necessary in order to determine the appropriate scales for the model as well as non-dimensional numbers that will be used to characterize the flow and the regimes of fire propagation. Recall the divergence equation:

$$\nabla \cdot \mathbf{u} = \frac{Hm}{c_p \rho_0 T_0} R\delta(\Gamma). \tag{3.6.1}$$

Define the following dimensionless variables ;

$$\delta^*(\Gamma) = \delta(\Gamma) d_c^2 \qquad \nabla^* = \nabla L_c$$
$$R^* = R/R_c \qquad \mathbf{u}^* = \mathbf{u}/U_c$$

where d_c is the characteristic length related to the diameter of the fireline, L_c the characteristic length of the topography, R_c the characteristic rate of spread of the fireline and U_c the characteristic velocity amplitude of the wind. Substituting these variables in Equation (3.6.1) leads to:

$$\nabla^* \cdot \mathbf{u}^* = \frac{Hm}{c_p \rho_0 T_0} \frac{R_c L_c}{U_c d_c^2} R^* \delta^*(\Gamma) \tag{3.6.2}$$

$$= QR^*\delta^*(\Gamma) \tag{3.6.3}$$

where $Q = \dfrac{Hm}{c_p\rho_0 T_0}\dfrac{R_c L_c}{U_c d_c^2}$ is a dimensionless number describing the quantity of heat released by the fireline relative to the wind amplitude U_c. Characteristic scales for field variables based on typical wildfires are:

$$\begin{aligned}
&U_c \sim 10 \quad [\mathrm{m/s}], && L_c \sim 10^2 \quad [\mathrm{m}], && H \sim 10^7 \quad [\mathrm{J/kg}],\\
&R_c \sim 1 \quad [\mathrm{m/s}], && d_c \sim 10 \quad [\mathrm{m}], && m \sim 1 \quad [\mathrm{kg/m^2}],\\
&c_p \sim 10^3 \quad [\mathrm{J/(kg\,K)}], && T_0 \sim 10^2 \quad [\mathrm{K}], && \rho_0 \sim 1 \quad [\mathrm{kg/m^3}].
\end{aligned}$$

Using these values, the dimensionless number Q will have a value of order $Q \sim 10^3$. The elliptic problem (3.3.19) is defined with the source term

$$S = \frac{Hm}{c_p\rho_0 T_0} R\delta(\Gamma). \tag{3.6.4}$$

Using the same dimensionless variables as before with

$$\varphi^* = \frac{\varphi}{L_c U_c} \qquad \frac{\partial^*}{\partial^* n} = \frac{\partial}{\partial n} L_c \qquad \Delta^* = \Delta L_c^2$$

the elliptic problem becomes:

$$\begin{aligned}
\Delta^*\varphi^* &= \nabla^*\cdot\mathbf{v}^* - QR^*\delta^*(\Gamma)\\
\varphi^{*B} &= 0 \quad \text{on the open boundaries,}\\
\frac{\partial^*\varphi^{*B}}{\partial^* n} &= 0 \quad \text{on the topography.}
\end{aligned} \tag{3.6.5}$$

Clark *et al.* [**18**] used the convective Froude number F_c to measure the level of coupling between the atmosphere and fire. The Froude number is defined as

$$F_c^2 = \frac{(u-R)^2}{g\frac{\Delta\theta}{\theta_a} D_f} \tag{3.6.6}$$

where u and R are the ambient wind speed and the spread rate of the fire, g the acceleration due to gravity, $\frac{\Delta\theta}{\theta_a}$ the convective buoyancy (ratio of the difference between the ambiant potential temperature θ_a and the potential temperature in the convection column θ_c) and D_f the flame depth, the depth of the flaming zone of the fire front. In the simulations, Clark *et al.* used a value of 50 m for D_f. Sullivan [**95**] found this Froude number F_c to be related to Byram's convective number N_c:

$$N_c = \frac{2gI}{\rho c_p \theta_a (u-R)^3} \tag{3.6.7}$$

where I is the fireline intensity, ρ is air density and c_p the specific heat of dry air at constant pressure. The number N_c is inversely proportional to the Froude number: $F_c \propto \frac{1}{N_c^{1/3}}$. The ratio of the two sides of Equation (3.5.5) corresponds up to a constant

$4/\alpha^2$ to the number N_c above. In fact, both physical parameters represent the ratio between two forces: the inertia of the wind and the buoyancy due to the thermal plume. These forces have an impact on the trajectory of the flame and thus influence the way the heat is transferred from the flame to the fuel bed.

There is a relation between the dimensionless number Q and these two parameters. Since the atmospheric model only indirectly takes into account the momentum Equation, the contribution of the buoyancy is not directly linked. The amplitude of the source term was defined with Byram's definition of the fire intensity ($I = HmR$), which appears in the definition of the dimensionless number Q:

$$Q = \frac{HmR_c}{c_p \rho_0 T_0} \cdot \frac{L_c}{U_c d_c^2}. \tag{3.6.8}$$

The parameter Q can be interpreted as the ratio between the fire induced wind field magnitude, which is generated by the sink-source pair, and a characteristic background wind velocity U_c. A large value of Q means that the fire induced wind flow will have a stronger impact on the fire rate of spread (strong coupling), while a low value means a weak fire induced flow (weak coupling).

3.7. Steady-state rate of spread regimes in 2D

In Section 3.5, it was shown that the fire rate of spread R is the sum of two speeds: a constant rate of spread R_0 without wind, which accounts for the slope, fuel and humidity, and the cubic root of the local wind velocity u which is a linear combination of a background wind and a fire induced wind given by Equation (3.3.18). The rate of spread $R(\mathbf{x}, t)$ is computed with Equation (3.5.8).

Assuming a constant rate R_0, this section first presents the study of the specific contribution of the fire induced wind and the topography slope in the absence of a background wind. This means that the wind flow only accounts for the fire heat release and that $\mathbf{u} = \nabla\chi$ according to Equation (3.3.18). Then, the effect on the rate of spread of adding the background wind $\mathbf{v}_d$ to the fire induced wind $\mathbf{u} = \nabla\chi$ is discussed.

3.7.1. Fire induced wind contribution

The contribution of the fire induced wind velocity field on the fire rate of spread is first considered in the absence of a background wind. The model governing the atmospheric flow is quasi-stationary since the divergence equation does not depend explicitly on time. A stationary solution of the elliptic problem (3.6.5) must be obtained at each time step.

The wind velocity field must satisfy the linear divergence equation:

$$\nabla \cdot \mathbf{u} = QR\delta(\Gamma), \tag{3.7.1}$$

where Q is a non-dimensional number that accounts for the amplitude of the fire intensity and $\delta(\Gamma)$ is the sink-source pair centered on the fireline Γ. In the absence of background wind ($\mathbf{v} = 0$), the wind velocity field is effectively computed by solving the Poisson equation:

$$\Delta\chi = QR\delta(\Gamma) \tag{3.7.2}$$

where $\mathbf{u} = \nabla\chi$ and R depends on the wind velocity $\mathbf{u}$. The fire rate of spread R has not reached its steady-state *a priori*.

Given R_0, the fire rate of spread in the absence of wind, one computes $\hat{\mathbf{u}} = \mathbf{u}/R_0$ by solving this equation:

$$\nabla \cdot \hat{\mathbf{u}} = Q\delta(\Gamma). \tag{3.7.3}$$

The fire rate of spread is computed with this wind contribution taken at a given distance from the fireline with Equation (3.5.8):

$$R_1 = R_0 + f(\hat{u}) = R_0 + \sqrt[3]{\hat{u}}. \tag{3.7.4}$$

If the model recomputes the generated wind field with the rate of spread R at the same position of the fireline Γ, a new wind field different in scales from $\hat{\mathbf{u}}$ will be computed. Hence, this process must be repeated multiple times until the rate of spread R_n approaches a steady-state R^* associated to a steady-state wind field $\mathbf{u}^*$. Since the divergence Equation (3.7.1) is linear, the ratio of the induced wind velocity at a given point of the wind velocity field $\hat{\mathbf{u}}$ and the n^{th} iteration is:

$$\frac{u_n}{\hat{u}} = \frac{QR_{n-1}}{Q} = R_{n-1} = R_0 + f(u_{n-1}) \tag{3.7.5}$$

thus, the steady-state wind velocity u^* can be computed from

$$\frac{u^*}{\hat{u}} = R_0 + f(u^*) \tag{3.7.6}$$

with a fixed point method. Note that the last equation does not involve the parameter Q explicitly. Since the number Q is constant throughout this iterative process, it has only an impact on the induced wind field $\hat{\mathbf{u}}$ computed with Equation (3.7.3). Because of the linearity of the elliptic operator of Equation (3.7.2), the subsequent iterations are proportional and the effect of Q is restricted to the first iteration.

An equivalent way to work that problem is to consider that the steady-state wind field $\mathbf{u}^*$ depends on R_0 and Q. Rather than computing $\mathbf{u}^*$, R^* is computed directly

with the relation:

$$R^* = \mathscr{F}(R^*) \tag{3.7.7}$$

$$R^* = R_0 + f(u^*) \tag{3.7.8}$$

$$R^* = R_0 + \sqrt[3]{QR^*} \tag{3.7.9}$$

since $u^* = QR^*$. Rescaling this last equation by R_0, the equation becomes:

$$R^* = 1 + \sqrt[3]{QR^*} \tag{3.7.10}$$

and depends only on the parameter Q. The steady-state R^* for the previous equation can be found easily with a symbolic solver. The set of solutions are divided into three cases:

$$\text{1 positive and 2 negative real solutions if } Q > \frac{27}{4}, \tag{3.7.11}$$

$$\text{1 positive real solution and two complex conjugate solutions if } Q < \frac{27}{4}, \tag{3.7.12}$$

$$R^* = -\frac{1}{2} \text{ and } R^* = 4 \text{ if } Q = \frac{27}{4}. \tag{3.7.13}$$

Only the positive solution has a physical meaning here. Note that the contribution of the fire induced wind is controlled by the parameter Q on the rate of spread R^*. This contribution can be found by subtracting the fire velocity R_0:

$$(R^* - R_0) = \frac{2\,3^{1/3} Q + 2^{1/3}\left(9Q + \sqrt{3}\sqrt{(27-4Q)Q^2}\right)^{2/3}}{6^{2/3}\left(9Q + \sqrt{3}\sqrt{(27-4Q)Q^2}\right)^{1/3}}. \tag{3.7.14}$$

Figure 3.11 shows the graph, on a log-log scale, of the fire induced wind contribution $(R^* - R_0)$ on the rate of spread R^* as a function of the parameter Q. This figure illustrates two asymptotic behaviors of Equation (3.7.14). When $Q \to \infty$, the ratio $\frac{(R^*-R_0)}{Q^{1/2}} \to 1$ and when $Q \to 0$, the ratio $\frac{(R^*-R_0)}{Q^{1/3}} \to 1$.

Figure 3.12 shows the contribution $(R^* - R_0)$ as a function of Q on a linear scale. The curve is drawn with two colors: the full red line represents the region where $(R^* - R0) \sim Q^{1/3}$ and the blue dashed line denotes the region where $(R^* - R0) \sim Q^{1/2}$.

In order to check the stability of the positive real value of the steady state R^*, the derivative of the function $\mathscr{F}(R)$ is computed and shown as a function of Q in Figure 3.13. The fixed point R^* satisfies the stability condition since $|\mathscr{F}'(R^*)| < 1$. Following this condition, Figure 3.13 shows that the positive fixed point value R^* is stable for all values of $Q > 0$.

Remark also that the cubic relation (3.5.8) guarantees that a steady-state rate of spread R^* exists. For instance, a linear relation for the rate of spread and the wind

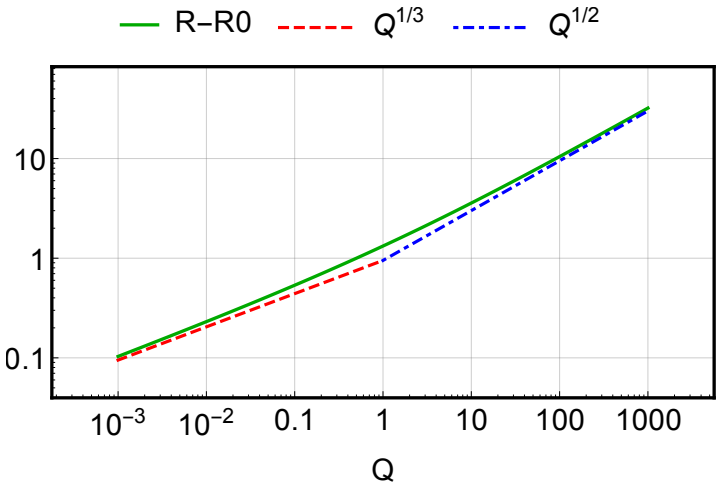

FIGURE 3.11. Log-log plot of the contribution of the induced wind $(R^* - R0)$ as a function of Q. There are two asymptotic behaviors of this contribution: $(R^* - R0) \sim Q^{1/2}$ as $Q \to \infty$ and $(R^* - R0) \sim Q^{1/3}$ as $Q \to 0$.

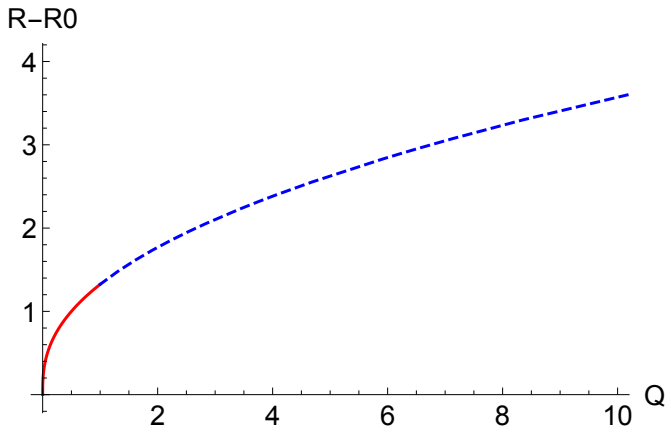

FIGURE 3.12. Plot of the contribution of the induced wind $(R^* - R0)$ as a function of the non-dimensional fire intensity parameter Q. The red part of the curve depicts $(R^* - R0) \sim Q^{1/3}$ and the blue dashed part when $(R^* - R0) \sim Q^{1/2}$.

velocity would not necessarily lead to a steady state for R^* which could increase indefinitely.

3.7.2. Slope contribution

In the previous subsection, the stable rate of spread R^* was computed from the parameters R_0 and Q when there is no contribution from a background wind and no topography slope. The latter is expected to have a major effect on the fire rate of spread. The inclination brings the flames near the ground which accelerates the

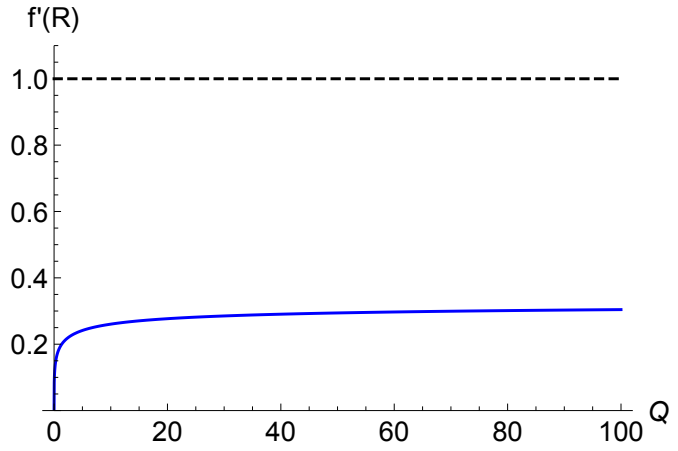

FIGURE 3.13. Plot of the derivative of the steady-state rate of spread function $\mathscr{F}(R^*)$ as a function of the non-dimensional parameter Q.

pre-heating of the fuel in the upslope direction, leading to a faster spread velocity when the fire is moving upslope than downslope.

This subsection aims to quantify the effect of the topography slope, noted α, on the fire induced wind $\mathbf{u}$. The same approach is used for computing the steady-state rate of spread R, but Equation (3.7.6) is more appropriate since $\hat{\mathbf{u}}$ can be computed numerically. Since $\hat{\mathbf{u}}$ is known, the formula for R^* could also be used since $Q = \hat{u}/R_0$.

In order to qualify the effect of the topography slope on the rate of spread R, the wind field $\hat{\mathbf{u}} = \mathbf{u}/R_0$, computed using an initial rate of spread $R = R_0 = 1$ with this equation:

$$\nabla \cdot \hat{\mathbf{u}} = Q\delta(\Gamma), \tag{3.7.15}$$

will be different for each slope angles α. The topography slopes $H_\alpha(x)$ are defined as:

$$H_\alpha(x) = \tan(\alpha)x + 1 \tag{3.7.16}$$

where $-45^\circ \leq \alpha \leq 45^\circ$ is the angle of the slope between the topography (a straight line) and the $x-$axis.

The wind fields $\hat{\mathbf{u}}$ are computed with the numerical model on a $[0,320] \times [0,640]$ computational domain with a mesh size of $h = 1/2$. The separation between the sink and source is fixed to 40 and the delta support is $2\varepsilon = 4$. The wind field component that will contribute to the rate of spread R given by Equation (3.7.4) is chosen at a fixed distance $D = 5$ m tangent to the topography behind the fireline and 1 m above the topography.

Figure 3.14 shows the wind $\hat{\mathbf{u}}$ for the slope angles $\alpha = 0, 25, 45^\circ$. When the topography is completely horizontal ($\alpha = 0^\circ$), the wind flow induced by the sink-source

pair is perfectly symmetric with respect to the fireline (point at $x = 160$). However, as the slope angle α increases, this symmetry is lost. Note that the wind magnitude is non-zero in the region close to the fireline. This is expected since the wind is induced by a singular sink-source pair. For this reason, the wind contributing to the fire rate of spread must be taken at a short distance D behind the fireline.

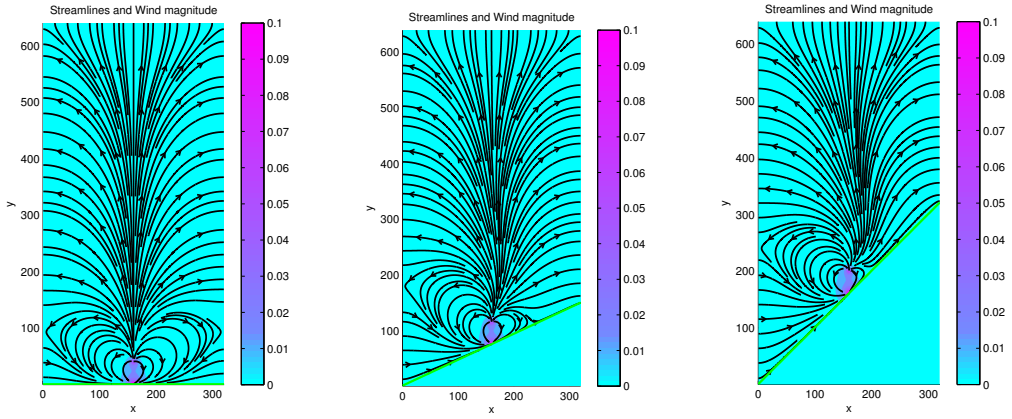

FIGURE 3.14. Streamlines (black arrowed-lines) and wind magnitude of a fire induced wind with $Q = 1$ on slope angles $\alpha = 0, 25, 45°$.

The vector field $\hat{\mathbf{u}}$ is computed numerically, but only the wind magnitude at a fixed distance D from the fireline is required to compute the steady-state rate of spread R. Since the generated wind field $\hat{\mathbf{u}} = (\hat{u}, \hat{v})$ is tangent to the topography, the wind magnitude can be computed by taking the horizontal component $\hat{u}$ and dividing it by $\cos(\alpha)$.

Figure 3.15 adds two new curves to the previous Figure 3.11. These two curves show the fire induced wind contribution $(R^* - R_0)$ as a function of Q for topographies with the slope angles $\alpha = -45°$ and $\alpha = 45°$. All other curves for the different slope angles between $-45°$ and $45°$ fall in the range outlined by these two curves. It is interesting to check if the slope angle has an impact on the asymptotic behavior of the fire induced wind. It is clear that the slope has little impact on the two asymptotic behaviors computed for the analytic relation (3.7.14).

As $Q \to 0$, the fire induced wind contribution $(R^* - R0) \sim Q^{1/3}$. There is a small difference when $Q \to \infty$, $(R^* - R0) \sim Q^{9/20}$ rather than $Q^{1/2}$. The two asymptotic behaviors are essentially the same as for the analytic result. The small discrepancy when $Q \to \infty$ is explained by the numerical computation of $\hat{\mathbf{u}}$. For each slope angle α and parameter value Q, a numerical solution of the fire induced wind velocity field $\hat{\mathbf{u}}$ is required for the computation of the fire rate of spread R^*. In the previous subsection, R^* was computed analytically from Equation (3.7.10) without the need of a numerical wind field $\hat{\mathbf{u}}$.

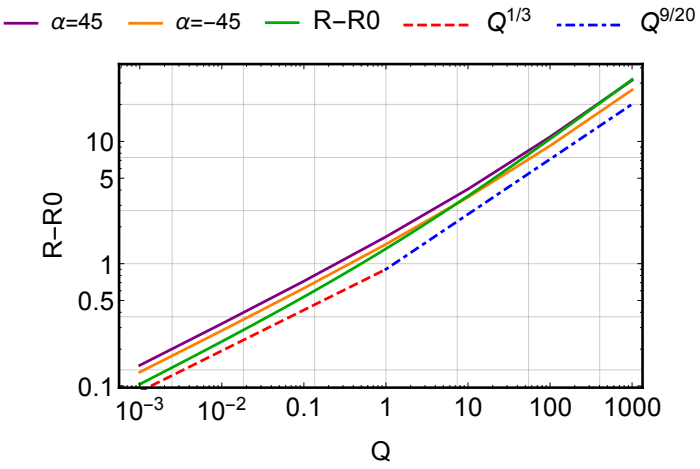

FIGURE 3.15. Log-log plot of the contribution of the induced wind $(R^* - R0)$ as a function of the fire intensity Q for the slope angles $\alpha = -45°$ and $\alpha = 45°$.

Figure 3.16 presents the steady-state fire rate of spread R^* as a function of the slope angle α for different magnitudes of Q. An increase in Q induces a proportional

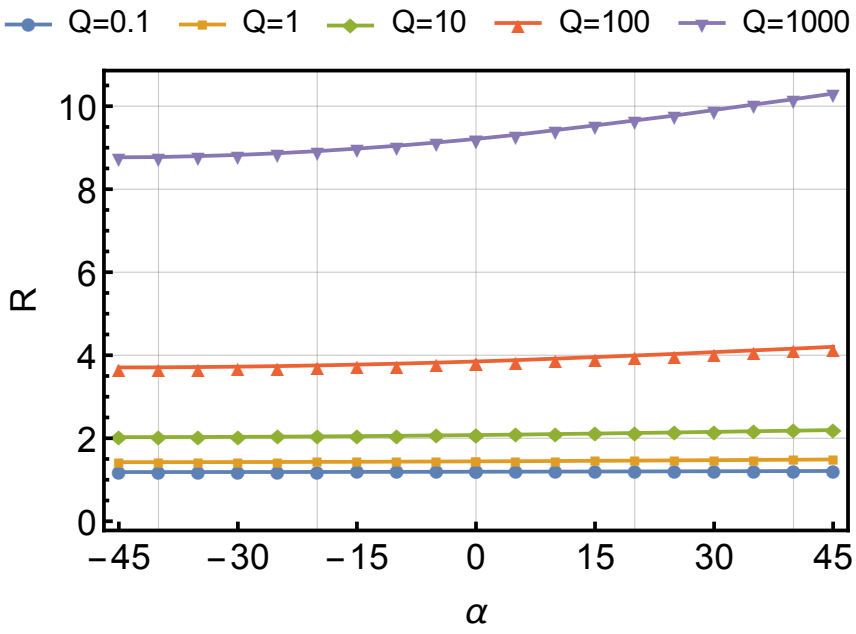

FIGURE 3.16. Stable rate of spread of the fire R^* as a function of the slope angles $\alpha \in [-45°, 45°]$ (5° increments) for the fire intensity parameter $Q = 10^k$ with $k = -1, 0, 1, 2, 3$.

increase in the induced wind field $\hat{\mathbf{u}}$. This is expected since the elliptic equation is linear. On the other hand, this linearity is lost when the stable rate of spread R is computed since the dependence of $\hat{\mathbf{u}}$ on R takes the form of a cubic root.

The rate at which R^* increases with α is not the same for the different values of Q. Figure 3.17 shows the same results as in Figure 3.16 but each Q curve was rescaled by the value of R^* at $\alpha = 0$. It is clear now that for a fixed value of the parameter Q, the rate of spread R increases as the slope increases and decreases as the slope decreases. This means that the structure of the wind field induced by the sink-source pair already accounts for the effect of the slope on the rate of spread. The relationship between the slope angle α and the rate of spread R^* is quadratic. A study of the rate of spread versus slope trends was conducted for FIRETEC by Pimont *et al.* [**79**]. They found that under weak background wind conditions, the rate of spread could increase exponentially with slope and that under strong background wind conditions, the effect of the slope would be mostly linear. They compared their results with other models for computing the rate of spread (such as BEHAVE, MacArthur and FCFDG) and found that rate of spread *"[...] versus slope trends for the operational models are all similar to FIRETEC in that they all increase monotonically with slope"*. Another conclusion was that the relationships between wind, slope and fire width are not linear.

As explained by Dold [**34**], the rate of spread in a plume-driven flow is higher than in a wind-dominated flow. If the fire intensity Q increases, the magnitude of the wind generated by the fire will increase and lead to a plume-driven flow. There is little empirical or experimental data in the literature to analyze the effect of the plume driven flow on the rate of spread when the fire is moving upslope or downslope. Figure 3.17 shows, at least for our particular model, the general behavior of the rate of spread R as a function of the slope α. As one could expect, the rate of spread of the fire is higher when the fire is moving upslope.

Finally, the impact of the slope is even accentuated when the magnitude of Q is increased. If it was not the case, the curves in Figure 3.17 would coincide with each other after the rescaling but this is not the case. Clearly, the effect of the slope on the rate of spread is even more important when Q is bigger, but the trend seems to remain quadratic.

3.7.3. Background wind contribution

The effect of fire induced wind and the slope angle α as a contribution to the fireline rate of spread has now been established. The same question surfaces for the background wind $\mathbf{v}_d$, the wind that is not induced by the fire. The background wind $\mathbf{v}_d$ is constant with respect to time. From the projection, it can be added to the fire induced wind with Equation (3.3.18):

$$\mathbf{v}_d + \nabla\chi = \mathbf{u} \tag{3.7.17}$$

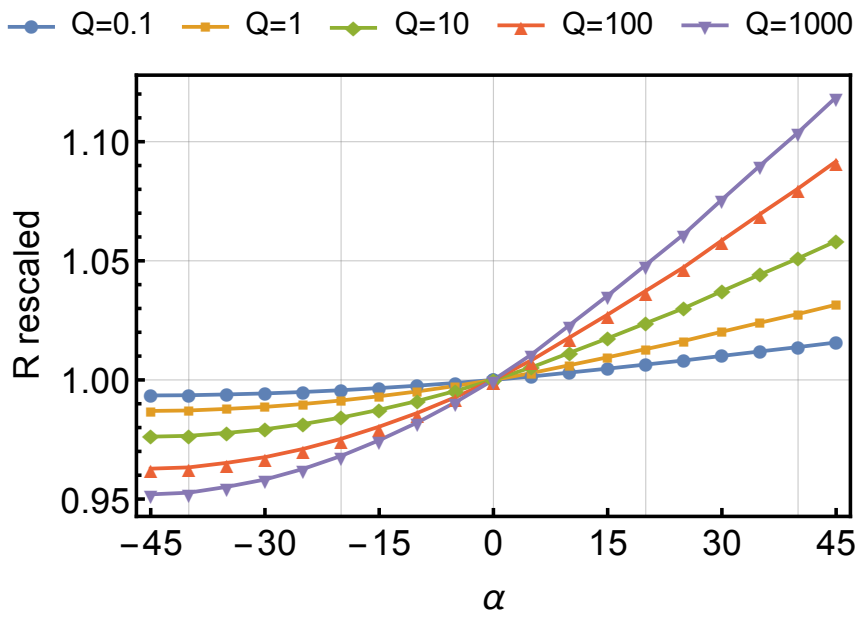

FIGURE 3.17. Stable rate of spread of the fire R^* rescaled by the value of R^* at the slope $\alpha = 0$ as a function of the slope angles $\alpha \in [-45°, 45°]$ (5° increments) for the fire intensity parameter $Q = 10^k$ with $k = -1, 0, 1, 2, 3$.

Applying the divergence operator on this equation will lead to:

$$\nabla \cdot \nabla \chi = \nabla \cdot \mathbf{u} \tag{3.7.18}$$

$$\Delta \chi = QR\delta(\Gamma) \tag{3.7.19}$$

the Poisson problem to be solved with the homogeneous boundary condition on χ. This is the same elliptic problem solved in the case of the absence of a background wind. The difference appears in the computation of the rate of spread:

$$R(\mathbf{x}, t) = R_0(\mathbf{x}) + \sqrt[3]{v_d(\mathbf{x}) + u(\mathbf{x}, t)}. \tag{3.7.20}$$

The results obtained in the previous two subsections are still appropriate since the effect of the background wind $\mathbf{v}_d$ on the steady-state rate of spread R^* can be seen as a shift, a linear increase, in the value of the steady-state wind field $(\mathbf{u} + \mathbf{v}_d)^*$. Obviously, if the background wind is much higher in magnitude, its contribution to the rate of spread R will be more significant than the contribution of the fire induced wind generated on any slope.

3.8. CONCLUSIONS

A novel coupling method between the atmosphere and fire models was developed in order to forecast wildfire spread. The single divergence equation of the atmosphere model, derived from a low Mach number approximation, makes it computationally efficient. The source term in this equation accounts for the heat released by the fireline. Its representation as a singular sink-source pair is consistent with the fireline geometry. The generated wind flow reproduces important plume features near the fireline, such as the indraft at the base of the fireline and the circulation pattern. The amplitude of the source is computed in a coherent manner with the fire intensity which depends on the fire rate of spread.

A dimensional analysis of the divergence equation led to a new dimensionless number Q. This parameter measures the importance of the fire induced wind flow magnitude relative to the background wind speed. This number was used to study the effect of the slope, fire intensity and background wind on the fire rate of spread for the two-dimensional case. A more extensive study of wildfire spread regimes over complex topography obtained with this novel coupled model will appear in a forthcoming paper.

Chapitre 4

SIMULATIONS AVEC LE MODÈLE COUPLÉ FEU-ATMOSPHÈRE ET ANALYSE DES RÉGIMES DE PROPAGATION DES FEUX DE FORÊT

Ce chapitre est constitué de l'article *Coupled Fire-Atmosphere simulations and Analysis of Forest Fire Spread Regimes*. L'article présente une étude des régimes de propagation avec le nouveau modèle couplé ainsi que des simulations aux fins de comparaison avec deux modèles existants. Les contributions principales de l'article sont :

(1) un nouvel algorithme et des méthodes numériques pour le couplage entre le modèle pour le feu et le modèle atmosphérique ;

(2) une étude des régimes de propagation des feux de forêt captés par le modèle avec une caractérisation en fonction du nombre adimensionnel pour l'amplitude du couplage Q, de la pente de la topographie et du vent initial ;

(3) une analyse comparative avec le modèle physique Firetec pour des topographiques idéalisées.

RÉSUMÉ

Cet article présente les simulations numériques obtenues avec un nouveau modèle couplé feu-atmosphère introduit dans un récent article [**82**]. Après la présentation des principales caractéristiques du modèle et de son implémentation numérique, une étude des régimes de propagation du feu pour diverses paramétrisations du modèle est présentée. Ces régimes sont analysés en fonction d'un nombre sans dimension qui caractérise l'intensité du feu relative à la magnitude du vent. Les simulations de la propagation du feu sur des topographies idéalisées et planes montrent que ce modèle arrive à reproduire des caractéristiques locales dans l'écoulement atmosphérique et des formes de propagation du feu obtenues avec des modèles couplés plus complexes.

COUPLED FIRE-ATMOSPHERE SIMULATIONS AND ANALYSIS OF FOREST FIRE SPREAD REGIMES

Louis-Xavier Proulx

ABSTRACT. This paper presents numerical simulations based on a novel coupled fire-atmosphere model introduced in a recent article [82]. After the presentation of the main model features and the numerical implementation of the model, a study of fire spread regimes is conducted. These regimes are analyzed as a function of a dimensionless number that characterizes the fire intensity relative to the background wind. Simulations of the fire propagation on flat and idealized topographies show that this model can reproduce local features of the flow and burn patterns obtained with more complex models.

4.1. INTRODUCTION

Coupled fire-atmosphere models have gained traction in the study of wildfire spread. Most models combine a mesoscale atmospheric model with a fire model which tracks the spread of the fireline. These are fully coupled in the sense that the wind velocity field affects the fireline rate of spread and the heat released by the fireline changes the local wind flow.

Research on coupled fire-atmosphere model started with the publication of two papers by Clark *et al.* [19, 20]. The importance of the fire-atmosphere coupling was well documented with the use of the CAWFE model [17, 21, 22, 23, 25, 26]. Other coupled models were developed such as the WRF-fire model [15, 24, 64, 65, 66, 77, 91, 92], the Forefire-MesoNH model [41, 42] and UU-LES model [100].

There are also more complicated physics models such as FIRETEC-HIGRAD [16, 29, 39, 58, 59, 60, 61, 62, 63, 69, 79, 80]. This model is based on a multi-phase transport approach coupled with a hydrodynamic atmosphere model. It thus brings more precision to the modeling of wildfire spread. It also exhibits self-determining properties and is intrinsically coupled. However, the model complexity makes it unusable for real-time forecasting.

These models have contributed to the understanding of wildfire spread, but they might not be fully suited for prediction purposes. They all use a mesoscale atmospheric model which requires significant computation time and resources. Beezley *et al.* [14] even concluded that local atmospheric features cannot be captured by the atmospheric model used by WRF-fire and thus the model is not designed for microscale simulations.

A quasi mass-consistent wind model combined with a new coupling paradigm led to a novel coupled model presented in a recent article [82]. This model falls in

between coupled models based on a mesoscale atmospheric model, which uses the primitive equations, and a mass-consistent model, based solely on the continuity equation. Forthofer [47] used this kind of approach to generate a more realistic wind to be used for simulations with Farsite [44]. The new atmospheric model is based on a single divergence constraint, similar to the one used by a mass-consistent model, but adds a source term that accounts for the heat released by the fireline.

The main goal of this model is to determine whether the use of a atmospheric model based on this divergence equation constraint combined with a sink-source term can achieve good predictions. The coupled model consisting of a single scalar divergence equation allows for fast simulations. A better understanding of core factors influencing the fire rate of spread will ultimately lead to an efficient prediction model.

This paper presents the main features of the fire and atmosphere models. The details of the coupling technique using a singular sink-source term are provided. A description of the numerical implementation and the model algorithm highlights the novelties of the coupled model. A study of the coupled model is pursued into three steps. First, the regimes of propagation on flat topographies are characterized using a non-dimensional intensity parameter Q as a function of the background wind and the topography slope. The results are compared to a previous study [82] conducted with the two-dimensional version of the coupled model. Numerical simulations of the fire spread are then performed on idealized topographies. A qualitative analysis of the fire induced wind flow and the burn patterns can reproduce non-trivial features of more complex coupled models. Finally, the coupled model is calibrated with the Firetec [61] model. The assessment of the numerical experiments is achieved with the propagation distance of the fire on idealized topographies.

4.2. Model features and coupling method

The derivation of the novel coupled fire-atmosphere model was detailed in a recent article [82]. This model was designed for forecasting purposes. The model brings a new approach for the atmospheric model and for the coupling. Rather than using a full mesoscale model, the atmospheric model is derived from a low Mach number approximation. This results in a single divergence equation with a singular sink-source term given as delta functions. The sink is supported on the fireline interface Γ and the source is defined on Γ_T, a vertical translation of the fireline. The choice of delta functions is consistent with the representation of the fireline as a curve. The divergence equation is a combination of the equations for conservation of mass and energy and the equation of state. The heat release rate is replaced by

Byram's fire intensity relation. The wind velocity field $\mathbf{u}$ thus satisfies the following:

$$\nabla \cdot \mathbf{u} = \frac{HmR(\mathbf{x},t)}{c_p \rho_0 T_0} (\delta(\Gamma_T) - \delta(\Gamma)) \equiv S \tag{4.2.1}$$

where R [m/s] is the fire rate of spread of the fireline Γ, H [kJ/kg] is the released combustion energy, m [kg/m^2] is the fuel load and $\delta(\Gamma_T) - \delta(\Gamma)$ is the sink-source pair. The source term S accounts for the amount of heat released by the fireline which perturbs the local wind flow.

The wind vector field $\mathbf{u}$ satisfying the divergence equation (4.2.1) is computed from a given initial background wind $\mathbf{v}$. It is decomposed as $\mathbf{v} = \mathbf{v}_d + \nabla\varphi + \nabla\chi$ where $\mathbf{v}_d$ is divergence-free. Assuming that $\Delta\chi = S$, a projection-like method leads to the elliptic problem:

$$\begin{aligned} \Delta\varphi &= \nabla \cdot \mathbf{v} - S, \\ \varphi^B &= 0 \quad \text{on the open boundaries,} \\ \frac{\partial \varphi^B}{\partial n} &= 0 \quad \text{on the topography,} \end{aligned} \tag{4.2.2}$$

where φ is a correction potential field used to find $\mathbf{u} = \mathbf{v} - \nabla\varphi$ satisfying equation (4.2.1). The Neumann condition applied on φ^B at the bottom boundary corresponds to a slip condition on the wind field $\mathbf{u}$. This condition was chosen since the wind flow was assumed to be inviscid and must therefore be tangent to the topography. The Dirichlet boundary conditions applied on top and side boundaries allow the wind to flow through these boundaries. This elliptic problem is solved on an irregular domain where the bottom boundary is defined by the topography.

The fireline is an interface, an infinitely thin curve Γ, that outlines the burned regions on the topography. The evolution of the interface is tracked numerically with the level set method. The method was adapted by Desfossés Foucault [**31**] in his PhD thesis in order to integrate Richards' ellipse model for fire propagation. The geometry of the topography is taken into account in the propagation velocity and the method is restrained to the projection of the interface in the $xy-$plane (Figure 4.1). This makes the method time efficient since the fire model is restrained to a two-dimensional function.

Since the heat release is concentrated along the fireline Γ, the source S is represented as a sink-source pair given by two delta functions: $\delta(\Gamma)$ supported on the fireline curve and $\delta(\Gamma_T)$ on the fireline curve vertically translated at a fixed distance above the fireline. The choice of the sink-source pair allows the reproduction of important features of the fire plume, such as the wind inflow at the base of the fire and the updraft above the fireline. It also creates a circulation pattern in the atmospheric flow along the fireline. The amplitude of the sink-source pair, the strength of the

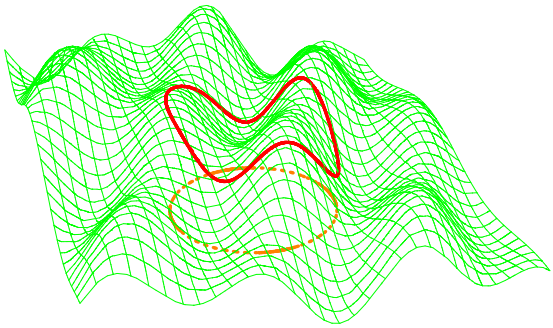

FIGURE 4.1. The level set method describing the evolution of the fireline (red curve) on the topography is simplified by considering the projection (orange circle) in the $xy-$plane.

induced wind flow, fluctuates along the fireline. It is controlled by the fire intensity which depends locally on the fire rate of spread and the fuel bed.

4.3. NUMERICAL IMPLEMENTATION

The coupled model combines two models. The first model tracks the evolution of the fireline and the second generates the wind velocity field. This section presents the numerical methods specific to each model. The computational solvers of the fire and wind models are implemented in two distinct codes. They are run consecutively so the models can exchange information before each execution. The fire model requires a wind velocity field for computing the fire rate of spread. The wind model needs the fire intensity for the generation of the wind flow. A communication pipeline was put in place for processing the information from one numerical model to the other. Challenges in the implementation, such as the use of two programming languages, are discussed. A description of the algorithm highlights the execution steps of the coupled model.

4.3.1. Elliptic solver

There are numerous numerical methods to solve the elliptic problem (4.2.2). The method must be able to deal with the irregularity of computational domain. An accurate representation of the topography is necessary, since its geometry will affect the structure of the wind flow. The method must also rely on a fast solver so the model can make fast predictions on the fireline evolution. These considerations are met with the embedded boundary method (EBM).

This approach developed by Colella and the Applied Numerical Algorithm Group (ANAG) [**8**, **52**, **57**, **89**] is based on a finite volume discretization of the divergence

operator in irregular cells of a computational grid. Special care is taken in the computation of the fluxes in the irregular cells. The method has been adapted for a mass-consistent wind model [**81**] to solve the elliptic problem (4.2.2) without the source term S.

The discretization of a $D-$dimensional space is achieved with control volumes centered on the Cartesian grid cells $\Upsilon_{\mathbf{i}} = [(\mathbf{i} - \frac{1}{2}\mathbf{u})h_d, (\mathbf{i} + \frac{1}{2}\mathbf{u})h_d]$, where $\mathbf{i} \in \mathbb{Z}^D$, h_d is the mesh space in direction d, and $\mathbf{u} \in \mathbb{Z}^D$ is the vector with all components equal to 1. The geometry of the irregular domain Ω is defined with an implicit function (level set) and is represented as the intersection with the Cartesian grid. This approach uses the control volumes $V_{\mathbf{i}} = \Upsilon_{\mathbf{i}} \cap \Omega$ and their faces $A_{\mathbf{i}\pm\frac{1}{2}\mathbf{e}_d}$ which correspond to the intersections of $\partial V_{\mathbf{i}}$ with the plane coordinates $\{\mathbf{x} : x_d = (i_d \pm \frac{1}{2})h_d\}$. The unitary vector in direction d is noted $\mathbf{e}_d$. The intersection of the irregular domain boundary with the Cartesian control volumes are the faces $A^B_{\mathbf{i}} = \Upsilon_{\mathbf{i}} \cap \partial\Omega$. These control volumes (cut cells) are the result from the intersection of the boundary, here the topography, and the rectangular cells of the Cartesian grid as illustrated in Figure 4.2. The discretized divergence operator requires the following geometric data of

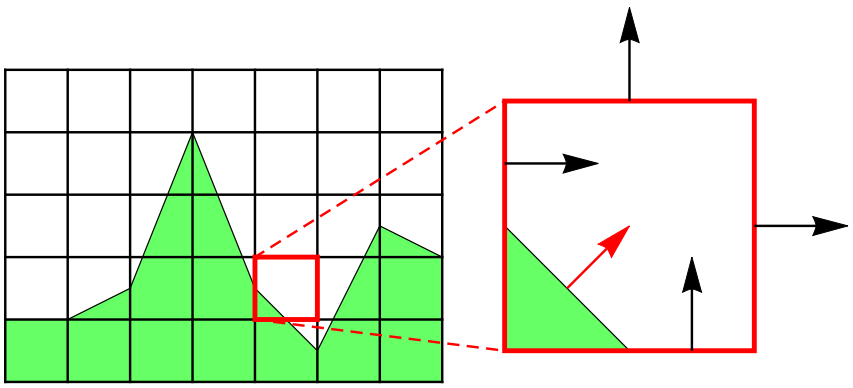

FIGURE 4.2. Embedded boundary on a Cartesian grid with fluxes at the face centroids of a given cut cell (irregular control volume).

the grid cells in non-dimensional terms:

$$\kappa_{\mathbf{i}} = |V_{\mathbf{i}}| \prod_{d=1}^{D} \frac{1}{h_d}, \tag{4.3.1}$$

$$\alpha_{\mathbf{i}\pm\frac{1}{2}\mathbf{e}_d} = |A_{\mathbf{i}\pm\frac{1}{2}\mathbf{e}_d}| \prod_{d'\neq d} \frac{1}{h_{d'}}, \tag{4.3.2}$$

where $\kappa_{\mathbf{i}}$ is the volume fraction and $\alpha_{\mathbf{i}\pm\frac{1}{2}\mathbf{e}_d}$ the face apertures. Boundary apertures $\alpha^B_{\mathbf{i}}$ must also be computed. These values are assumed to be computed with precision of order $O(h^2)$. Coordinates of face centroids $\mathbf{x}_{\mathbf{i}+\frac{1}{2}\mathbf{e}_d}$ in the domain and $\mathbf{x}^B_{\mathbf{i}}$ on the boundary as well as the outward normal $\mathbf{n}^B_{\mathbf{i}}$ can be computed with these explicit

formulas:

$$\mathbf{x}_{\mathbf{i}+\frac{1}{2}\mathbf{e}_d} = \frac{1}{|A_{\mathbf{i}+\frac{1}{2}\mathbf{e}_d}|}\int_{A_{\mathbf{i}+\frac{1}{2}\mathbf{e}_d}} \mathbf{x} dA, \tag{4.3.3}$$

$$\mathbf{x}_{\mathbf{i}}^B = \frac{1}{|A_{\mathbf{i}}^B|}\int_{A_{\mathbf{i}}^B} \mathbf{x} dA, \tag{4.3.4}$$

$$\mathbf{n}_{\mathbf{i}}^B = \frac{1}{|A_{\mathbf{i}}^B|}\int_{A_{\mathbf{i}}^B} \mathbf{n}^B dA, \tag{4.3.5}$$

where $\mathbf{n}^B$ is the outward normal at the boundary $\partial\Omega$ defined at each point on $\partial\Omega$. The precision of these values is again assumed to be order $O(h^2)$. An important advantage of this method is the accurate representation of complex geometries.

The elliptic equation of the form $\Delta\varphi = \rho$ can be written in conservation form:

$$\nabla \cdot \mathbf{F} = \rho, \tag{4.3.6}$$

where $\mathbf{F} = \nabla\varphi$ on the irregular domain Ω. The elliptic equation is solved on a Marker-and-Cell (MAC) grid where the potential φ is discretized at the cells center and the vector field on a staggered grid. The numerical scheme of the embedded boundary method uses a discretization of the divergence operator based on the divergence theorem. Let the fluxes $\mathbf{F} = (F^1, \ldots, F^D)$ be a function of $\mathbf{x}$. The midpoint rule leads to:

$$\nabla \cdot \mathbf{F} \approx \frac{1}{|V_{\mathbf{i}}|}\int_{V_{\mathbf{i}}} \nabla \cdot \mathbf{F} dV = \frac{1}{|V_{\mathbf{i}}|}\oint_{\partial V_{\mathbf{i}}} \mathbf{F} \cdot \mathbf{n} dA \tag{4.3.7}$$

$$\approx \frac{1}{\kappa_{\mathbf{i}} h}\left[\left(\sum_{\pm=+,-}\sum_{d=1}^{D} \pm\alpha_{\mathbf{i}\pm\frac{1}{2}\mathbf{e}_d} F^d(\mathbf{x}_{\mathbf{i}\pm\frac{1}{2}\mathbf{e}_d})\right) + \alpha_{\mathbf{i}}^B \mathbf{n}_{\mathbf{i}}{}^B \cdot \mathbf{F}(\mathbf{x}_{\mathbf{i}}{}^B)\right], \tag{4.3.8}$$

with the fluxes $\mathbf{F}$ located at centroids of cell faces. The treatment of boundary conditions is specified by the fluxes on the boundaries in the divergence operator. The homogeneous Neumann boundary condition applied at the bottom boundary leads to the flux $\mathbf{F}(\mathbf{x}_{\mathbf{i}}{}^B) = \mathbf{0}$. The expended divergence operator can then be written as

$$D^M(\mathbf{F})_{\mathbf{i}} = \frac{1}{\kappa_{\mathbf{i}} h}\left(\sum_{d=1}^{D} \alpha_{\mathbf{i}+\frac{1}{2}\mathbf{e}_d} F^d_{\mathbf{i}+\frac{1}{2}\mathbf{e}_d}(\mathbf{x}_{\mathbf{i}+\frac{1}{2}\mathbf{e}_d}) - \alpha_{\mathbf{i}-\frac{1}{2}\mathbf{e}_d} F^d_{\mathbf{i}-\frac{1}{2}\mathbf{e}_d}(\mathbf{x}_{\mathbf{i}-\frac{1}{2}\mathbf{e}_d})\right). \tag{4.3.9}$$

Homogeneous Dirichlet conditions for the top and side boundaries of the domain do not prescribe a value for the fluxes on these boundaries. Hence, a three-point stencil extrapolation is used for these fluxes. For instance, the flux on the right boundary in direction $d = 1$ is given by:

$$F_{\mathbf{i}+\frac{1}{2}\mathbf{e}_1} = \frac{1}{h_1}\left[3\left(\varphi^B - \varphi_{\mathbf{i}}\right) - \frac{1}{3}\left(\varphi^B - \varphi_{\mathbf{i}-\mathbf{e}_1}\right)\right]. \tag{4.3.10}$$

where φ^B is the value of φ on the boundary, here zero. The divergence operator requires the fluxes to be defined at the face centroid $\mathbf{x}_{\mathbf{i}+\frac{1}{2}\mathbf{e}_d}$ of each cell. For the full cell non-adjacent to the domain boundaries, the fluxes are computed with finite differences for the scalar field φ defined at the center of each cell. For the cut cells, the flux must be defined at the face centroid. This is achieved with a bilinear interpolation using the flux values of the neighboring cells. A relaxation method based on Gauss-Seidel iteration is used with red-black ordering.

The embedded boundary method has been made available by the ANAG team under EBChombo [**9**], a collection of C++ libraries based on the infrastructure of the Chombo [**27**] software [1]. Additional libraries were added in order to implement the model. These new libraries consist of routines for:

— writing the topographies definition files for grid generation with an implicit function $\psi(\mathbf{x})$;
— initializing the initial wind field $\mathbf{v}$ at the center of cell faces ;
— calling the elliptic solver with the appropriate boundary conditions ;
— building HDF5 files for reading the delta function and writing the projected wind field $\mathbf{u}$.

4.3.2. Level set method and delta regularization

The level set method is used for tracking the evolution of the fireline interface on the topography. This method was adapted by Desfossés Foucault [**31**] and implemented in MATLAB [**67**]. The zero level set of the function ϕ corresponds to the projection of the fireline in the $xy-$plane. The level set function ϕ can be written in the Hamilton-Jacobi form:

$$\phi_t + \mathscr{H}(\nabla\phi) = 0,$$

where the Hamiltonian is

$$\mathscr{H}(\nabla\phi) = \|A\nabla\phi\| + \mathbf{C}\cdot\nabla\phi. \tag{4.3.11}$$

The matrix A and the vector $\mathbf{C}$ are defined in the following manner:

$$A = \begin{pmatrix} b & 0 \\ 0 & a \end{pmatrix} R_\theta, \qquad \mathbf{C} = R_\theta \begin{pmatrix} 0 \\ c \end{pmatrix}, \tag{4.3.12}$$

where a, b and c are the fire propagation speed parameters and R_θ is the rotation matrix with θ being the wind direction with respect to the $y-$axis. The Hamiltonian

1. Version 3.0 of Chombo was used for this project.

$\mathscr{H}$ can be defined in the convenient form:

$$\mathscr{H}(\nabla\phi) = F\left(\frac{\nabla\phi}{\|\nabla\phi\|}\right)\|\nabla\phi\|, \tag{4.3.13}$$

where the function F is the fireline normal rate of spread which depends on the interface orientation. This speed can be computed with $\nabla\phi = (\phi_x, \phi_y)$, the gradient of the level set function. In this model, the level set method is initialized with a signed-distance function. After each time-step, a reinitialization algorithm forces the level set function to remain a signed distance function. A property of a signed distance function is that its gradient norm $\|\nabla\phi\| = 1$. The Hamiltonian can thus be written as $\mathscr{H}(\nabla\phi) = F(\nabla\phi)$. This property of the level set function allows an easy computation of projected normal speed of the zero level set.

The normal speed F is the normal rate of spread in the $xy-$plane. This speed can be computed on the topography $h(x, y)$ in order to get the normal rate of spread R:

$$R = F\sqrt{1 + (h_x\phi_x + h_y\phi_y)^2} \tag{4.3.14}$$

where h_x, h_y, ϕ_x and ϕ_y denote the x and y derivative of the topography function $h(x, y)$ and level set function ϕ. The normal rate of spread $R(\mathbf{x}, t)$ is used to compute the amplitude of the sink-source pair in the divergence equation:

$$\nabla\cdot\mathbf{u} = \frac{HmR(\mathbf{x}, t)}{c_p\rho_0 T_0}(\delta(\Gamma_T) - \delta(\Gamma)) \tag{4.3.15}$$

where Γ is the fireline on the topography and Γ_T is the fireline curve translated vertically above the topography at a fixed distance d_δ. This doublet acts as the feedback from the fire model to the atmosphere model. The amplitude of the sink-source pair varies in time and along the fireline Γ according to the normal rate of spread $R(\mathbf{x}, t)$.

A new regularization technique for delta functions supported on codimension-2 manifolds was developed in [**83**]. This technique addresses the challenges coming from the irregularity of the computational grid in the atmosphere model. The fact that the singular source lies on the bottom boundary of the domain has also been taken into account for the regularization of the delta function. The interface Γ, the support of the delta function, is represented as the intersection of two level set functions.

The fire model already provides the level set function for the projected evolution of the fire $\phi(x, y, z, t)$. Since the height of the topography $h(x, y)$ is assumed to be known at each grid point, a steady level set function for the topography can be given by

$$\psi(x, y, z) = h(x, y) - z. \tag{4.3.16}$$

The level set function $\phi(x, y, z, t)$ can be projected back on the topography $h(x, y)$ in order to get the level set function $\Phi(x, y, z = h(x, y), t)$ for which the zero level set represents the fireline on the topography. The delta function can then be written as the product of these two delta functions supported on their respective level set function:

$$\delta(\Gamma) = \delta(\psi(\mathbf{x}))\delta(\Phi(\mathbf{x}, t)) \tag{4.3.17}$$

where $\mathbf{x} = (x, y, z)$ is the position and $\Phi(\mathbf{x}, t)$ is the fire interface on the topography. The translated delta function $\delta(\Gamma_T)$ is defined in the same manner. Figure 4.3 illustrates this regularization in the case of a circle-shaped fireline Γ on a horizontal plane topography $\psi(\mathbf{x})$.

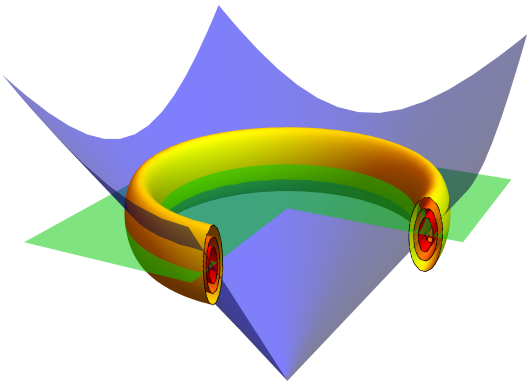

FIGURE 4.3. Sliced contours of the regularized delta function on a circle shaped fireline Γ. The circle is the intersection of the green plane topography $\psi(\mathbf{x})$ and the blue level set function $\Phi(\mathbf{x}, t)$ tracking the fireline.

The amplitude of the delta functions is defined as

$$\mathscr{M}(\mathbf{x}, t) = \frac{HmR(\mathbf{x}, t)}{c_p \rho_0 T_0}. \tag{4.3.18}$$

It changes in time and along the fireline interface since it depends directly on the normal rate of spread $R(\mathbf{x}, t)$. Hence, the amplitude of each delta function of the sink-source pair must be defined locally.

The regularization method presented in [**83**] is coupled to a local rescaling technique in order to force the delta function to satisfy a first moment condition. This technique requires a piecewise line segment representation of the zero level set of function ϕ such as in Figure 4.4. The rescaling process rescales the delta weights assigned to each line segment so that they add up to the length of the line segment.

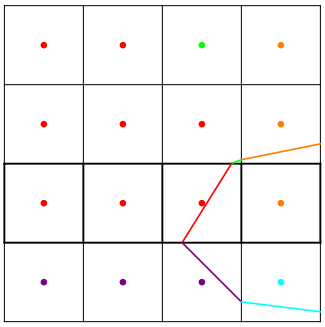

FIGURE 4.4. Line segment representation of the fireline in the $xy-$plane. The dots are the weights of the regularized delta assigned to each line segment.

The same rescaling technique can now be used to assign the computed local amplitude $\mathscr{M}(\mathbf{x},t)$. Rather than rescaling the local weights by the length of the line segment, it is rescaled by the local amplitude.

The rate of spread of the level set function ϕ is computed with the Hamiltonian $\mathscr{H}(\nabla\phi)$ in equation (4.3.11) and depends on the a, b and c parameters in equation (4.3.12). The forward rate of spread is defined as $R = a + c$. The back rate of spread is equal to $a - c$. The flank rate of spread is controlled by the parameter b. These three parameters are computed from the wind velocity as follows:

$$\begin{aligned} a &= R_0 + \frac{9}{20}\sqrt[3]{u(x,t)}, \\ b &= R_0 + \frac{1}{5}\sqrt[3]{u(x,t)}, \\ c &= \frac{11}{20}\sqrt[3]{u(x,t)}, \end{aligned} \tag{4.3.19}$$

where R_0 is the fire rate of spread in absence of wind depending on the fuel bed composition and terrain slope and u is the contribution of the local wind flow. The choice of the wind contribution follows a typical approach taken in fire spread modeling community. The wind affecting the fire rate of spread is taken at a fixed distance $d_{\mathbf{u}-\Gamma}$ from the fireline Γ and tangent to the topography. This is necessary since the wind directly above the fireline has zero horizontal components and cannot contribute to the fireline rate of spread. This distance is taken in the normal direction to the fireline Γ and in the opposite direction of the spread. The wind is also chosen at a fixed height vertically above the topography $d_{\mathbf{u}-h}$.

4.3.3. Pipeline

The coupled model is made up of two code modules. The elliptic solver is implemented in `C++` language from libraries packaged under EBChombo. The level set

method and regularization of the delta functions are coded in MATLAB. Solving the elliptic equation is the most time-consuming operation since the problem is solved on a 3D domain. Fortunately, its implementation in C++ makes it efficient. The level set method is solved as a 2D problem since only the projection of the interface in the $xy-$plane needs to be tracked.

A pipeline between the two codes was implemented in order to pass information from one code to the other. The HDF5 files, which were already used by EBChombo for outputting data for visualization, were used to store and exchange the information required by the two codes. Basically, the MATLAB code outputs the delta functions regularized on the appropriate level set functions. Chombo reads this file and loads the delta functions in the right-hand side term of the Poisson equation (4.2.2). It solves the elliptic problem and computes the projected velocity field $\mathbf{u}$. This wind field is then stored in a HDF5 file and sent to MATLAB. The level set code in MATLAB uses this wind field $\mathbf{u}$ to compute the a, b and c parameters of the ellipse which define the level set rate of spread $R(\mathbf{x}, t)$. The different steps involved in the pipeline are summarized:

(1) Chombo computes and outputs the geometric data (such as the volume fraction $\kappa_\mathbf{i}$) of the irregular domain.

(2) MATLAB regularizes the delta functions on the interfaces Γ and Γ_T using the volume fractions $\kappa_\mathbf{i}$ and sends the regularized delta functions to Chombo.

(3) Chombo adds the delta functions to the right-hand side term of the Poisson equation, solves it on the irregular domain and projects the velocity field. The final velocity field is sent to MATLAB.

(4) MATLAB uses the projected velocity field to spread the interface with the level set function.

(5) The code starts over to step 2 with the new position of the interface.

Between each step, the Chombo and MATLAB codes hold their execution and wait for a signal of the other program to continue the execution. The details of the numerical algorithm for coupling the fire and atmospheric models are given below.

4.3.4. Algorithm

The two governing equations of the coupled model are:

$$\frac{\partial \phi}{\partial t} + \left\| A \nabla \phi \right\| + \mathbf{C} \cdot \nabla \phi = 0 \tag{4.3.20}$$

$$\nabla \cdot \mathbf{u} = \frac{H m R(\mathbf{x}, t)}{c_p \rho_0 T_0} \left(\delta(\Gamma_T) - \delta(\Gamma) \right). \tag{4.3.21}$$

The first equation tracks the evolution of the fireline on the topography. The ellipse parameters a, b and c stored in the matrix A and vector $\mathbf{C}$ depend on the wind velocity $\mathbf{u}$. The second equation is a constraint on the divergence of the wind velocity field with a source term representing the perturbation of the fire heat release. The rate of spread R is computed from the ellipse parameters.

The atmosphere model is quasi-stationary. The wind flow $\mathbf{u}$ in the divergence equation (4.2.1) does not depend explicitly on the time t. Its time-dependence comes from the source term which requires the rate of spread $R(\mathbf{x}, t)$ computed by the level set algorithm. This means that, between each time step of the level set method, the dynamics of the atmospheric flow are adjusted infinitely fast. Therefore, the velocity field $\mathbf{u}$ must be fully converged, stable, before advecting the fireline at the next time step.

This feature must be taken into account when coupling the fire and atmosphere models. It means that sub-iterations of the atmosphere model are required between each time step of the fire model. This iterative process ensures the computation of a converged wind velocity field $\mathbf{u}$. The convergence for this problem is fast, but it is necessary that the model start with a fully converged solution of the elliptic problem. The time steps in the simulations are relatively small, it can be assumed that the atmospheric flow is not perturbed much between each time step. Therefore, it does not require many iterations to reach a stable solution. For this coupled model, 5 iterations of the atmosphere model were performed between each time step of the fire model.

The two equations are solved with their appropriate numerical method on their respective grids. The atmosphere model relies on the embedded boundary method (EBM) which uses a Marker-and-Cell (MAC) grid where the potential field is cell-centered. The level set function ϕ is defined on the vertex-centered grid. These grid meshes are illustrated in Figure 4.5. The subscript l refers to the level set grid (red dots), the subscript c to the cell-centered grid (blue dots) and the subscript e to the edge-centered vector field (purple/magenta arrows).

The algorithm is implemented in three major steps. The initialization step defines the topography and initializes the level set function as well as the background wind field. The second step iterates a number of times in order to compute a converged rate of spread R. Then, the level set equation is solved for this time step. The algorithm is described in detail below.

(1) **Initialization**

   (a) Compute the topography level set function: $\psi^-(x_l, y_l, z_l) = h(x_l, y_l) - z_l$ and interpolate $\psi_l^- \rightarrow \psi_c^-$.

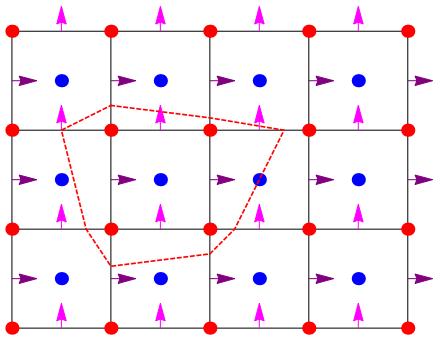

FIGURE 4.5. Two overlapping Cartesian grids. The grid used by the level set solver and for the discretization of the topography is represented by red dots. The MAC grid is pictured by cell-centered blue dots (for scalar fields) and staggered edge-centered vector field. The red dashed line is a representation of the zero level curve of the level set function.

(b) Compute the volume fractions $\kappa_{\mathbf{i}}$ of the Cartesian grid.

(c) For a fixed vertical height between the sink and source d_δ, compute the vertical translation of the topography function $\psi^+(x_l, y_l, z_l) = h(x_l, y_l) - z_l + d_\delta$ and interpolate $\psi_l^+ \to \psi_c^+$.

(d) Compute the projected background velocity field $\mathbf{v}(x_e, y_e, z_e, t^0)$ and interpolate it on the level set grid: $\mathbf{v}_e^0 \to \mathbf{v}_l^0$.

(e) Initialize the level set function $\phi(x_l, y_l, z_l, t^0)$.

(f) Compute the surface wind taken from a vertical distance $d_{\mathbf{u}-h}$ above the topography.

(g) Compute the ellipse parameters a_l^0, b_l^0 and c_l^0 using the topography slope and the surface wind velocity $\mathbf{v}_l^0$ at a distance $d_{\mathbf{u}-\Gamma}$ from the fireline Γ and tangent to the topography.

(h) Compute the projected normal rate of spread R_l^0 of the level set function.

(2) **Computing a converged rate of spread**. For each time step n of the level set algorithm, loop over the following steps to compute a converged rate of spread of the level set function:

(a) Interpolate $\phi_l^n \to \phi_c^n$ and compute the level set function Φ_c^n from ϕ_c^n.

(b) Regularize the two delta functions:

$$\delta_c^n = \delta(\Phi(x_c, y_c, z_c, t^n); \psi_c^+) - \delta(\Phi(x_c, y_c, z_c, t^n); \psi_c^-).$$

(c) For each line segment ϕ_l^n, compute the amplitude of the delta functions (i.e. fireline intensity) using the normal rate of spread R_l^n on the topography.

(d) Rescale δ_c^{n+1} using R_l^n, ϕ_l^n and the volume fractions κ.

(e) Solve $\Delta\varphi(x_c, y_c, z_c, t^n) = (\nabla\cdot\mathbf{v}(x_e, y_e, z_e, t^n))_c - \delta_c^n$ for $\varphi_c^n = \varphi(x_c, y_c, z_c, t^n)$. Here φ_c^n does not explicitly depend in t^n. The time dependence comes from the delta function δ_c^n.

(f) Project the vector field: $\mathbf{v}(x_e, y_e, z_e, t^*) = \mathbf{v}(x_e, y_e, z_e, t^n) - (\nabla\varphi_c^n)_e$ and interpolate it on the level set grid: $\mathbf{v}_e^* \to \mathbf{v}_l^*$.

(g) Compute the surface wind taken from a vertical distance $d_{\mathbf{u}-h}$ above the topography.

(h) Compute the ellipse parameters a_l^n, b_l^n and c_l^n using the topography slope and the surface wind velocity $\mathbf{v}_l^n$ at a distance $d_{\mathbf{u}-\Gamma}$ from the fireline Γ and tangent to the topography.

(i) Compute the projected normal rate of spread R_l^n of the level set function.

(j) Loop over from step (2)(c) until $\mathbf{v}_e^*$ (R_l^n equivalently) has converged to its stable steady state.

(3) **Level set iteration**. Solve the level set equation for one time step: $\phi_l^n \to \phi_l^{n+1}$ using the steady state $\mathbf{v}_l^{n+1} = \mathbf{v}_l^*$.

(4) **Loop over** from step (2).

Note that the delta function at time t^{n+1} is rescaled using the rate of spread R_l^n computed at the previous time t^n. The rate of spread cannot be computed at t^{n+1}, since it requires the vector field at the same time t^{n+1}. This vector field is found using the delta function also at time t^{n+1}. Hence, one must make a choice of what is computed first.

It is also more efficient to do the iterations on the wind velocity field than taking smaller time step in the level set algorithm. Since the matrix for the elliptic problem is already constructed for a given position of the fireline, it only needs to update the amplitude of the delta function which appears in the source term S in the right-hand side of the Poisson equation (4.2.2). An exploration of the model capacity and an analysis of the forest fire spread regimes are conducted in the next sections.

4.4. Regimes of propagation on flat topographies

Rather than using a mesoscale atmosphere model, the coupled model features a simpler wind model based on a single divergence equation (4.3.15). A singular sink-source perturbation in the divergence equation acts as a fire feedback onto the atmospheric flow. The ultimate purpose of this model is to be used as a forecasting tool for wildfire spread. The relative simplicity of this model makes it numerically

efficient. The remaining step is to determine which characteristics of the wind flow and the fireline spread this model can replicate. The simple atmospheric model cannot pretend to generate fully featured flows such as those of a mesoscale atmospheric model. It may nevertheless be able to reproduce some of the fireline behavior simulated with more complex models.

This section presents a study of the regimes of propagation on flat inclined topographies with the coupled model. Preliminary results for the 2D model were discussed in [**82**]. A dimensional analysis led to a dimensionless number Q which characterizes the intensity of the fire feedback onto the wind flow compared to the background wind. The contribution of the fire induced wind flow to the rate of spread R was studied. The main parameters affecting the rate of spread are the topography slope α, the fire intensity parameter Q and the background wind $\mathbf{v}_d$. The following questions will be addressed:

(1) Is there a non-trivial effect of the coupling on the fire spread?

(2) Does the rate of spread R change with the intensity parameter Q and the slope angle α in the same manner as in the 2D model [**82**]?

For the sake of simplifying the analysis and to be able to answer these questions, the experiments will be done on plane topographies with different inclinations. The horizontal flat surface ($\alpha = 0°$) is used to study the effect of the fire-induced wind, generated with different intensities Q, on the propagation of the fireline. The plane topographies are defined using their normal vector and the origin being an initial point. For each plane, the normal has the form $\mathbf{n} = (-\tan(\alpha), 0, 1)$, where the parameter α is the angle between the plane topographies and the $xy-$plane. Theses surfaces are shown in Figure 4.6. The computational domain is $640 \times 320 \times 320$ m. The number of grid cells is $160 \times 80 \times 80$ which implies a mesh size of 4 m in each direction.

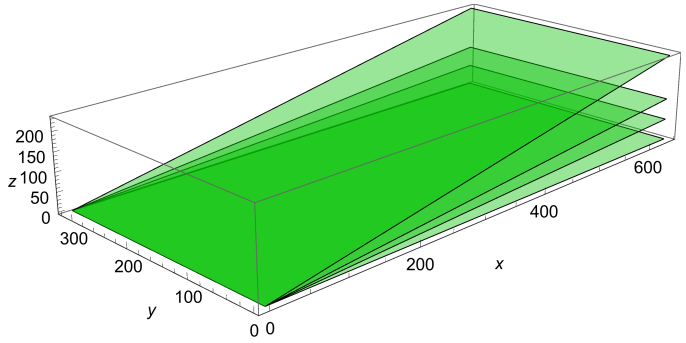

FIGURE 4.6. Four plane topographies with inclining angle $\alpha = 0, 5, 10, 20°$.

The coupled model also has its specific parameters. The delta function representing the fire heat release is computed as a product of two regularized delta functions

supported on the level set functions $\psi(\mathbf{x})$ and $\Phi(\mathbf{x}, t)$ given by equation (4.3.17). Each of these delta functions is regularized using a Gaussian approximation (see [**83**]) with the half-width support parameter ε. The parameter d_δ is the vertical distance between the sink and source. The wind vector that will affect the local rate of spread is taken at a constant height $d_{\mathbf{u}-h}$ above the topography and at a fixed distance $d_{\mathbf{u}-\Gamma}$ from the fireline Γ, tangent to the topography. The distance $d_{\mathbf{u}-\Gamma}$ is computed in the normal direction to the fireline Γ and in the opposite direction of the spread. These parameters have been set to a constant value for all experiments in this article as shown in Table 4.I.

Parameters	Values
ε [m]	8
d_δ [m]	40
$d_{\mathbf{u}-h}$ [m]	16
$d_{\mathbf{u}-\Gamma}$ [m]	15

TABLE 4.I. Coupled model parameter values for all simulations.

4.4.1. Qualitative analysis

Before the analysis of the propagation regimes, Figures 4.7-4.10 present the fireline contours and streamlines of the wind flow at different times with the parameter $Q = 1500$. The background wind has a magnitude of 6 m/s and is horizontal. The rate of spread in absence of wind is $R_0 = 0.5$ m/s. The inflow comes from the left boundary and exits through the right boundary of the domain. The fireline is ignited such that its projection in the horizontal plane is a circle of radius 35 m centered in the domain at $(300, 160)$. Figures 4.7 shows the contour lines over the flat surface. The fire grows in a teardrop shape when the coupling between the fire and atmosphere models is enabled.

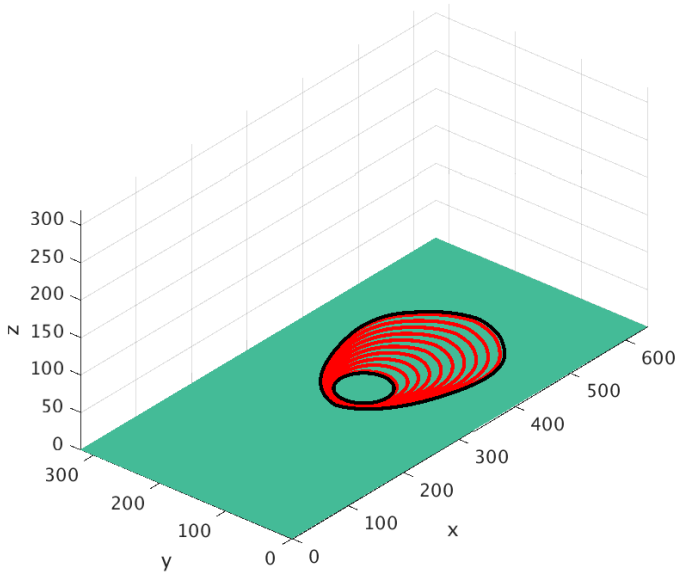

FIGURE 4.7. Fireline spread over the horizontal flat topography ($\alpha = 0°$).

The streamlines in Figures 4.8, 4.9 and 4.10 reveal the particular features of the wind flow for which the coupled model was developed. The flow convergence at the head fire is visible in Figure 4.8. This phenomena is caused by the sink-source pair which generates the entrainment of air near the fireline. In absence of the coupling, the streamlines would appear as straight parallel lines running from the left side to the right side of the domain.

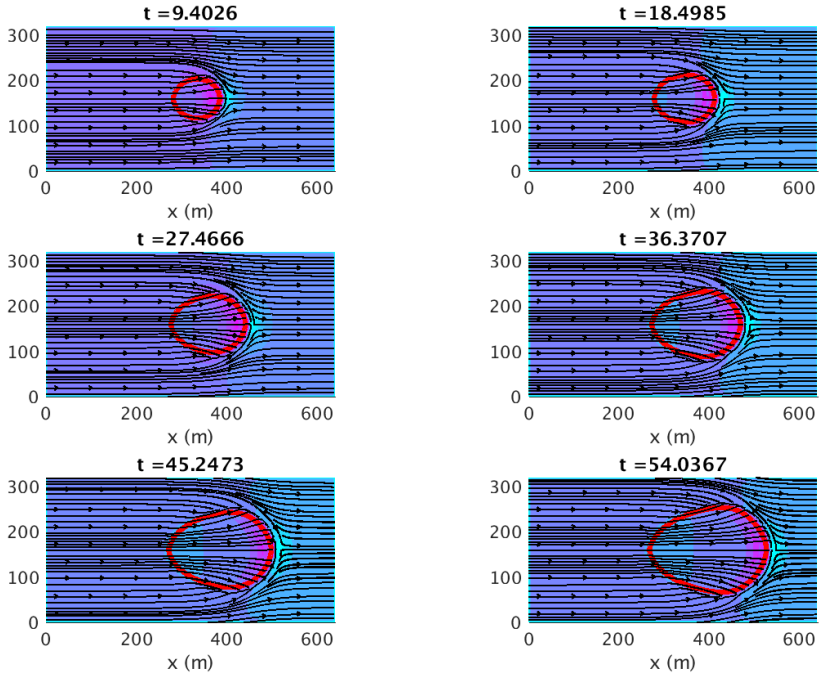

FIGURE 4.8. Fireline (red), streamlines and velocity magnitude in the projected plane for the horizontal flat topography ($\alpha = 0°$). The magenta and cyan colors indicate high and low wind magnitudes respectively.

The downdraft behind the head fire appears clearly in Figure 4.9. Figure 4.10 shows the circulation pattern. The wind velocity magnitude is particularly strong near the fireline due to the local perturbation of the wind flow caused by fireline heat release.

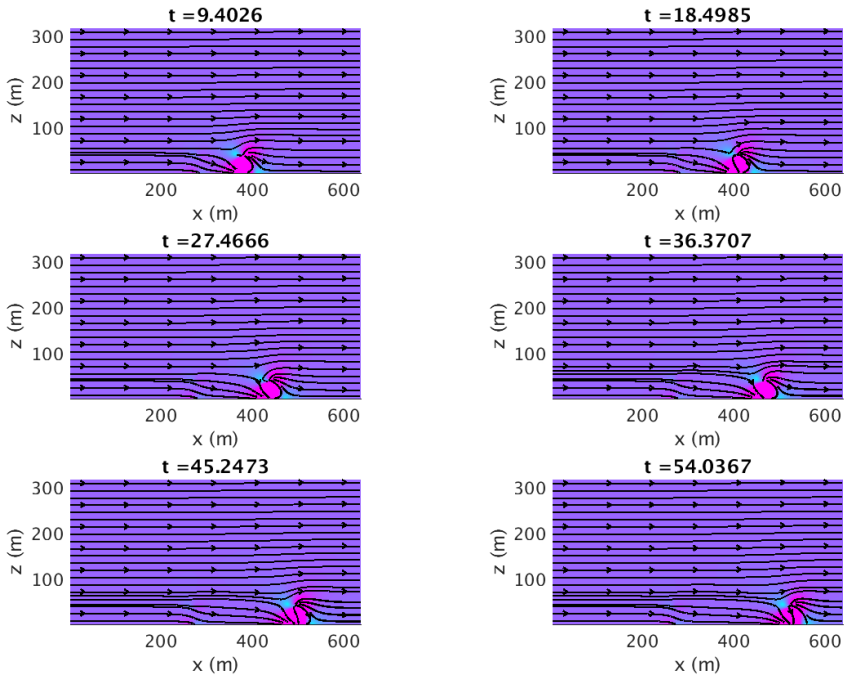

FIGURE 4.9. Fireline, streamlines and velocity magnitude in the $y = 160$ plane for the horizontal flat topography ($\alpha = 0°$). The magenta and cyan colors indicate high and low wind magnitudes respectively.

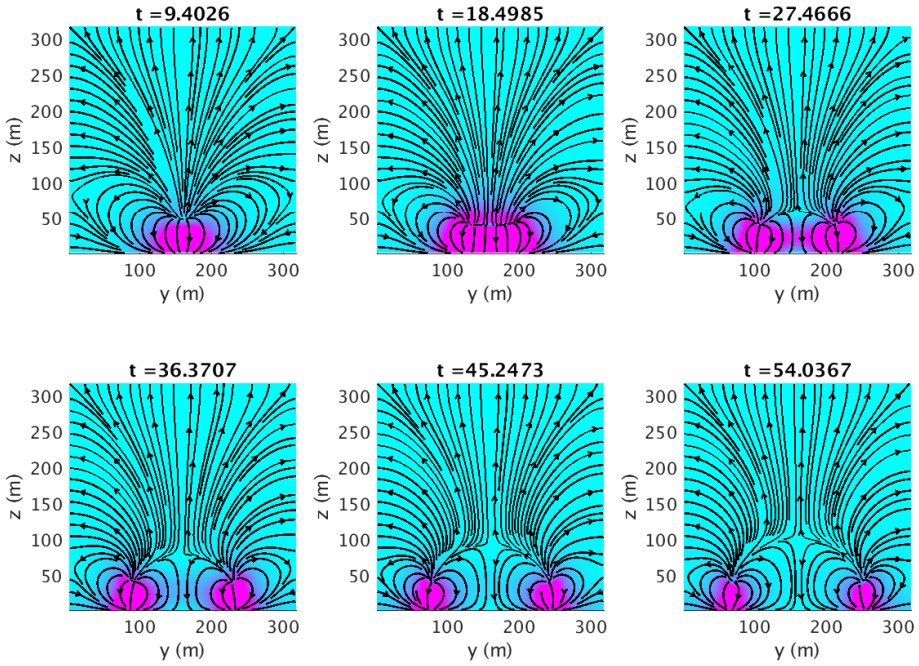

FIGURE 4.10. Fireline, streamlines and velocity magnitude in the $x = 400$ plane for the horizontal flat topography ($\alpha = 0°$). The magenta and cyan colors indicate high and low wind magnitudes respectively.

Figure 4.11 shows the contours of the fireline for different values of the coupling parameter Q. When $Q = 0$, there is no coupling between the atmosphere and the fire models, which means there is no perturbation of the wind flow by the fireline heat release. As the value of the parameter Q increases, the fireline feedback onto the atmosphere becomes more important and will affect significantly the rate of spread in every direction.

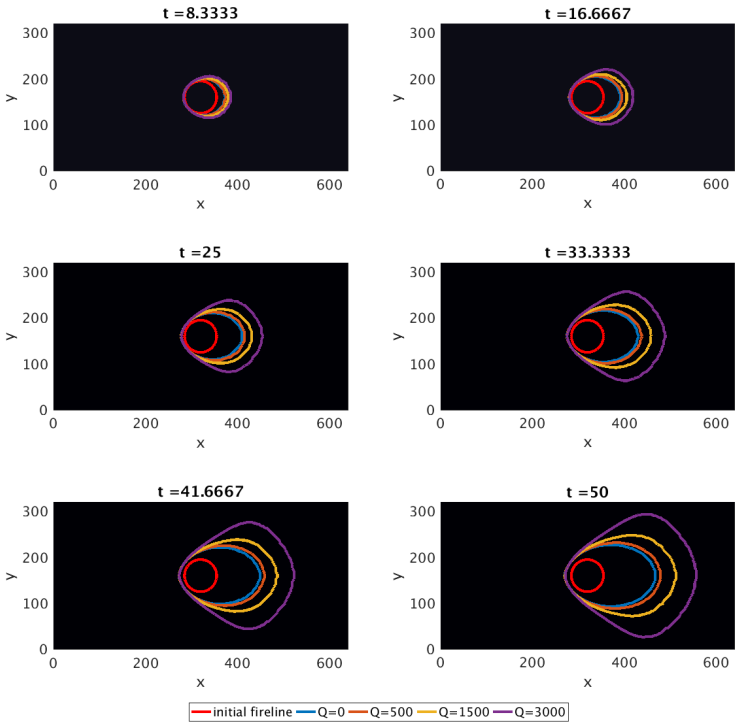

FIGURE 4.11. Fireline over the horizontal flat topography ($\alpha = 0°$) at 6 different times for $Q = 0$ (no coupling) and $Q = 500, 1500, 3000$ (coupled model).

A first consequence of the coupling is the changes in the fire shape. Initially, the fireline seems to grow as an ellipse for any given value of the parameter Q. After 50 seconds, it is clear that there are two resulting fire shapes: ellipse and teardrop. When there is no coupling ($Q = 0$) or a weak fire intensity ($Q = 500$), the burned region grows in the well-know ellipse shape. When the parameter Q is sufficiently large, the fireline adopts a teardrop shape. This behavior has been studied by Canfield *et al.* [**16**] with Firetec. This can be explained by the increase of the indraft flow at the head part, but also at the flanking portion of the fireline. In this case, the induced wind velocity field adds a strong contribution to the flank rate of spread for which the background does not contribute much.

Richards [87] tried to reproduce the teardrop shape in applying variations in the wind speed with its ellipse model. He was unable to change the shape of the fire from an ellipse to a teardrop shape. He concluded that the reproduction of this fire shape might be due to other factor such as fuel type and distribution. In the simulations above, the fuel bed is uniform across the topography. The local indraft near the fireline clearly enables the teardrop fire shape. One can therefore conclude that this non-trivial behavior of the fire propagation is directly caused by the fire heat release. This is the central piece of the coupling between the fire and the atmosphere models.

4.4.2. Regimes for the 3D setting

The figures above have shown the qualitative behavior of the fire spread. The same simulations were executed on the inclined planes in order to study the effect of slope α and parameter Q on the rate of spread. This study has been conducted with the 2D version of the coupled model in a recent article [82]. Figure 4.12 presents the steady-state fire rate of spread R as a function of the slope angle α for different magnitudes of Q. Note that the for $\alpha = 0°$, the rate of spread is about 1.8 m/s when $Q = 10$ and about 9 m/s when $Q = 1000$.

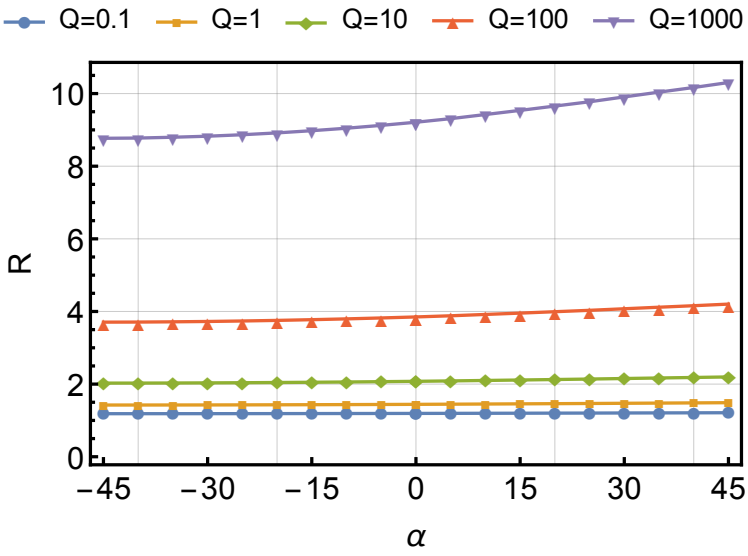

FIGURE 4.12. Stable rate of spread of the fire R^* as a function of the slope angles $\alpha \in [-45°, 45°]$ (5° increments) for the fire intensity parameter $Q = 10^k$ with $k = -1, 0, 1, 2, 3$.

The experiments in 3D for the plane cases were conducted until a fully converged rate of spread R was computed. The intensity parameter Q was set to 0, 10, 100 and 1000. The results are shown in Figure 4.13 when there is no background wind,

but only the fire induced wind. As in Figure 4.12, the curves are increasing with the value of the slope angle α. This behavior is recurrent for any value of the parameter Q. The magnitude of the rate of spread R increases when the value of Q gets bigger, but the values are not the same. This might be explained by two factors. First, the fire rate of spread was computed along the $y = 160$ axis at the head fire. This is a very local measurement of a complex structured flow. Second, the fireline is a curve rather than a point. Hence the flank rate of spread can alter the normal rate of spread at the head fire. The magnitudes of the converged rate of spread R are different bet-

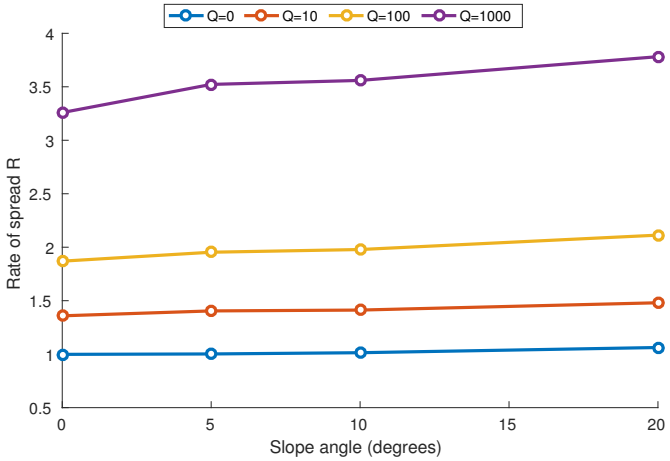

FIGURE 4.13. Stable rate of spread of the fire R^* in absence of background wind as a function of the slope angles $\alpha = \{0, 5, 10, 20°\}$ for the fire intensity parameter $Q = \{0, 10, 100, 1000\}$.

ween the 2D and 3D models, but the way R changes as a function of Q for a fixed value of the slope angle is the same. In fact, a linear change in Q does not lead to a linear variation of R^*. The relation between the two is the inverse cubic root which is explained by the model (4.3.19) used for computing the rates of spread. For a fixed value of the parameter Q, the rate of spread R increases as the slope α increases. Like in the 2D model, the fire induced wind flow by the sink-source pair accounts for the effect of the slope on the rate of spread. The relationship between the slope angle α and the rate of spread R^* is not linear but rather quadratic.

4.5. SIMULATIONS ON IDEALIZED TOPOGRAPHIES

In this section, the coupled model is studied for simulations of the fire spread over complex topographies. Linn *et al.* [**61**] defined four idealized topographies in order to explore the coupling between the atmosphere and the fire. A qualitative analysis focuses on the impact of the complex geometry of the terrain surface on the shape of the burned region. Special attention is directed at the combined effect of the fire induced flow quantified by the parameter Q. The main questions are:

(1) Does the sink-source pair reproduce the main features of fire plumes?

(2) Are the main features (such as convergence zones) of the wind flow preserved as the fire spreads?

(3) What is the effect of the parameter Q on the propagation of the fireline?

(4) Do the burned areas have similar shapes when Q increases?

The four idealized topographies were first defined in the article by Linn *et al.* [**61**]. The horizontal domain for each surface has a length of 640 m and a width of 320 m. The topographies are constructed from the same basis surface function $b(x)$:

$$b(x) = 55 + 40 \arctan\left(\frac{(x-300)-140}{60}\right) \tag{4.5.1}$$

which corresponds to a hill. The basis function is designed such that the topographies have the same height along the centerline axis $y = 160$ m from $x = 300$ m to $x = 640$ m. In each case, the elevation reaches 106 m at (640, 160) m. The four idealized topographies are defined in the following manner:

$$H_{hill}(x,y) = b(x) \tag{4.5.2}$$

$$H_{canyon}(x,y) = \begin{cases} 55 + 40 \arctan\left(\dfrac{|x-300|-140}{60}\right) & \text{for } x < 300 \text{ m} \\ b(x) & \text{for } x \geq 300 \text{ m} \end{cases} \tag{4.5.3}$$

$$H_{upcan}(x,y) = \left(\frac{|y-160|}{160}\right)^{3/2} \times b(x) + b(x) \tag{4.5.4}$$

$$H_{ridge}(x,y) = -\left(\frac{|y-160|}{160}\right)^{3/2} \times b(x) + b(x). \tag{4.5.5}$$

Each of these surfaces is illustrated in Figure 4.14. For the upcan surface, the maximal height is 211 m on the edge of the domain and for the ridge, the height decreases to only 1 m on the same edges. The simulations of the coupled model use the parameter values of Table 4.I and the following Table 4.II.

The initial wind is uniform and horizontal in the direction of the positive $x-$axis. This background wind is corrected by the model so that it becomes tangent to the topography and is divergence-free. The height of the domain is fixed at 320 m. The

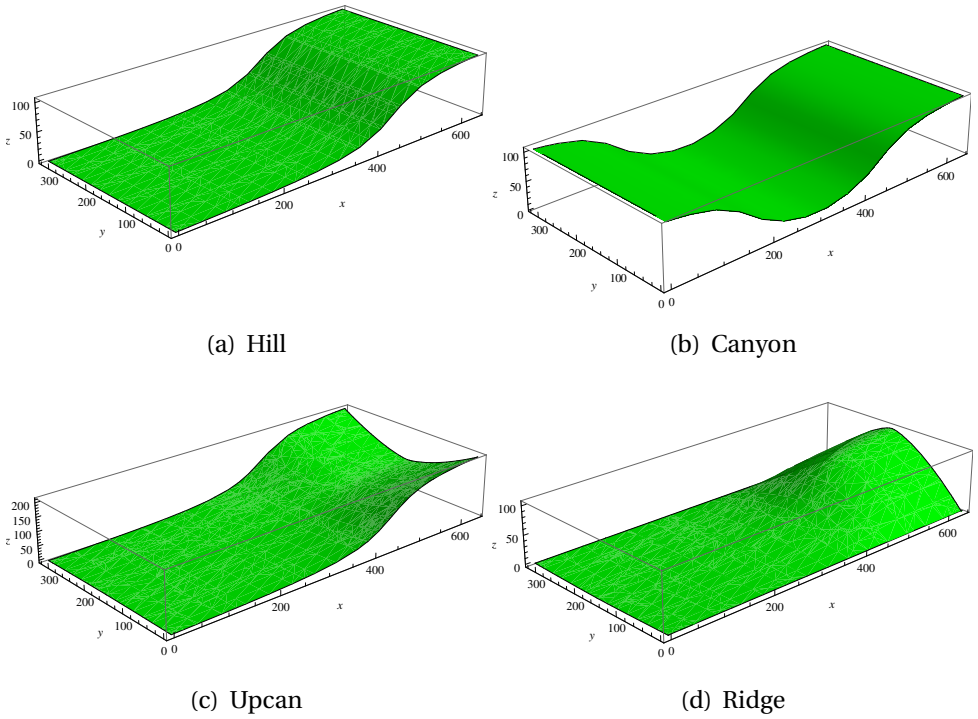

(a) Hill (b) Canyon

(c) Upcan (d) Ridge

FIGURE 4.14. Four idealized topographies: hill, canyon, upcan and ridge.

Characteristics	Coupled model
Domain	$640 \times 320 \times 320$ m
Mesh size	4 m
Number of cells	$160 \times 80 \times 80$
Ignition curve	circle of radius 35 m with origin at $(x, y) = (300, 160)$ m
Constant initial horizontal wind	6 m/s

TABLE 4.II. Parameter values used by the coupled model.

horizontal and vertical mesh sizes are both 4 m which means that the domain is discretized with $160 \times 80 \times 80$ cells. The ignition fireline is a circle of radius 35 m is centered at $(x, y) = (300, 160)$. The rate of spread without wind is $R_0 = 0.5$ m/s. The pictures in this section show the simulations with the coupled model for the parameter $Q = 1500$.

4.5.1. Hill

The hill topography is the base function $b(x)$ from which the other topographies are computed. Figure 4.15 shows the evolution of the fireline on the hill topography. This surface has no variation in the y direction. The projected shape of the fireline is ignited as a circle.

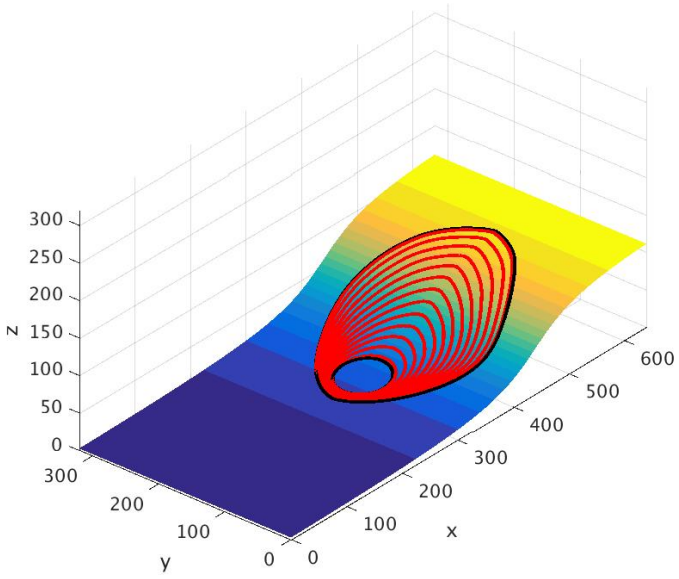

FIGURE 4.15. Fireline spread over the hill topography.

Figure 4.16 shows that as the fire spreads, the shape progressively becomes an ellipse and later an oval. The fire intensity increases with time at the head fire and at $t = 62$ s, a converging zone is clearly visible.

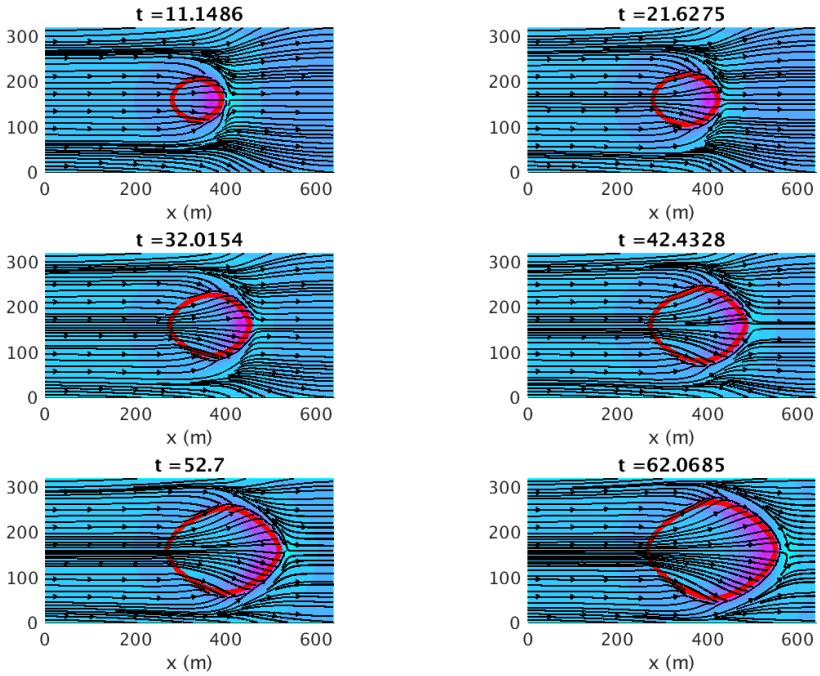

FIGURE 4.16. Fireline (red), streamlines and velocity magnitude at distance $d_{\mathbf{u}-h} = 16$ m above the surface of the hill topography. The magenta and cyan colors indicate high and low wind magnitudes respectively.

Figure 4.17 and 4.18 show a slice of the streamlines in the $y = 160$ and $x = 400$ planes respectively. The circulation motion becomes clearly visible in Figure 4.18.

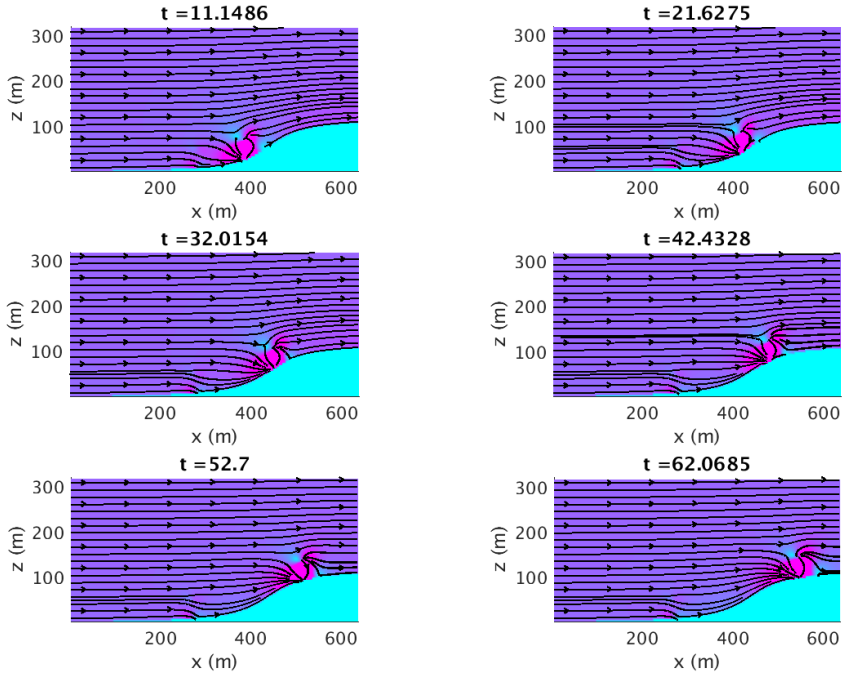

FIGURE 4.17. Fireline, streamlines and velocity magnitude in the $y = 160$ plane for the hill topography. The magenta and cyan colors indicate high and low wind magnitudes respectively.

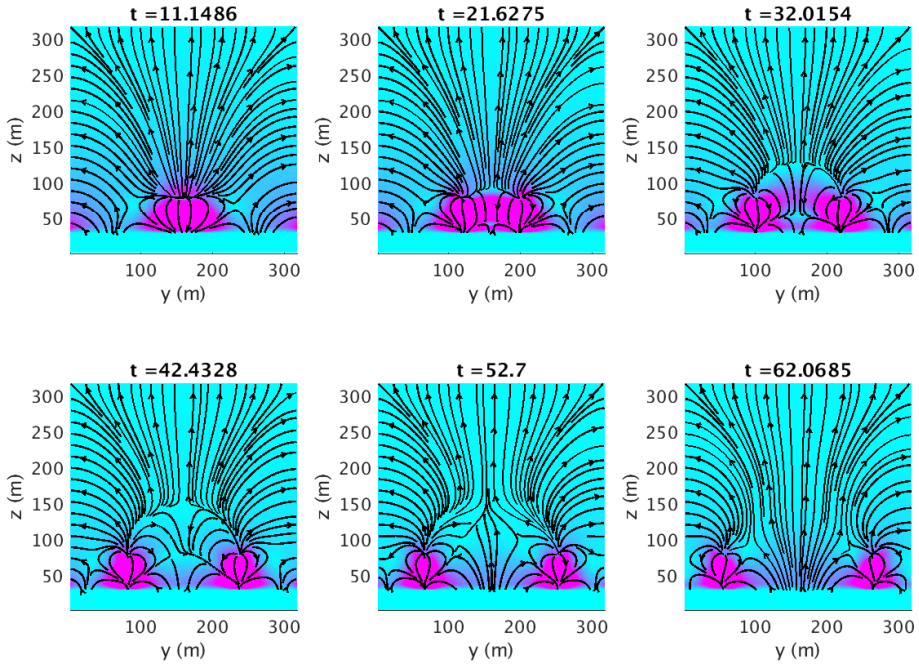

FIGURE 4.18. Fireline, streamlines and velocity magnitude in the $x = 400$ plane for the hill topography. The magenta and cyan colors indicate high and low wind magnitudes respectively.

Figure 4.19 presents six snapshots of the fireline generated with four values of Q. When $Q = 0$, there is no coupling. The delta sink-source pair vanishes since its amplitude is zero. This case is depicted by the blue curve that remains an ellipse at all times. From the previous subsection, it is known that an increase in the value of Q leads to a higher rate of spread. This increase is clearly visible in the downwind part of the fireline. The backward rate of spread does not change much when Q is increased.

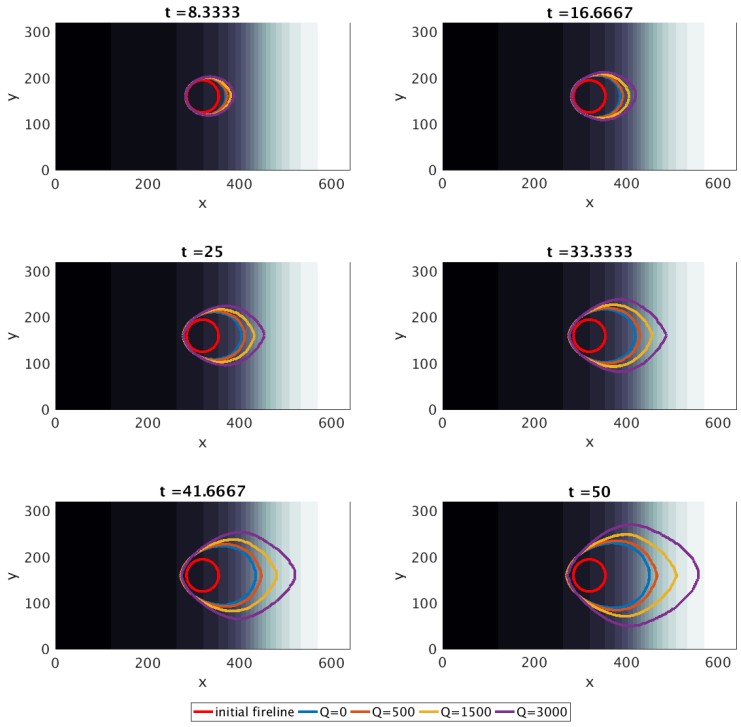

FIGURE 4.19. Fireline over the hill topography (black and white elevation map) at 6 different times for $Q = 0$ (no coupling) and $Q = 500, 1500, 3000$ (coupled model).

Another consequence of an increased Q value is the pointed shape appearing at the head fire. This is different from the results in Figure 4.11 where a teardrop shape was observed. The topography slope explains this change in the fire shape. As the fire spreads over an upward slope, its rate of spread increases, thus increasing the fire induced wind velocity. The fire feedback in the wind flow accentuates the effects of the terrain geometry.

4.5.2. Canyon

The canyon topography is similar to the hill geometry. The region for $x > 300$ m is exactly the same. The region comprised between $x = 0$ and $x = 300$ is constructed in a symmetric manner. The main factor affecting the spread in this case will be the background wind field which is modified by this symmetric part of the topography. Figure 4.20-4.24 show the topography change in the left part of the domain does not have an impact on the fireline spread.

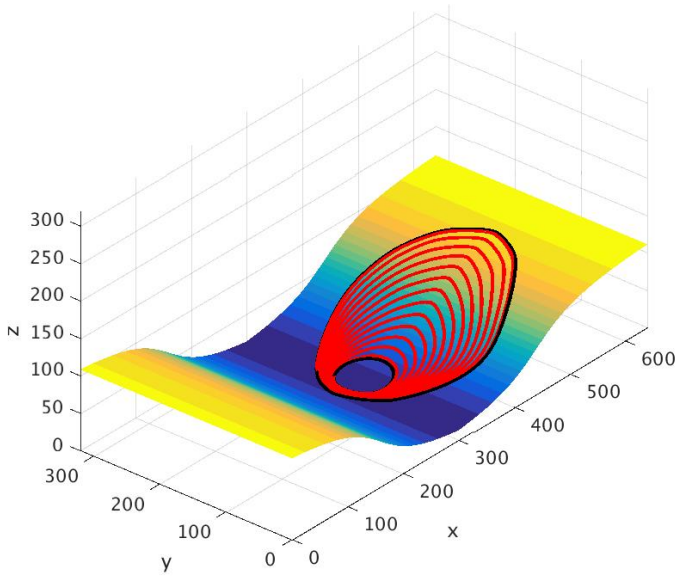

FIGURE 4.20. Fireline spread over the canyon topography.

The streamlines, particularly in Figure 4.21, are different from those in the hill case. There is a change in the background wind field but only near the domain boundaries. Since it is far from the fireline, it does not affect the fire rate of spread. The canyon geometry would only affect the backward rate of spread which is too low in magnitude to be notified.

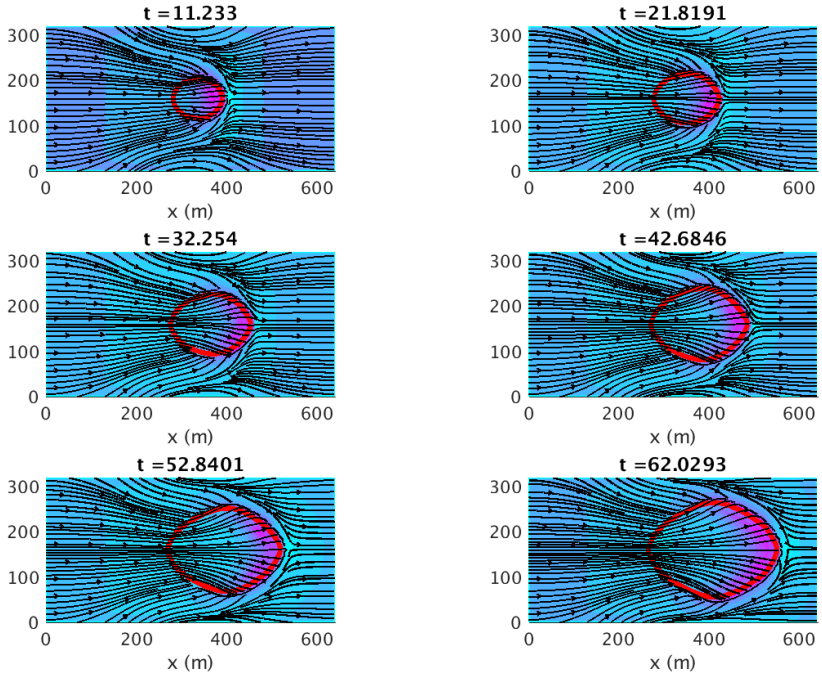

FIGURE 4.21. Fireline (red), streamlines and velocity magnitude at distance $d_{\mathbf{u}-h}$ = 16 m above the surface of the canyon topography. The magenta and cyan colors indicate high and low wind magnitudes respectively.

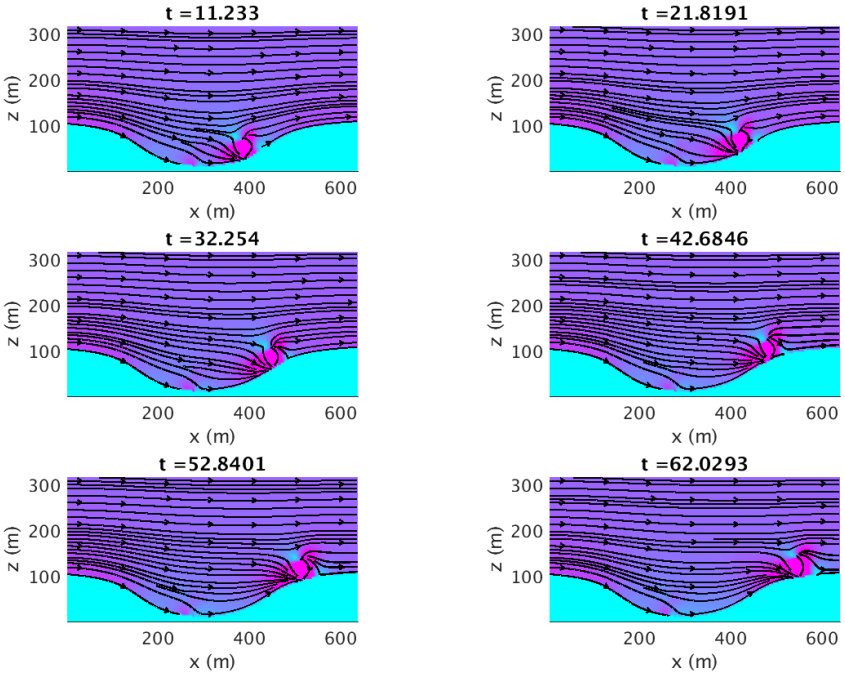

FIGURE 4.22. Fireline, streamlines and velocity magnitude in the $y = 160$ plane for the canyon topography. The magenta and cyan colors indicate high and low wind magnitudes respectively.

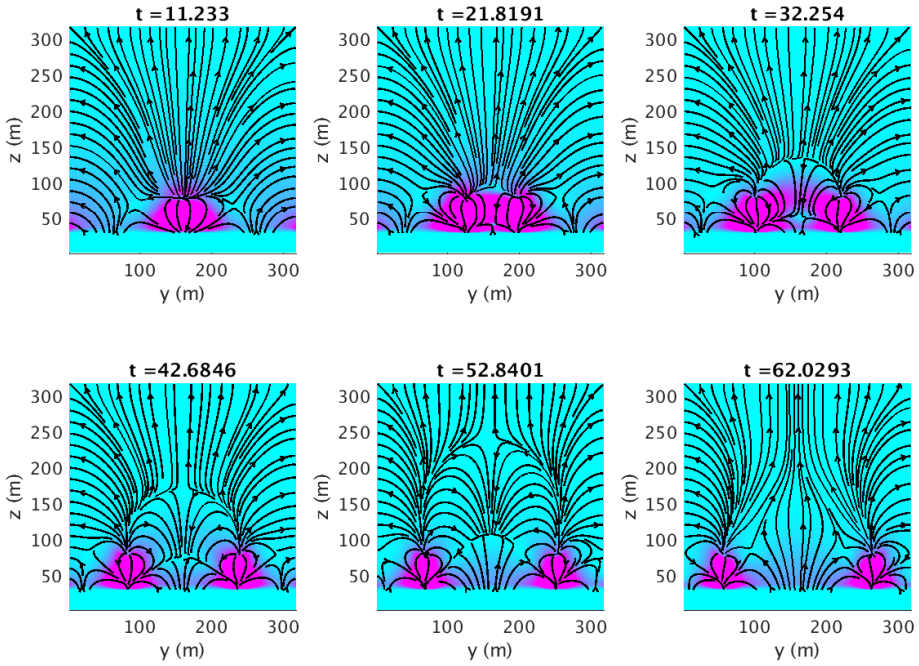

FIGURE 4.23. Fireline, streamlines and velocity magnitude in the $x = 400$ plane for the canyon topography. The magenta and cyan colors indicate high and low wind magnitudes respectively.

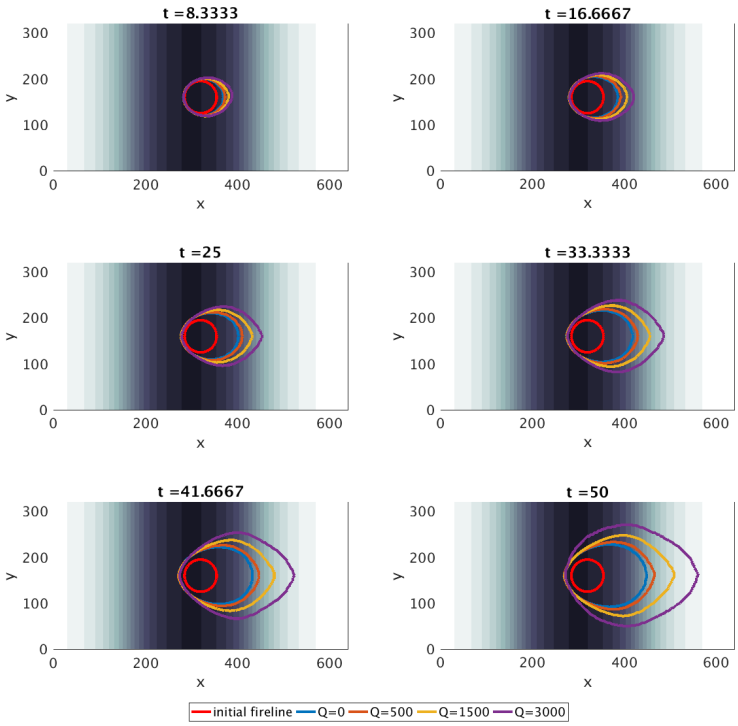

FIGURE 4.24. Fireline over the canyon topography (black and white elevation map) at 6 different times for $Q = 0$ (no coupling) and $Q = 500, 1500, 3000$ (coupled model).

4.5.3. Upcan

The upcan topography adds some variation in the y direction of the hill topography. The slope along the $y = 160$ m axis stays the same, but the elevation is higher on the sides. The upper region of the topography shown in Figure 4.25 looks like a saddle. Such geometric feature lead to a funneling effect in the wind flow. The background wind velocity field converges towards the middle horizontal axis of the domain even if the slope increases on the side.

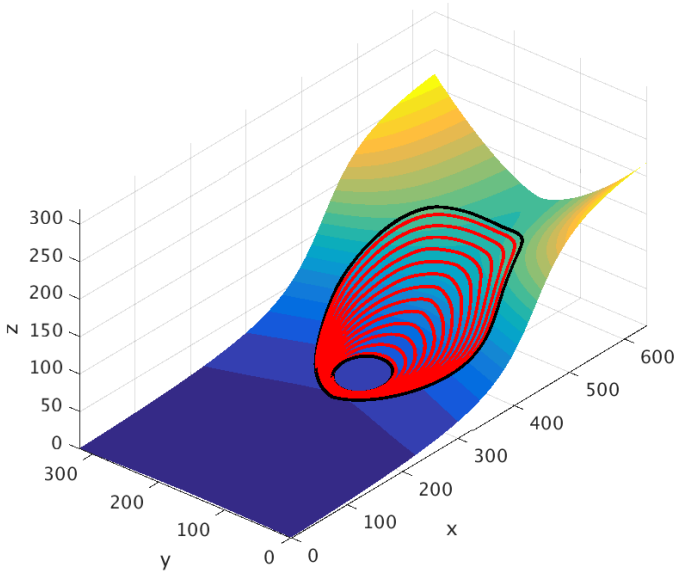

FIGURE 4.25. Fireline spread over the upcan topography.

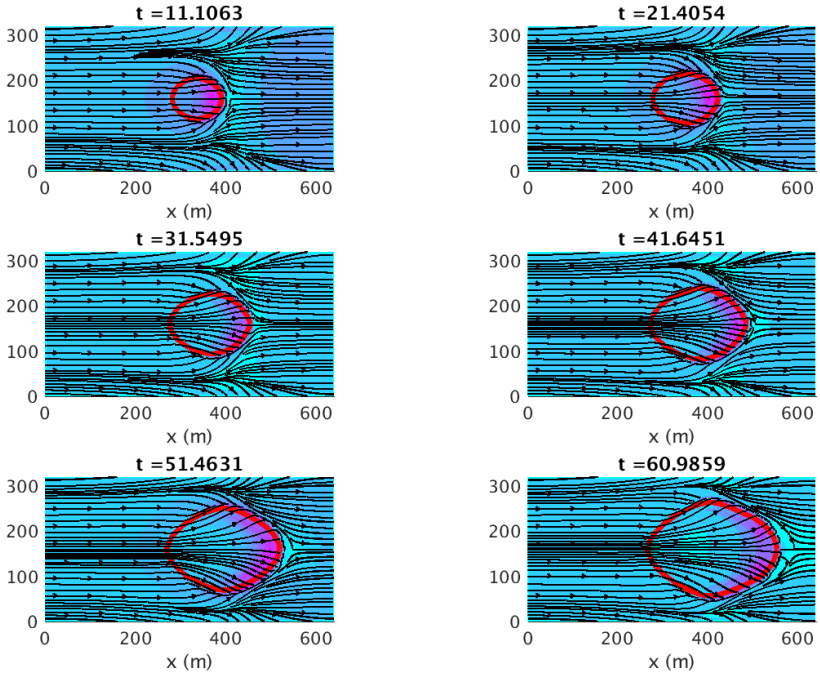

FIGURE 4.26. Fireline (red), streamlines and velocity magnitude at distance $d_{\mathbf{u}-h} = 16$ m above the surface of the upcan topography. The magenta and cyan colors indicate high and low wind magnitudes respectively.

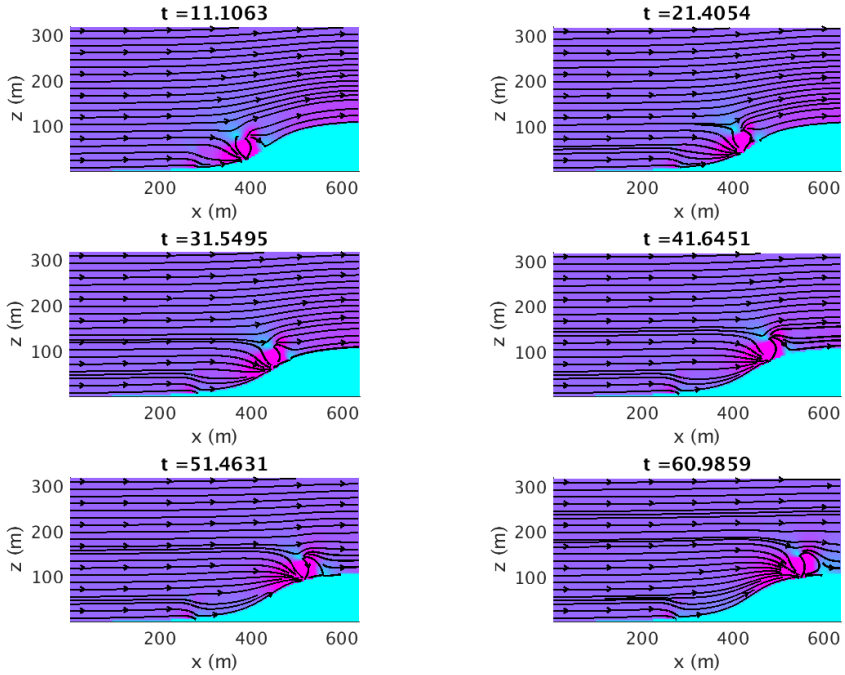

FIGURE 4.27. Fireline, streamlines and velocity magnitude in the $y = 160$ plane for the upcan topography. The magenta and cyan colors indicate high and low wind magnitudes respectively.

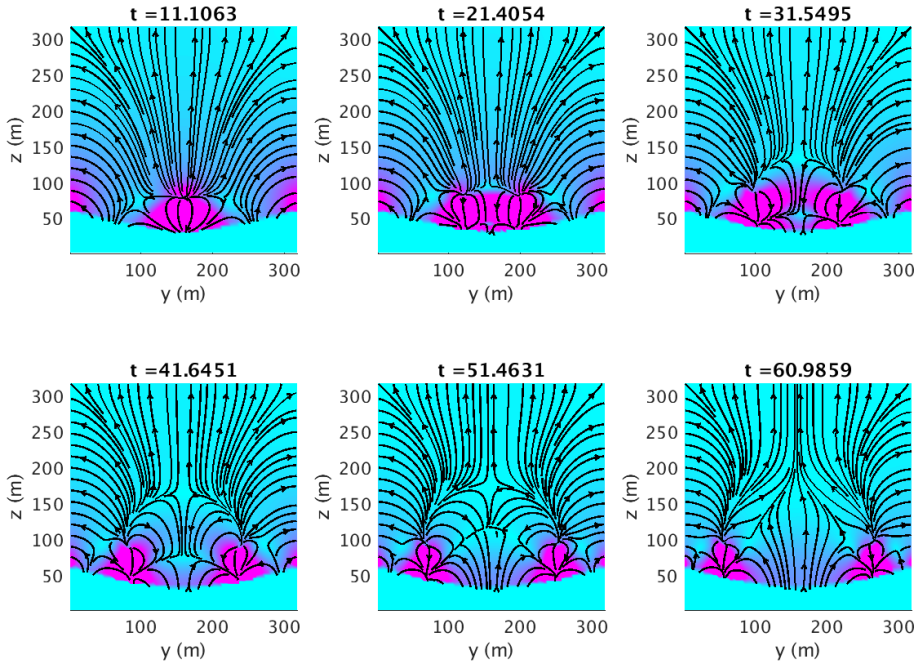

FIGURE 4.28. Fireline, streamlines and velocity magnitude in the $x = 400$ plane for the upcan topography. The magenta and cyan colors indicate high and low wind magnitudes respectively.

When compared to the hill and canyon topographies, Figure 4.29 shows that the fireline in the uncoupled case ($Q = 0$) does not have the oval shape. The head fire already has a convergent structure due to the funneling effect of the background wind field. This feature is amplified when the fire intensity parameter Q increases.

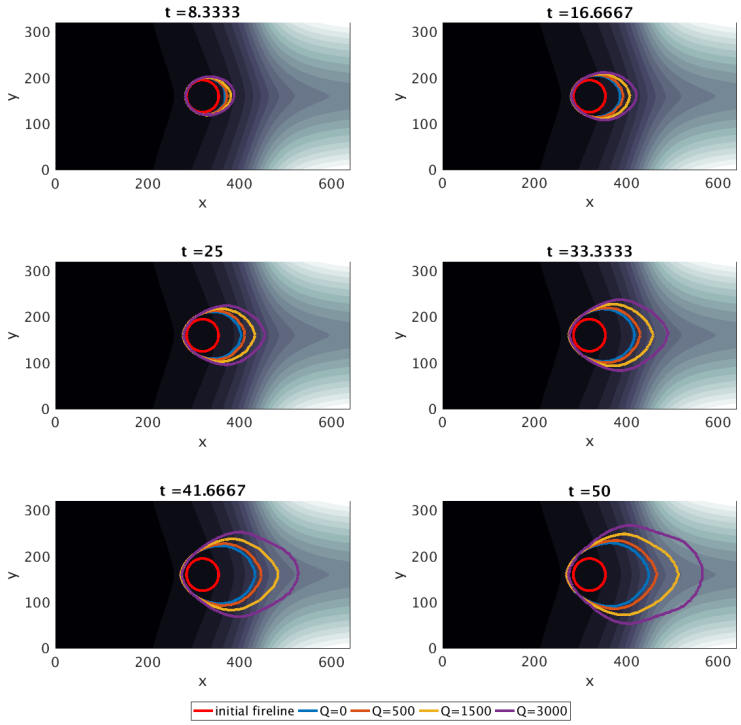

FIGURE 4.29. Fireline over the upcan topography (black and white elevation map) at 6 different times for $Q = 0$ (no coupling) and $Q = 500, 1500, 3000$ (coupled model).

4.5.4. Ridge

The ridge topography is again a modification of the hill topography with an elevation in the center of the upslope section. This creates a ridge along the $y = 160$ m line. This topography is defined with the negative modification previously used by the upcan. Rather than being carved out like the upcan, the topography has a crest. This ridge has a great impact on the fire spread. Figure 4.30 shows the fireline evolution on the ridge in the coupled case ($Q = 1500$). The most notable feature is the convergence in the head zone leading to a sharp tip. This tip is completely absent when there is no fire feedback ($Q = 0$). Figure 4.34 shows that in this case, the fireline shape is a double ellipse, which can be represented by two semi-ellipses. As soon as the feedback is enabled, even the weakest case ($Q = 500$), the tip appears. This is clearly seen at $t = 50$ s in the orange curve.

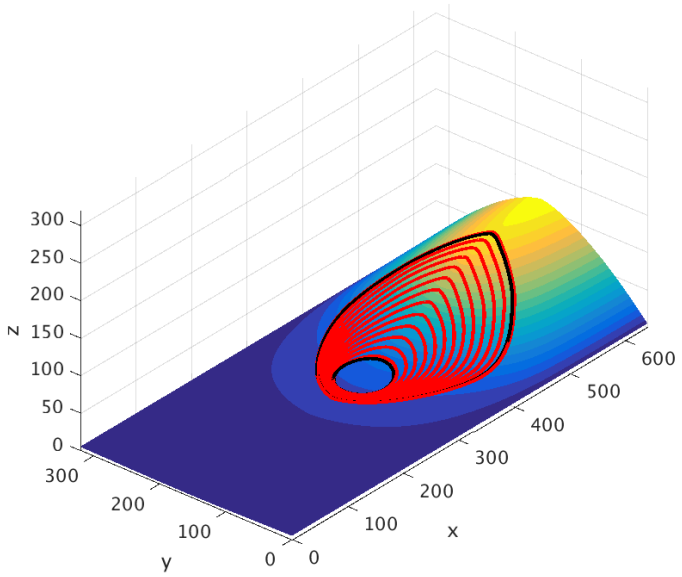

FIGURE 4.30. Fireline spread over the ridge topography.

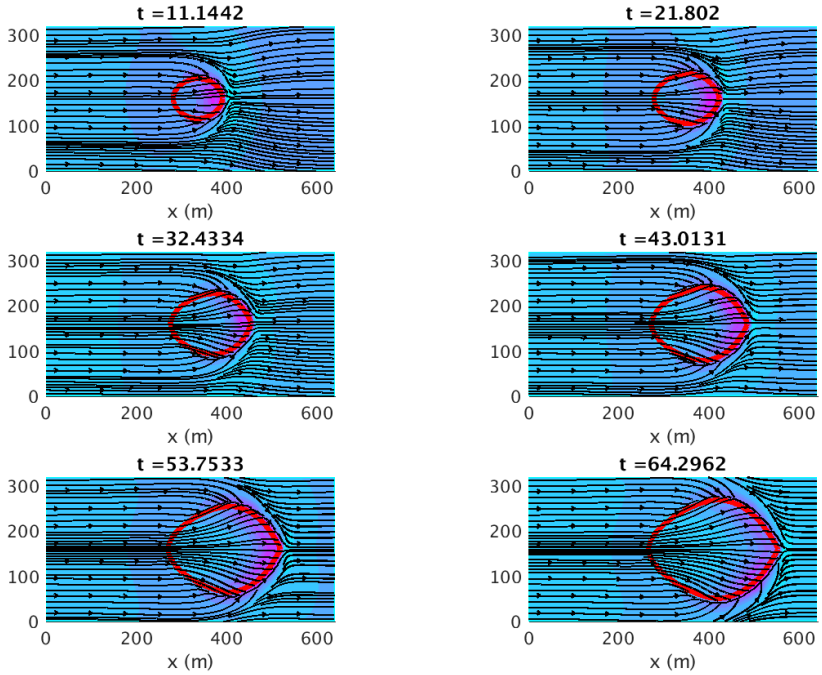

FIGURE 4.31. Fireline (red), streamlines and velocity magnitude at distance $d_{\mathbf{u}-h} = 16$ m above the surface of the ridge topography. The magenta and cyan colors indicate high and low wind magnitudes respectively.

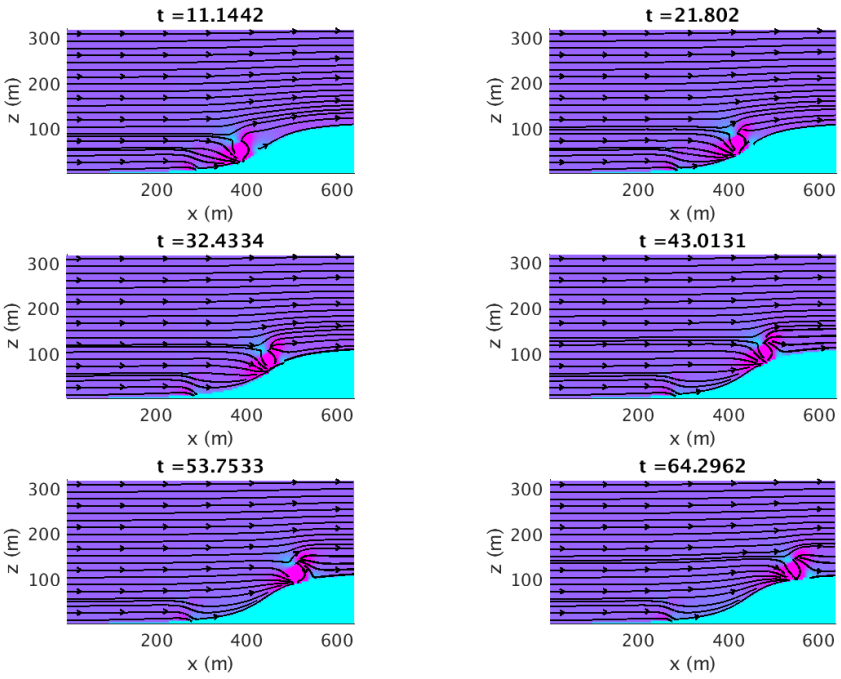

FIGURE 4.32. Fireline, streamlines and velocity magnitude in the $y = 160$ plane for the ridge topography. The magenta and cyan colors indicate high and low wind magnitudes respectively.

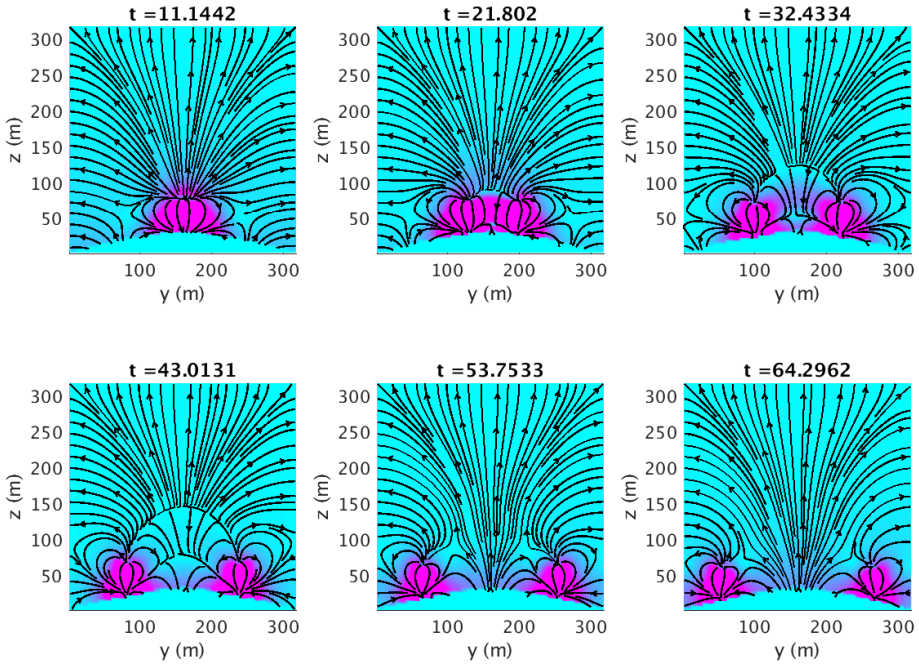

FIGURE 4.33. Fireline, streamlines and velocity magnitude in the $x = 400$ plane for the ridge topography. The magenta and cyan colors indicate high and low wind magnitudes respectively.

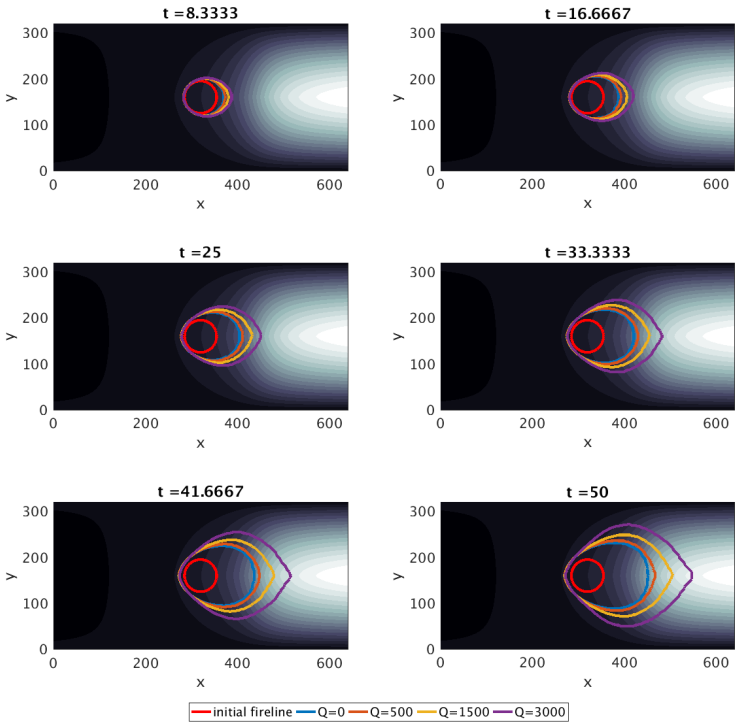

FIGURE 4.34. Fireline over the ridge topography (black and white elevation map) at 6 different times for $Q = 0$ (no coupling) and $Q = 500, 1500, 3000$ (coupled model).

4.5.5. Discussion

The streamlines in the figures above show that the coupled model can generate a wind flow tangent to the terrain and sensitive to the geometrical features of the topography. The fire feedback on the wind velocity field achieve a good reproduction of the important local features of fire plumes. The wind streamlines show a well-defined circulation motion, a rear downdraft and a wind inflow near the fireline.

The sink-source pair can also induce convergence zones in the heading zone of the fire. This convergence of the wind flow, observed for all topographies, causes the pointed shape of the burned region. This narrow head shape was not observed for the simulations on the horizontal flat topography. A similar observation was made by Linn *et al.* [**62**] from their simulations with Firetec: "*the fire head shape is more pointed on the upslope topography than on the flat ground*".

The shape of the burned areas is sensitive to the combined effect of the topography geometry and the intensity parameter Q. When $Q = 3000$, these shapes are very different for the hill, upcan and ridge topographies. An increase in the value of Q accelerates the propagation of the fireline and changes the fire shape in a significant manner.

4.6. Comparison with Firetec and Forefire

The coupled model is compared with two other fire-atmosphere models: Firetec [**58**], a self-determining physical model and Forefire [**42**], a fire model coupled with the mesoscale atmospheric model MesoNH. The simulations of the fire spread are performed on the same idealized topographies as in section 4.5 with a background wind of 6 m/s. The comparison is based on the propagation distance of the head fire in the x direction as a function of time. These diagnostic tests were first used for Firetec in [**61**]. The distance is computed between the greater value of the x coordinate of the head fire position with the initial position. This corresponds to the horizontal distance, which facilitates the comparison of the propagation between each topography.

Since Firetec and Forefire models are the results of two different modeling approaches, the quantity and values of the parameters and variables for calibration of both models are not the same. The scales change from one model to another, which means a different mesh size must be used for each model. Table 4.III presents the different configurations for the simulations with Firetec and Forefire. The differences between both simulation set-ups are more pronounced for the mesh size and fuel type. Firetec used two kinds of fuel over two distinct regions separated by a 45° line. These fuels were included in the model as discretized fuel elements. Since

Characteristics	Firetec	Forefire
Domain	$640 \times 320 \times \sim 700$ m	$640 \times 320 \times 500$ m
Horizontal mesh size	2 m	16 m
Vertical mesh size	~ 1.5 m near surface	20 m in average
Number of cells	$320 \times 160 \times \sim 350$	$40 \times 20 \times 25$
Time step	0.01 s	–
Ignition line	60×8 m at $x = 300$ m	60×8 m at $x = 320$ m
Constant initial horizontal wind	6 m/s and 12 m/s	6 m/s
R_0	–	0.1 m/s
Fuel type	Tall grass and Ponderosa pines	Average homogeneous dry fuel of 7 kg/m^2

TABLE 4.III. Parameter values used for the simulations with Firetec and Forefire.

Forefire does not require a fuel map at such a fine scale, a homogeneous fuel covered the whole domain and its average value was computed from the fuel types used by Firetec. The boundary conditions were not given explicitly for Firetec, but open boundary conditions were fixed by Forefire. In order to compare the simulations of the coupled model with those of Firetec and Forefire, the values for the grid are the same as in Table 4.II.

In the simulations with Firetec, the fireline is ignited as a line segment centered at $x = 300$ and $y = 16$. The length of the segment in the y direction is 60 m and its width in the x direction is 8 m. The ignition line used by Firetec is under-resolved for the coupled model. The fireline curve must be sufficiently spread apart so the sink-source pair can be correctly defined. For the simulations below, the fireline is ignited as a rectangle with smoothed corners and of sides 60 m long and 30 m wide. The right edge of the rectangle is aligned with the $x = 300$ axis like the line segment used by Firetec.

Comparison between models can be challenging. The coupled model requires some calibration before the simulations can be run. Figure 4.35 shows the propagation distance on the canyon, ridge and flat topographies with Forefire and Firetec. The latter is fully coupled so there is only one simulation for each case. Simulations with Forefire are shown when the fire and atmosphere models are coupled and uncoupled. From this picture, the authors using Forefire could only conclude that even with the coupling on, their coupled model would underestimate the propagation distances computed by Firetec which were considered as the reference target. For unexplained reasons, the propagation distance saturates in the uncoupled simulations of Forefire.

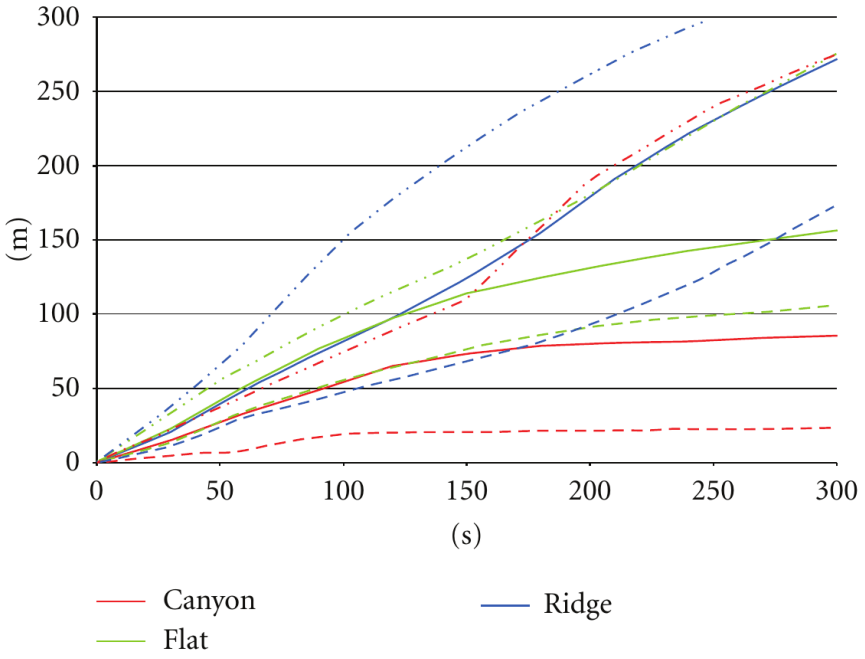

FIGURE 4.35. Propagation distance of the fire front as a function of time for the canyon, ridge and flat topographies for Firetec (dotted-dashed lines) and Forefire for the coupled (plain lines) and uncoupled (dashed lines) cases. (Source: Forefire [**42**])

For the sake of simplifying the analysis, a different approach is taken. The fire-atmosphere model was calibrated first to match the results of Firetec on the flat topography, when there is no fire feedback into the wind flow. This means the intensity parameter is $Q = 0$. The calibration is done such that the fire head and lateral propagation distances match Firetec results for the first 50 s. This is achieved by multiplying the propagation speeds parameters a, b and c by an appropriate factor. Once the model is calibrated for the flat topography, the calibration is kept for the simulations on the other surfaces. This process allows to check the impact of the terrain geometry on the propagation distance.

The model is completely re-calibrated in the same manner before launching simulations for the coupled case ($Q = 7000$). The reason is to be able to efficiently analyze the effect of the fire feedback on the fire spread compared to the simulations computed without the feedback. The factors used for the calibrations are shown in Table 4.IV.

With the graph of Figure 4.36 combining the results for the five idealized topographies, Linn *et al.* [**61**] using Firetec noted that the propagation distances according topographies could be separated into two groups: a first consisting of the hill, the upcan and the ridge, and a second gathering the canyon and the flat terrain. The

Q	a & c	b
0	6/13	9/65
7000	3/10	3/20

TABLE 4.IV. Multiplying factors for a, b and c propagation parameters in the coupled and uncoupled cases.

propagation distance for a fixed period of time is greater for the first group than the second. The analysis will answer the following questions:

(1) Do the propagation distances computed with the coupled model recover the two collections found by Firetec?

(2) What is the effect of the non-trivial topographies on the fire spread with the coupled and uncoupled model?

(3) For the same topography, how does the coupling affect the fire shape?

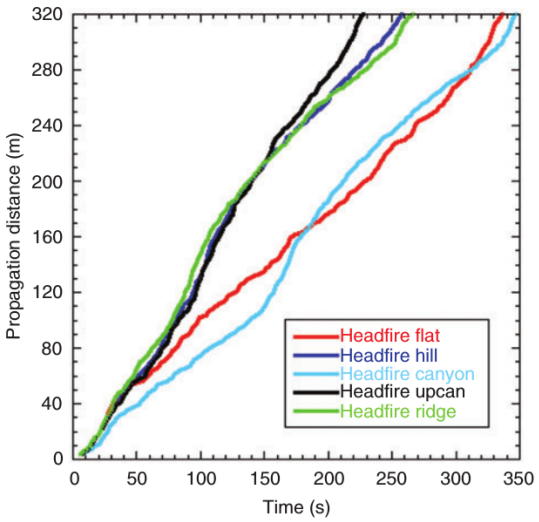

FIGURE 4.36. Propagation distance of the fire front as a function of time for five idealized topographies with Firetec. (Source: Linn *et al.* [**61**])

The propagation distance is shown in Figure 4.37 when there is no feedback ($Q = 0$) from the fireline into the wind flow. The curve for the flat topography is straight, which means the rate of spread is constant in time. This is not surprising since there is no perturbation coming either from the wind or the terrain geometry. Looking for the four non-trivial topographies, the distance as a function of time is not a straight line. There is a deflection around 70 s and then the curves become parallel to the flat curve about 200 s. The four curves almost overlap. Remember that

the slope along the centerline of the domain is the same for the four idealized topographies. The uncoupled model does not seem to change the propagation distance in any obvious way.

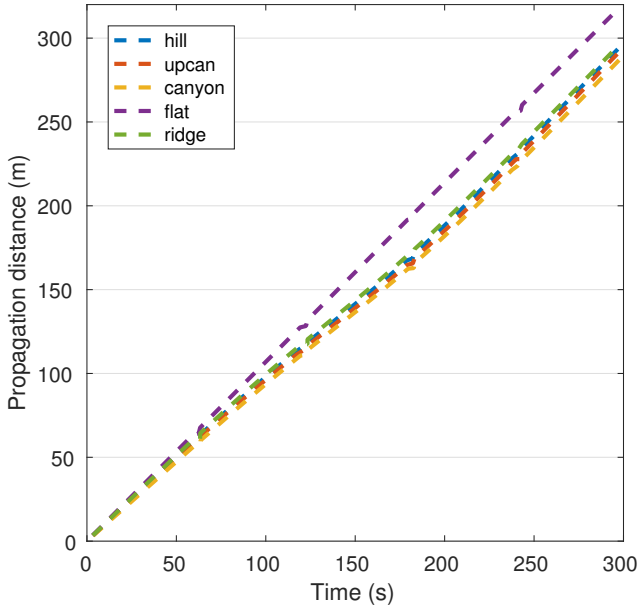

FIGURE 4.37. Propagation distance of the head fire as a function of time for five topographies with the uncoupled model.

Figure 4.38 shows the propagation distance when the coupling between the fire and atmosphere models is enabled ($Q = 7000$). The results show a totally different situation from Figure 4.37. The horizontal propagation distances are about the same for the first 120 s. Then the curve for the flat surface goes over all other curves before being caught up by the upcan curve around 240 s. There is no significant difference for the propagation distance on the hill and canyon topographies. The coupling changes the wind flow on these topographies in the same manner. Finally, the propagation distance for the ridge ends under all other curves.

The curves of the propagation distance for the coupled model show more fluctuations than in the simulations without the fire feedback. The rate of spread has more sensitivity to the topography in the coupled simulations. The fluctuations in the curves in Figure 4.38 do not form the two groupings observed by the Linn *et al.* In both cases, the fire spreads the fastest on the upcan. The major difference with Firetec is for the ridge and canyon cases. The distance on the canyon shows a different behavior from the distance on the hill in Firetec results. The explanation comes from the effect of the geometry of the terrain far behind the head fire on the wind flow. Firetec uses a full physics atmospheric model which can capture complicated wind

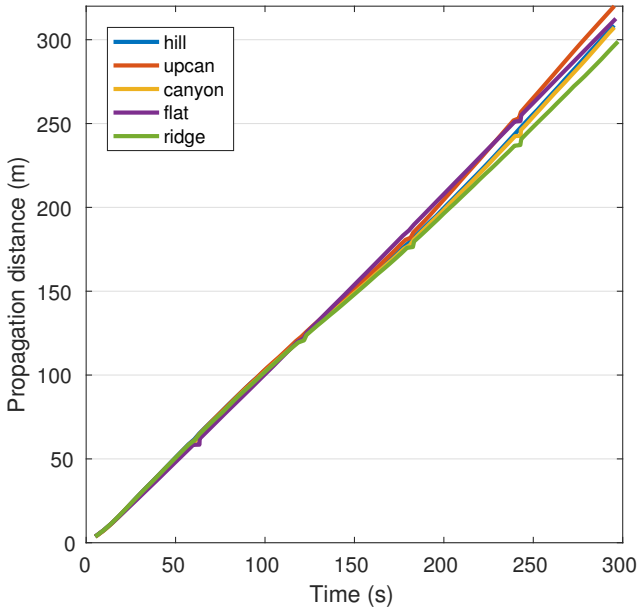

FIGURE 4.38. Propagation distance of the head fire as a function of time for five topographies with the coupled model.

motion that can be triggered by the terrain surface such as the cavity of the canyon. The almost mass consistent model cannot capture such features. This is why there is no difference between the hill and canyon in our simulations. As for the ridge, the coupling combined with the topography slope induce a strong convergence at the head fire. This slows down significantly the fire spread, as illustrated in the right picture of Figure 4.39.

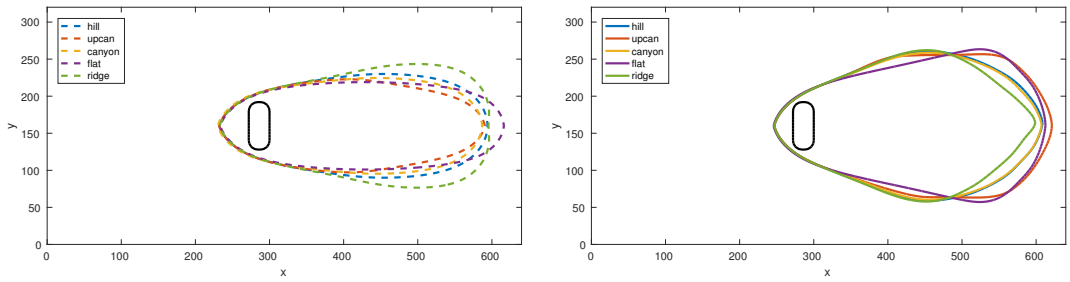

FIGURE 4.39. Propagation distance of the fire front as a function of time for five topographies with the coupled (**right**) and uncoupled (**left**) model.

The contours at time 300 s are shown for the coupled and uncoupled simulations. When there is no coupling, the fireline shape grows as an ellipse or remains close to it as for the upcan and flat cases. The coupling creates the pointed shape of

the burned region and increases the flanking. Figure 4.40 shows the effect of the coupling on each individual topography. Recall that the simulations for the coupled and uncoupled cases were calibrated separately in different manners for the flat surface. Section 4.5 has shown that enabling the coupling accelerates the fire rate of spread. The distinct calibration explains why this phenomenon is not present in Figure 4.40, especially for the flat case.

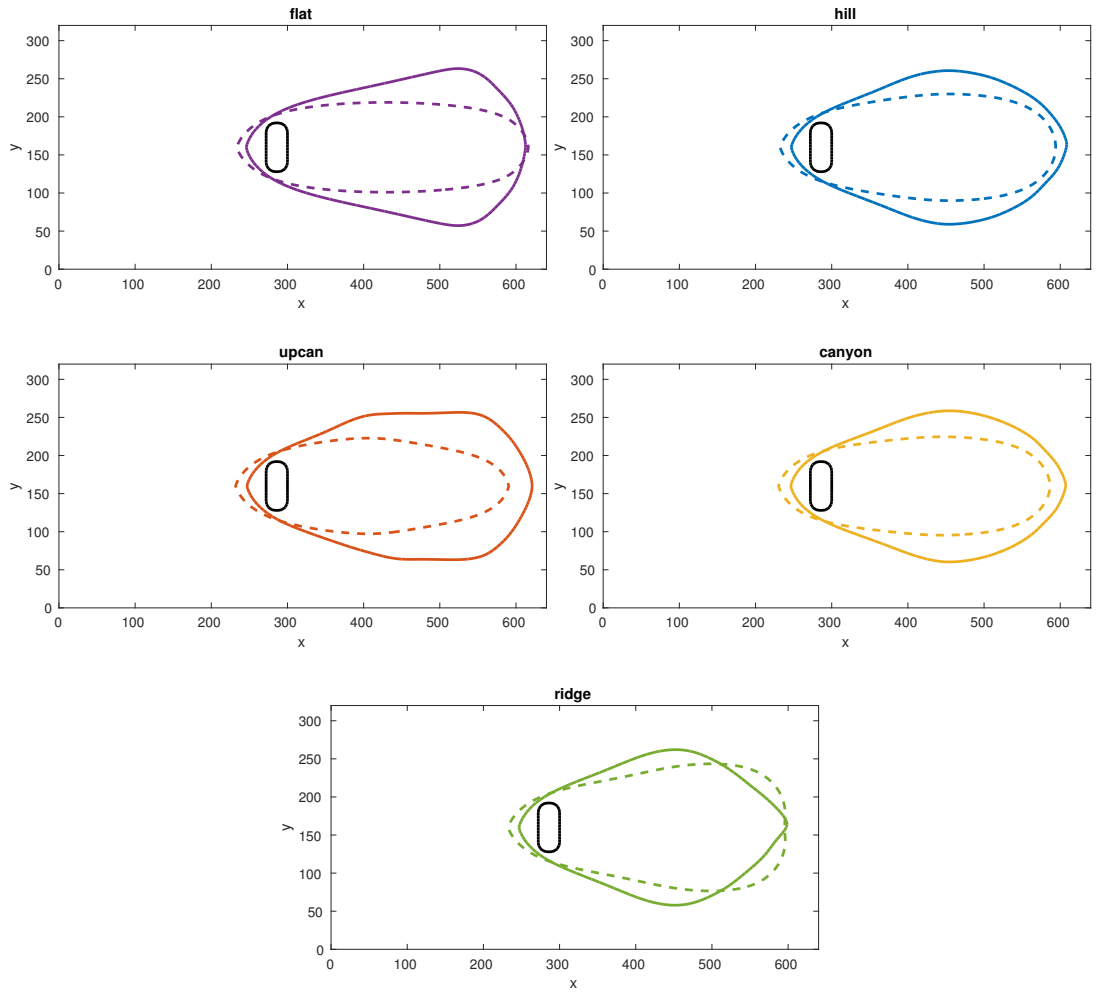

FIGURE 4.40. Propagation distance of the fire front as a function of time for five topographies with the coupled (plain lines) and uncoupled (dashed lines) model.

In all five cases, the coupling slows down the backfire propagation in the upwind direction. This behavior is expected since the induced wind flow contributing to the fire rate of spread is in the opposite direction of the background wind velocity field. It is already well documented that the shape of the topography affects the fire spread. These simulations clearly show that the fire feedback can also have a great impact on the fire propagation. It can emphasize the prominent features of

the shape in the uncoupled model, as for the hill, canyon and upcan cases. It can also radically alter the shape of the burned region. This is seen on for flat topography, where flanking is induced by the fire feedback and for the ridge topography, where the head zone becomes sharp rather than being flat. From the pictures in Figure 4.40, the lateral spread seems to be deeply affected by the fire feedback. Figures 4.41 and 4.42 show the maximal horizontal lateral extent of the fireline as a function of time for the five topographies in the uncoupled and coupled cases respectively.

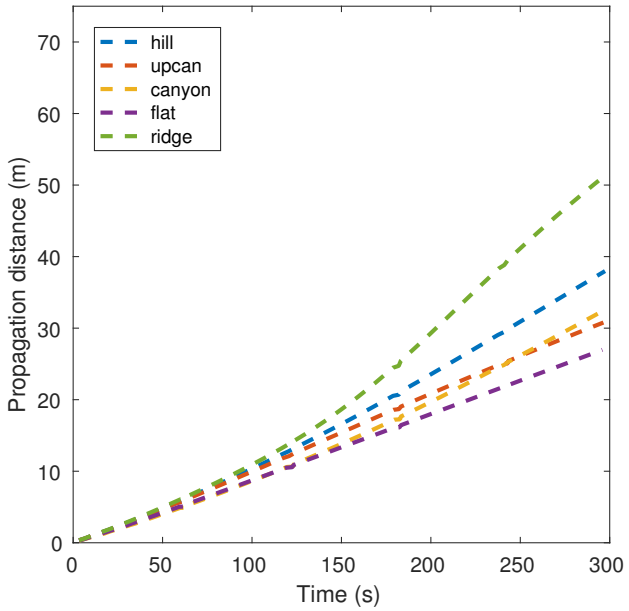

FIGURE 4.41. Maximal lateral extent of the fire as a function of time for five topographies with the uncoupled model.

For the uncoupled case, there is already more significant difference between the flat and the non-trivial topographies. The most striking observation can be made on the hill and canyon cases. They do not overlap as it was the case for the propagation distance in Figures 4.37 and 4.38. The lateral spread is highest for the ridge surface in the uncoupled case. This is completely different for the coupled simulations. In this case, the fire has a wider lateral spread on the flat topography than any other. At 300 s, the difference in the maximal lateral spread between the non-trivial topographies is less than the uncoupled case. There are fluctuations in the curves of Figure 4.38 between 50 s and 200 s that are not captured by the uncoupled model.

Finally, the coupled model brings variability in the simulations due to the increased sensitivity to the geometric features of topography. This variability is not as strong as the results obtained by a full Navier-Stokes model like Firetec. The head propagation distances were close to each other but not for the flat topography. The

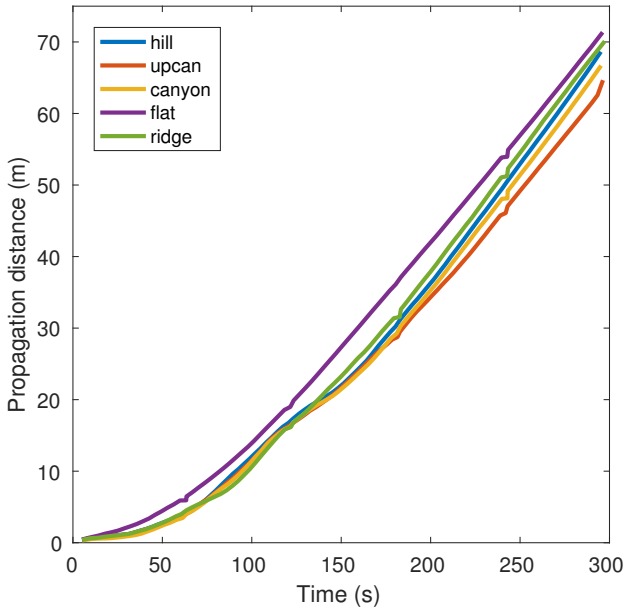

FIGURE 4.42. Maximal lateral extent of the fire as a function of time for five topographies with the coupled model.

non-trivial topographies are defined in such a way that the slope along the centerline is identical for all of them. The relative similarity in the results can be explained by the coupled model being affected only by local perturbations. The global geometry of the terrain, away from the fireline along the centerline, has less direct effect on the fire spread.

The simulations with the coupled model show that the shape and lateral propagation were highly influenced by the fire induced wind velocity field and the topography. In the non-coupled model, the fire shapes were almost perfect ellipses for any topography. The geometry of the topographies has a stronger influence on the fire spread with the coupled model. For a given topography, the coupling alters the fire shape dramatically. It increases its lateral propagation speed due to a flanking effect and creates the characteristic narrow tip in the head fire shape.

4.7. CONCLUSIONS

A model is useful as a forecasting tool if it can generate simulated scenarios quickly. A novel coupled fire-atmosphere model has been designed for the propagation of forest fires. The focus was placed on developing a simple atmosphere model that can take into account the fire heat release without compromising its computational efficiency. The innovative features are: a quasi mass-consistent model for the wind

flow based on a projection method, a fire feedback given as sink-source pair represented by delta functions, the amplitude of the fire heat release computed from the fire intensity, an accurate representation of the topography in the computational domain and a dimensionless number Q quantifying the feedback onto the atmosphere. These features were presented in detail in the first part of the article. The key idea of the coupling is to add a local perturbation in the wind flow which is hardly achieved by mesoscale atmospheric models. The simplicity of the coupled model was demonstrated in the description of the numerical implementation and its algorithm.

A three-stage study of the model was conducted. The regimes of propagation of the 3D model on flat inclined topographies were compared with the results for the 2D model documented in [**82**]. It was shown that the contribution of the induced wind velocity field on the fire rate of spread has the same dependence on the parameter Q and the slope angle α. The difference in the magnitude of the rate of spread was explained by the non-trivial behavior of the spread occurring in the third dimension.

A qualitative analysis of the spread on idealized topographies showed that the sink-source pair reproduces local features of a flow induced by a fire. The local perturbation increases the effect of the topography on the fire spread. The coupling enables the reproduction of particular burned shapes, such as the teardrop on the flat topography and the narrow converging tip on the upslope terrain. The cause of the formation of these shapes was previously associated with fuel bed heterogeneity. The coupled model showed that it is an intrinsic feature of the fire feedback and its local perturbation on the wind flow.

Finally, a study of the coupled influence of wind and topography was conducted with the coupled model. The simulations were calibrated in order to match the propagation distance obtained with Firetec. The effect of the coupling and the topography was compared to the uncoupled case. The results have shown that the upcan topography has the most impact on the propagation distance like it was the case with Firetec. The difference between the hill and canyon topography in the upwind section of the domain did not change the propagation distance in a quantitative manner. The major difference was observed with the ridge for which the propagation distance was underestimated by the coupled model. The coupling was able to reproduce the convergence in the head fire that was absent in the uncoupled simulations. The simulations showed the coupled model adds variability in the propagation distance, especially for the lateral propagation.

This coupled approach is promising for forecasting wildfire spread. It is worth studying the effect of other parameters on the rate of spread and the local fire induced wind flow. A subsequent study, similar to the ones conducted with Firetec [**62**, **80**], could focus on the model sensitivity to the heterogeneity of the fuel distribution on the fire spread.

CONCLUSION

L'objectif principal de cette thèse était de développer un nouveau modèle couplé dans le but de prévoir la propagation des feux de forêt. L'idée maîtresse est de générer numériquement un écoulement atmosphérique qui est perturbé localement par la chaleur émise par le feu. Cette perturbation doit reproduire les principales caractéristiques d'un écoulement induit par le feu. Les résultats principaux de la thèse résident en deux parties. La première est la composante de modélisation, avec l'élaboration de la physique du modèle couplé et son usage dans des simulations. La deuxième est de nature numérique avec le développement d'une nouvelle technique de régularisation pour les fonctions delta supportées sur des variétés de codimension 2.

NOUVELLE APPROCHE COUPLÉE

L'élaboration du modèle feu-atmosphère a été présentée en détail dans le chapitre 3. Le modèle pour le feu a été établi à partir du modèle de propagation de Richards. Une technique numérique développée par Desfossés Foucault [**31**] permet d'utiliser ce modèle pour suivre l'évolution de l'interface du feu. Le modèle atmosphérique est une généralisation du modèle strictement incompressible pour le vent décrit dans [**81**]. Il est composé d'une seule contrainte de divergence pour le champ de vitesse du vent avec un terme source. Cette équation est dérivée d'une approximation à faible nombre de Mach. Cette propriété du modèle contraste avec l'approche entreprise par d'autres modèles couplés. Ces modèles, présentés dans la revue de littérature du chapitre 1, ont souvent recourt à un modèle atmosphérique méso-échelle. Le choix de représenter le terme source de l'équation de divergence par une paire source-puits permet de reproduire des effets caractéristiques d'un écoulement induit par le feu tels que la convergence du vent vers l'interface du feu en aval et l'effet de circulation. La source et le puits sont représentés par des fonctions delta pour assurer la cohérence avec la représentation du feu par une interface infiniment mince. L'amplitude locale de la perturbation due à la chaleur émise par le feu sur l'atmosphère est calculée à l'aide de l'intensité du feu telle que

définie par Byram. Une analyse dimensionnelle a permis de déterminer un nouveau nombre sans dimension Q qui traduit la force du couplage entre le feu et l'atmosphère. Une analyse des régimes de propagation pour des cas en deux dimensions a été présentée.

Le chapitre 4 a présenté les détails de l'implémentation numérique du modèle. La méthode numérique pour le modèle atmosphérique est détaillée. Un algorithme décrit le fonctionnement du couplage entre les deux modèles feu et atmosphère dont les codes respectifs communiquent à l'aide d'un «pipeline». Une étude des régimes de propagation avec le modèle couplé a été effectuée afin d'étudier l'effet du vent et de la pente sur la vitesse de propagation dans le modèle. Des simulations réalisées sur des topographies idéalisées ont permis de comparer le modèle physique Firetec. Les résultats ont montré que le modèle couplé augmente la sensibilité de la vitesse de propagation aux changements de topographies et qu'il permet de reproduire certaines formes de propagation observées dans les simulations réalisées par des modèles plus complexes.

Les nouvelles approches numériques et le modèle atmosphérique développés dans le cadre de cette thèse pourront être intégrés aux modèles de prédiction actuels tels que le modèle canadien Prometheus. Ce modèle qui permet de simuler la propagation des feux de forêt en milieu hétérogène est présentement utilisé par les instances gouvernementales du Canada ainsi qu'à l'étranger. Ultimement, ces contributions permettront d'apporter un gain de rapidité et de précision dans les modèles de prédictions. De meilleures décisions pourront alors être prises par les autorités afin de limiter les impacts négatifs des feux de forêt sur la santé publique et la sécurité des individus, ainsi que minimiser les pertes de biens matériels et de ressources naturelles.

Nouvelle technique de régularisation

Une méthode de régularisation pour les fonctions delta a été développée afin d'assigner une amplitude locale au terme source supporté par l'interface du feu. Cette méthode de régularisation combinée à un rééchelonnage de la fonction delta régularisée a été présentée dans le chapitre 2. Les défis principaux de la régularisation découlaient des caractéristiques du modèle couplé. L'objet sur lequel est supportée la fonction delta est une variété de codimension 2. La majorité de la littérature considère seulement le cas de codimension 1. Le domaine de résolution utilise une grille cartésienne dont les volumes de contrôles près du bord inférieur sont irréguliers. La fonction delta se retrouve sur cette frontière plutôt que d'être au centre du domaine. La méthode de régularisation tire avantage de la représentation de l'interface du feu et de la topographie par des fonctions «level set». La méthode

de rééchelonnage utilise la projection de l'interface dans le plan horizontal pour assigner la bonne amplitude de la fonction delta à chaque segment de droite projeté. Cette technique a été validée dans le cas d'un problème elliptique similaire à celui du modèle atmosphérique. La fonction delta était rééchelonnée afin de satisfaire une condition de premier moment. Les tests numériques ont montré que cette propriété assure la convergence des solutions numériques.

FUTURES AVENUES DE RECHERCHE

Plusieurs directions sont envisageables afin de poursuivre la recherche entamée avec ce modèle. Il serait d'abord intéressant d'étudier l'effet de la distribution des combustibles sur la propagation. Le moteur principal de la vitesse de propagation du feu est le vent. Tout comme la pente du terrain, le type de combustible et sa répartition jouent également un grand rôle dans la variabilité de la vitesse de propagation. Par exemple, le modèle permettrait de vérifier si l'hétérogénéité du combustible a le même effet sur la propagation du feu que les petites variations géométriques de la topographie. Cette analyse de la sensibilité du modèle aux petites échelles pourrait être comparée aux travaux sur l'homogénéisation dans la thèse de Desfossés Foucault [**31**].

Une autre possibilité de développement serait d'étudier le modèle dans le contexte d'un vrai feu de forêt. Certains feux de forêt ont bien été recensés et offrent suffisamment de données pour tester des modèles. Les conditions météorologiques observées, les cartes de combustibles et la surface brûlée à de courts intervalles permettent de reproduire des effets empiriques de la propagation avec des modèles numériques. Ce nouveau modèle couplé pourrait être mis à l'épreuve dans un contexte réaliste comme cela a été fait par Coen [**21**] avec CAWFE et Fillipi *et al.* [**42**] avec Forefire.

BIBLIOGRAPHIE

[1] F. Albini. Response of free-burning fires to nonsteady wind. *Combustion Science and Technology*, 29(3-6):225–241, 1982.

[2] F. Albini. PROGRAM BURNUP: A simulation model of the burning of large woody natural fuels. Final Report on Research Grant INT-92754-GR by USFS to Montana State University. *Mechanical Engineering Dept*, 1994.

[3] M. E. Alexander. Calculating and interpreting forest fire intensities. *Canadian Journal of Botany*, 60(10):2185–2185, 1982.

[4] M. E. Alexander and M. G. Cruz. Interdependencies between flame length and fireline intensity in predicting crown fire initiation and crown scorch height. *International Journal of Wildland Fire*, 21(2):95, 2012.

[5] A. A. Ali, O. Blarquez, M. P. Girardin, C. Hély, F. Tinquaut, A. El Guellab, V. Valsecchi, A. Terrier, L. Bremond, A. Genries, et al. Control of the multimillennial wildfire size in boreal North America by spring climatic conditions. *Proceedings of the National Academy of Sciences*, 109(51):20966–20970, 2012.

[6] P. L. Andrews. BEHAVE: fire behavior prediction and fuel modeling system-BURN subsystem, Part 1. 1986.

[7] J. Balbi, F. Morandini, X. Silvani, J. Filippi, and F. Rinieri. A physical model for wildland fires. *Combustion and Flame*, 156(12):2217–2230, dec 2009.

[8] M. Barad and P. Colella. An adaptive cut-cell method for environmental fluid mechanics. *International Journal for Numerical Methods in Fluids*, 60(October 2008):473–514, 2009.

[9] M. Barad, P. Colella, D. Graves, T. Ligocki, D. Modiano, P. Schwartz, and B. Van Straalen. EBChombo Software Package for Cartesian Grid, Embedded Boundary Applications. Technical report, Technical report LBNL-6615E, Lawrence Berkeley National Laboratory, 2000.

[10] J. Barber, C. Bose, A. Bourlioux, J. Braun, E. Brunelle, T. Garcia, T. Hillen, C. Lam, B. Ong, and C. Pöschl. PROMETHEUS - Canada's Wildfire Growth Simulator. Technical report, 2007.

[11] H. Baum and B. McCaffrey. Fire induced flow field–theory and experiment. *Proceedings of the Second International Symposium*, pages 129–148, 1989.

[12] H. Baum, K. Mcgrattan, and R. Rehm. Three Dimensional Simulations Of Fire Plume Dynamics. *Fire Safety Science*, 5:511–522, 1997.

[13] H. R. Baum. Modeling and scaling laws for large fires. In *Progress in Scale Modeling*, pages 39–60. Springer, 2008.

[14] J. Beezley, A. Kochanski, V. Kondratenko, J. Mandel, and B. Sousedik. Simulation of the Meadow Creek fire using WRF-Fire. In *AGU Fall Meeting Abstracts*, volume 1, page 1478, 2010.

[15] J. D. Beezley, S. Chakraborty, J. L. Coen, C. C. Douglas, J. Mandel, A. Vodacek, and Z. Wang. Real-time data driven wildland fire modeling. In *International Conference on Computational Science*, pages 46–53. Springer, 2008.

[16] J. M. Canfield, R. R. Linn, J. A. Sauer, M. Finney, and J. Forthofer. A numerical investigation of the interplay between fireline length, geometry, and rate of spread. *Agricultural and Forest Meteorology*, 189-190:48–59, 2014.

[17] T. Clark, J. Coen, and D. Latham. Description of a coupled atmosphere–fire model. *International Journal of Wildland Fire*, pages 49–63, 2004.

[18] T. Clark and W. Hall. The design of smooth, conservative vertical grids for interactive grid nesting with stretching. *Journal of Applied Meteorology*, 35:1040–1048, 1996.

[19] T. Clark, M. Jenkins, J. Coen, and D. Packham. A coupled atmosphere-fire model: Convective feedback on fire-line dynamics. *Journal of Applied Meteorology*, 35(6):875–901, 1996.

[20] T. Clark, M. Jenkins, J. Coen, and D. Packham. A Coupled Atmosphere-Fire Model: Role of the Convective Froude Number and Dynamic Fingering at the Fireline. *International Journal of Wildland Fire*, 6(4):177, 1996.

[21] J. Coen. Simulation of the Big Elk Fire using coupled atmosphere–fire modeling. *International Journal of Wildland Fire*, 14(1):49–59, 2005.

[22] J. Coen, T. Clark, and D. Latham. Coupled atmosphere-fire model simulations in various fuel types in complex terrain. In *Fourth Symposium on Fire and Forest Meteorology*, pages 1–4, 2001.

[23] J. Coen and P. Riggan. Landscape-Scale Wildland Fire Modeling: Research & Applications. *knowledgeweb.afac.com.au*, 2, 2006.

[24] J. L. Coen, M. Cameron, J. Michalakes, E. G. Patton, P. J. Riggan, and K. M. Yedinak. WRF-fire: Coupled weather-wildland fire modeling with the weather research and forecasting model. *Journal of Applied Meteorology and Climatology*, 52(1):16–38, 2013.

[25] J. L. Coen and W. Schroeder. Use of spatially refined satellite remote sensing fire detection data to initialize and evaluate coupled weather-wildfire growth model simulations. *Geophysical Research Letters*, 40(20):5536–5541, 2013.

[26] J. L. Coen and W. Schroeder. The High Park fire: Coupled weather-wildland fire model simulation of a windstorm-driven wildfire in Colorado's Front Range. *Journal of Geophysical Research: Atmospheres*, 120(1):131–146, jan 2015.

[27] P. Colella, D. Graves, T. Ligocki, D. Martin, D. Modiano, D. Serafini, and B. Van Straalen. Chombo software package for AMR applications - Design document. Technical report, Technical report LBNL-6616E, Lawrence Berkeley National Laboratory, 2000.

[28] P. Cunningham, S. L. Goodrick, M. Yousuff Hussaini, and R. R. Linn. Coherent vortical structures in numerical simulations of buoyant plumes from wildland fires. *International Journal of Wildland Fire*, 14(1):61–75, 2005.

[29] P. Cunningham and R. Linn. Numerical simulations of grass fires using a coupled atmosphere-fire model: Dynamics of fire spread. *Journal of Geophysical Research*, 112(D5):1–17, mar 2007.

[30] A. Desfossés Foucault. Simulation numérique de feux de forêt avec réinitialisation et contournement d'obstacles. Master's thesis, Université de Montréal, 2010.

[31] A. Desfossés Foucault. *Méthodes rapides et efficaces pour résolution numérique d'équations de type Hamilton-Jacobi avec application à la simulation de feux de forêt.* PhD thesis, Université de Montréal, 2015.

[32] J. Dold. Flow attachment in eruptive fire growth. In *Proceedings of the 6th International Conference on Forest Fire Research. Portugal*, 2010.

[33] J. Dold. Vegetation engagement in unsteady fire spread. In *Proceedings of 6th International Conference on Forest Fire Research. Portugal*, 2010.

[34] J. Dold. Fire spread near the attached and separated flow transition, including surge and stall behaviour. 2011.

[35] J. Dold, G. Sivashinsky, and R. Weber. Onset of flow-induced fingering in bushfires. (July):177–180, 2010.

[36] J. Dold, A. Zinoviev, and E. Leslie. Intensity accumulation in unsteady firelines: A simple model for vegetation engagement. *Fire Safety Journal*, 46(1-2):63–69, 2011.

[37] J. Dold, A. Zinoviev, and R. Weber. Nonlocal flow effects in bushfire spread rates. *Forest Ecology and Management*, 234:S93, nov 2006.

[38] J. W. Dold and a. Zinoviev. Fire eruption through intensity and spread rate interaction mediated by flow attachment. *Combustion Theory and Modelling*, 13(5):763–793, 2009.

[39] J. L. Dupuy, R. R. Linn, V. Konovalov, F. Pimont, J. a. Vega, and E. Jiménez. Exploring three-dimensional coupled fireatmosphere interactions downwind of wind-driven surface fires and their influence on backfires using the HIGRAD-FIRETEC model. *International Journal of Wildland Fire*, 20(6):734–750, 2011.

[40] B. Engquist, A.-K. Tornberg, and R. Tsai. Discretization of Dirac delta functions in level set methods. *Journal of Computational Physics*, 207(1):28–51, jul 2005.

[41] J. Filippi, F. Bosseur, C. Mari, C. Lac, P. Le Moigne, B. Cuenot, D. Veynante, D. Cariolle, and J.-H. Balbi. Coupled atmosphere-wildland fire modelling. *Journal of Advances in Modeling Earth Systems*, 2, oct 2009.

[42] J.-B. Filippi, F. Bosseur, X. Pialat, P.-A. Santoni, S. Strada, and C. Mari. Simulation of coupled fire/atmosphere interaction with the MesoNH-ForeFire models. *Journal of Combustion*, 2011.

[43] J.-B. Filippi, F. Morandini, J. H. Balbi, and D. R. Hill. Discrete Event Front-tracking Simulation of a Physical Fire-spread Model. *Simulation*, 86(10):629–646, aug 2009.

[44] M. A. Finney, D. Q. Ã, M. Alexander, P. Andrews, J. Beck, B. Keane, and J. Scott. FARSITE : Fire Area Simulator — Model Development and Evaluation. *Evaluation*, Research P(March):47, 1998.

[45] M. A. Finney, J. D. Cohen, J. M. Forthofer, S. S. McAllister, M. J. Gollner, D. J. Gorham, K. Saito, N. K. Akafuah, B. A. Adam, and J. D. English. Role of buoyant flame dynamics in wildfire spread. *Proceedings of the National Academy of Sciences*, 112(32):9833–9838, aug 2015.

[46] Forestry Canada Fire Danger Group. Development and structure of the Canadian forest fire behaviour prediction system. Technical report, 1992.

[47] J. Forthofer. Modeling wind in complex terrain for use in fire spread prediction. Master's thesis, Colorado State University Fort Collins, 2007.

[48] J. M. Forthofer and S. L. Goodrick. Review of vortices in wildland fire. *Journal of Combustion*, 2011(Figure 1), 2011.

[49] J. Hilditch and P. Colella. A projection method for low Mach number fast chemistry reacting flow. In *35th Aerospace Sciences Meeting and Exhibit*, page 263, 1997.

[50] K. G. Hirsch et al. *Canadian forest fire behavior prediction (FBP) system: user's guide*, volume 7. 1996.

[51] B. Hosseini, N. Nigam, and J. M. Stockie. On regularizations of the Dirac delta distribution. *Journal of Computational Physics*, 305:423–447, 2016.

[52] H. Johansen. A Cartesian Grid Embedded Boundary Method for Poisson's Equation on Irregular Domains. *Journal of Computational Physics*, 147(1):60–85, nov 1998.

[53] W. M. Jolly, M. A. Cochrane, P. H. Freeborn, Z. A. Holden, T. J. Brown, G. J. Williamson, and D. M. Bowman. Climate-induced variations in global wildfire danger from 1979 to 2013. *Nature communications*, 6, 2015.

[54] J. P. Lafore, J. Stein, M. I. Asensio, P. Bougeault, V. Ducrocq, J. Duron, C. Fischer, P. Héreil, P. Mascart, V. Masson, J. P. Pinty, J. L. Redelsperger, E. Richard, and J. Vilà-Guerau de Arellano. The Meso-NH Atmospheric Simulation System. Part I: adiabatic formulation and control simulations. *Annales Geophysicae*, 16(1):90–109, 1998.

[55] M. Lai. *A projection method for reacting flow in the zero Mach number limit*. PhD thesis, University of California, Berkeley, 1993.

[56] M. Lai and J. Bell. A projection method for combustion in the zero Mach number limit. *AIAA 11th Computational Fluid*, 1993.

[57] T. J. Ligocki, P. O. Schwartz, J. Percelay, and P. Colella. Embedded boundary grid generation using the divergence theorem, implicit functions, and constructive solid geometry. *Journal of Physics: Conference Series*, 125:012080, jul 2008.

[58] R. Linn. A transport model for prediction of wildfire behavior. Technical report, Los Alamos National Lab., NM (United States), 1997.

[59] R. Linn. Numerical simulations of grass fires using a coupled atmosphere–fire model: Basic fire behavior and dependence on wind speed. *Journal of Geophysical Research*, 110(D13):1–19, 2005.

[60] R. Linn, J. Reisner, and J. Colman. Studying wildfire behavior using FIRETEC. *Journal of Wildland Fire*, 11:233–246, 2002.

[61] R. Linn, J. Winterkamp, C. Edminster, J. Colman, and W. S. Smith. Coupled influences of topography and wind on wildland fire behaviour. *International Journal of Wildland Fire*, 16(2):183, 2007.

[62] R. Linn, J. L. Winterkamp, D. R. Weise, and C. Edminster. A numerical study of slope and fuel structure effects on coupled wildfire behaviour. *International Journal of Wildland Fire*, 19(2):179, 2010.

[63] R. R. Linn, J. M. Canfield, P. Cunningham, C. Edminster, J. L. Dupuy, and F. Pimont. Using periodic line fires to gain a new perspective on multi-dimensional aspects of forward fire spread. *Agricultural and Forest Meteorology*, 157:60–76, 2012.

[64] J. Mandel, J. Beezley, and A. Kochanski. Coupled atmosphere-wildland fire modeling with WRF-Fire version 3.3. *Geoscientific Model Development Discussions*, 4(1):497–545, mar 2011.

[65] J. Mandel, J. D. Beezley, and A. K. Kochanski. An overview of the coupled atmosphere-wildland fire model WRF-Fire. *arXiv preprint arXiv:1101.5745*, 2011.

[66] J. Mandel, L. Bennethum, J. Beezley, J. Coen, C. Douglas, M. Kim, and A. Vodacek. A wildland fire model with data assimilation. *Mathematics and Computers in Simulation*, 79(3):584–606, dec 2008.

[67] MATLAB. *version 8.03.0 (R2014a)*. The MathWorks Inc., Natick, Massachusetts, 2014.

[68] A. McArthur. *Fire behaviour in eucalypt forests*. Canberra : Forestry and Timber Bureau, 1967.

[69] W. Mell, J. Charney, M. Jenkins, P. Cheney, and J. Gould. Numerical simulations of grassland fire behavior from the LANL-FIRETEC and NIST-WFDS models. In *EastFIRE Conference*, pages 11–13, 2005.

[70] W. Mell, M. A. Jenkins, J. Gould, and P. Cheney. A physics-based approach to modelling grassland fires. *International Journal of Wildland Fire*, 16(1):1–22, 2007.

[71] W. Mell, R. McDermott, and G. Forney. Wildland fire behavior modeling: perspectives, new approaches and applications. *Firescience.Gov*, page 4, 2010.

[72] R. Montenegro, A. Plaza, L. Ferragut, and M. I. Asensio. Application of a nonlinear evolution model to fire propagation. *Nonlinear Analysis*, 30(5):2873–2882, 1997.

[73] D. Morvan, C. Hoffman, F. Rego, and W. Mell. Numerical simulation of the interaction between two fire fronts in grassland and shrubland. *Fire Safety Journal*, 46(8):469–479, nov 2011.

[74] D. Morvan, S. Meradji, and W. Mell. Interaction between head fire and backfire in grasslands. *Fire Safety Journal*, 58:195–203, 2013.

[75] S. Osher, R. Fedkiw, and K. Piechor. Level Set Methods and Dynamic Implicit Surfaces. *Applied Mechanics Reviews*, 57(3):B15, 2004.

[76] G. Papadopoulos and F. Pavlidou. A Comparative Review on Wildfire Simulators. *Systems Journal, IEEE*, 5(99):1–1, 2011.

[77] M. Peace. *Coupled fire-atmosphere simulations of three Australian fires where unusual fire behaviour occurred*. PhD thesis, University of Adelaide, 2014.

[78] R. B. Pember, L. H. Howell, J. B. Bell, P. Colella, W. Y. Crutchfield, W. a. Fiveland, and J. P. Jessee. An Adaptive Projection Method for Unsteady, Low-Mach Number Combustion. *Combustion Science and Technology*, 140(1):123–168, 1998.

[79] F. Pimont, J. L. Dupuy, and R. R. Linn. Coupled slope and wind effects on fire spread with influences of fire size: A numerical study using FIRETEC. *International Journal of Wildland Fire*, 21(7):828–842, 2012.

[80] F. Pimont, J.-L. Dupuy, R. R. Linn, and S. Dupont. Impacts of tree canopy structure on wind flows and fire propagation simulated with FIRETEC. *Annals of Forest Science*, 68(3):523–530, apr 2011.

[81] L.-X. Proulx. Approche cartésienne pour le calcul du vent en terrain complexe avec application à la propagation des feux de forêt. Master's thesis, Université de Montréal, 2011.

[82] L.-X. Proulx. A Novel Coupled Fire-Atmosphere Model for the Forecast of Forest Fire Spread. Unpublished manuscript, 2016.

[83] L.-X. Proulx. Regularization of a Singular Source on a Codimension-2 Manifold for a Coupled Fire-Atmosphere Model. Unpublished Manuscript, 2016.

[84] R. Rehm. The effects of winds from burning structures on ground-fire propagation at the wildland-urban interface. *Combustion Theory and Modelling*, 12(3):1–20, 2008.

[85] R. Rehm and H. Baum. The Equations of Motion for Thermally Driven , Buoya nt Flows. *Journal Of Research Of The National Bureau Of Standards*, 8(3):297–308, 1978.

[86] J. Reisner and J. Bossert. Numerical simulations of two wildfire events using a combined modeling system (HIGRAD/BEHAVE). *Earth*, 836, 1997.

[87] G. D. Richards. The Properties of Elliptical Wildfire Growth for Time Dependent Fuel and Meteorological Conditions. *Combustion Science and Technology*, 95(1-6):357–383, 1993.

[88] R. Rothermel. A mathematical model for predicting fire spread in wildland fuels. *USDA Forest Service Research Paper INT USA*, 1972.

[89] P. Schwartz, M. Barad, P. Colella, and T. Ligocki. A Cartesian grid embedded boundary method for the heat equation and Poisson's equation in three dimensions. *Journal of Computational Physics*, 211(2):531–550, jan 2006.

[90] J. Sethian. *Level set methods and fast marching methods: evolving interfaces in computational geometry, fluid mechanics, computer vision, and materials science*. Cambridge University Press, 1999.

[91] J. Sharples, C. Simpson, and J. Evans. Examination of wind speed thresholds for vorticity-driven lateral fire spread. In *20th International Congress of Modelling and Simulation*, volume 3, 2013.

[92] C. C. Simpson, J. J. Sharples, and J. P. Evans. Resolving vorticity-driven lateral fire spread using the WRF-Fire coupled atmosphere&amp ;ndash ;fire numerical model. *Natural Hazards and Earth System Science*, 14(9):2359–2371, sep 2014.

[93] W. C. Skamarock, J. B. Klemp, J. Dudhia, D. O. Gill, D. M. Barker, W. Wang, and J. G. Powers. A description of the advanced research wrf version 2. Technical report, National Center For Atmospheric Research Boulder Co Mesoscale and Microscale Meteorology Div, 2005.

[94] P. Smereka. The numerical approximation of a delta function with application to level set methods. *Journal of Computational Physics*, 211(1):77–90, jan 2006.

[95] A. Sullivan. Convective Froude number and Byram's energy criterion of Australian experimental grassland fires. *Proceedings of the Combustion Institute*, 31(2):2557–2564, jan 2007.

[96] A. L. Sullivan. A review of wildland fire spread modelling, 1990-present, 1: Physical and quasi-physical models. *Sciences-New York*, page 31, jun 2007.

[97] A. L. Sullivan. A review of wildland fire spread modelling, 1990-present 2: Empirical and quasi-empirical models. *Behaviour*, page 22, jun 2007.

[98] A. L. Sullivan. A review of wildland fire spread modelling, 1990-present 3: Mathematical analogues and simulation models. *Engineering*, page 20, jun 2007.

[99] R. Sun, M. Jenkins, S. K. Krueger, W. Mell, and J. Charney. An evaluation of fire-plume properties simulated with the Fire Dynamics Simulator (FDS) and the Clark coupled wildfire model. *Canadian Journal of Forest Research*, 36(11):2894–2908, nov 2006.

[100] R. Sun, S. K. Krueger, M. Jenkins, M. a. Zulauf, and J. Charney. The importance of fire–atmosphere coupling and boundary-layer turbulence to wildfire spread. *International Journal of Wildland Fire*, 18(1):50, 2009.

[101] M. Sussman, P. Smereka, and S. Osher. A level set approach for computing solutions to incompressible two-phase flow. *Journal of Computational Physics*, 114:146–159, 1994.

[102] A.-K. Tornberg. Multi-dimensional quadrature of singular and discontinuous functions. *BIT Numerical Mathematics*, 42(3):644–669, 2002.

[103] A.-K. Tornberg and B. Engquist. Regularization Techniques for Numerical Approximation of PDEs with Singularities. *Journal of Scientific Computing*, 19(1-3):527–552, 2003.

[104] A.-K. Tornberg and B. Engquist. Numerical approximations of singular source terms in differential equations. *Journal of Computational Physics*, 200(2):462–488, nov 2004.

[105] J. D. Towers. Two methods for discretizing a delta function supported on a level set. *Journal of Computational Physics*, 220(2):915–931, jan 2007.

[106] J. D. Towers. Discretizing delta functions via finite differences and gradient normalization. *Journal of Computational Physics*, 228(10):3816–3836, 2009.

[107] J. Trelles. *Mass fire modeling of the 20 October 1991 Oakland Hills fire*. PhD thesis, University of California, Berkeley, 1995.

[108] J. Trelles, K. McGrattan, and H. Baum. Smoke Dispersion from Multiple Fire Plumes. *AIAA Journal*, 37(12):1588–1601, 1999.

[109] J. Trelles, K. B. McGrattan, and H. R. Baum. Smoke transport by sheared. *Combustion Theory and Modelling*, 3:323–341, 1999.

[110] J. Trelles and P. Pagni. A Practical Scheme for Calculating the Fire-Induced Winds in the October 20, 1991 Oakland Hills Fire. In *Fire Research and Safety. 12th Joint Panel Meeting*, pages 297–305, 1992.

[111] J. Trelles and P. Pagni. Fire-induced winds in the 20 October 1991 Oakland Hills fire. In *Fire Safety Science-Proceedings of the Fifth International Symposium*, pages 911–922. International Association for Fire Safety Science, 1997.

[112] C. Tymstra, R. Bryce, B. Wotton, S. Taylor, O. Armitage, et al. Development and structure of Prometheus: the Canadian wildland fire growth simulation model. Technical report, Natural Resources Canada, Canadian Forest Service, Northern Forestry Centre, Information Report NOR-X-417.(Edmonton, AB), 2010.

[113] D. Viegas et al. A mathematical model for forest fires blowup. *Combustion Science and Technology*, 177(1):27–51, 2005.

[114] P. A. Werth, B. E. Potter, C. B. Clements, M. Finney, S. L. Goodrick, M. E. Alexander, M. G. Cruz, J. A. Forthofer, S. S. McAllister, et al. Synthesis of knowledge of extreme fire behavior: volume 1 for fire managers. *Gen. Tech. Rep. PNW-GTR-854. Portland, OR: US Department of Agriculture, Forest Service, Pacific Northwest Research Station. 144 p.*, 2011.

[115] S. Zahedi and A.-K. Tornberg. Delta function approximations in level set methods by distance function extension. *Journal of Computational Physics*, 229(6):2199–2219, mar 2010.

[116] Z. Zhang and X. Zheng. The representation of line Dirac delta function along a space curve. *arXiv preprint arXiv:1209.3221*, 2012.

Annexe A

ÉQUATIONS PRIMITIVES EN SCIENCES DE L'ATMOSPHÈRE

Les équations primitives sont les équations météorologiques hydrostatiques sous l'approximation traditionnelle. Elles regroupent dans l'ordre ; l'équation de la conservation de la quantité de mouvement, la relation hydrostatique, l'équation thermodynamique, l'équation pour la conservation de la masse, l'équation pour le rapport de mélange et la relation des gaz (équation de fermeture).

$$\frac{D\mathbf{V}_h}{Dt} + f\mathbf{k}\times\mathbf{V}_h + \frac{1}{\rho}\nabla_h p = F_h \tag{A.0.1}$$

$$\frac{\partial p}{\partial z} + \rho g = 0 \tag{A.0.2}$$

$$C_p\frac{DT}{Dt} - \frac{1}{\rho}\frac{Dp}{Dt} = Q \tag{A.0.3}$$

$$\frac{D\rho}{Dt} + \rho\nabla\cdot\mathbf{V} = 0 \tag{A.0.4}$$

$$\frac{Dr}{Dt} = S_r \tag{A.0.5}$$

$$p = \rho RT \tag{A.0.6}$$

où $\mathbf{V} = (u, v, w)$, $\mathbf{V}_h = (u, v, 0)$, D/Dt est la dérivée matérielle, f est le paramètre de Coriolis, F_h sont les forces agissant dans le plan horizontal, C_p est la chaleur spécifique à pression constante, Q est le taux de réchauffement diabatique (radiation terrestre, chaleur latente, diffusion/conduction thermique), $r = \rho_v/\rho_a$ est le rapport de mélange de vapeur d'eau à l'air sec, $S_r = S_{\rho_v}/\rho_a$ avec S_{ρ_v} comme terme source de vapeur d'eau et R est la constante de gaz de l'air sec.

Annexe B

GLOSSAIRE

Conduction thermique: Transfert d'énergie avec contact quand il existe un gradient de température (variation progressive de la température) au sein d'un système.

Convection thermique: Transfert de chaleur d'un endroit à un autre dû au mouvement d'un fluide.

Chaleur latente: Quantité de chaleur émise ou absorbée par un corps durant un changement de phase sans qu'il y ait un changement de température. En météorologie, le flux de chaleur latente est le flux de chaleur de la surface de la Terre vers l'atmosphère associé à l'évaporation ou la transpiration végétale et la condensation subséquente de la vapeur d'eau dans la troposphère. C'est une quantité importante dans le bilan énergétique de la surface planétaire.

Chaleur sensible: Quantité de chaleur qui est échangée, sans transition de phase physique, entre deux corps formant un système isolé. Cet échange de chaleur change la température d'un corps, effet qui peut être ressenti ou mesuré par un observateur.

Couche limite planétaire: Partie de l'atmosphère dans laquelle l'écoulement est fortement influencé par son interaction avec la surface de la planète. Cette couche est caractérisée par la turbulence et des variations spatiales et temporelles à des échelles beaucoup plus petites que celles résolues par les réseaux météorologiques. La profondeur de cette couche peut varier de 30 m dans des conditions de grande stabilité statique à plus de 3 km dans des conditions où la convection est importante. Pour des conditions moyennes aux latitudes moyennes, la couche limite planétaire s'étend dans le premier kilomètre près de la surface.

Équilibre hydrostatique: État en mécanique des fluides où un volume de fluide est au repos ou à vitesse constante. Cet état survient lorsque la force de gravitation est contrebalancée par la force du gradient de pression. En météorologie, l'approximation hydrostatique permet de négliger, dans le calcul de la pression le long de l'axe vertical, les forces dues au mouvement horizontal ou vertical de l'air et à la force de Coriolis. Cette approximation est valide à un grand degré de précision pour un très grand nombre de phénomènes naturels de l'atmosphère, plus précisément pour les mouvements de grande échelle.

Méso-échelle: Ce terme décrit les phénomènes qui se passent à une échelle plus petite que l'échelle synoptique, celui de la circulation atmosphérique générale, mais plus grande que celui des nuages individuels traités par la micro-échelle. Les dimensions horizontales varient entre quelques kilomètres et plusieurs centaines de kilomètres.

Pyrolyse: La première réaction chimique à survenir dans la décomposition d'un combustible solide organique par la chaleur.

Rayonnement thermique: Énergie émise par la matière comme des ondes électromagnétiques. Toute matière avec une température au-dessus du zéro absolu émet une radiation thermique. Cette radiation se propage sans la présence de matière à travers le vide.

Synoptique: L'échelle synoptique est caractérisée par des phénomènes atmosphériques se développant sur une longueur de plusieurs centaines à plusieurs milliers de kilomètres et sur une durée de plusieurs jours. Les systèmes dépressionnaires et les anticyclones en Amérique du Nord se retrouvent à cette échelle.

Température potentielle: Température acquise par une parcelle de fluide à une pression P si elle était amenée adiabatiquement vers un niveau de pression standard P_0. Dans le cas de l'atmosphère, le calcul est effectué afin de trouver la température qu'aurait la parcelle d'air à la pression de 1000 hPa, pression près de la normale à la surface de la Terre. La température potentielle θ est donnée par

$$\theta = T\left(\frac{P_0}{P}\right)^{R/C_p} \tag{B.0.7}$$

où T est la température absolue (en Kelvin) de la parcelle, R est la constante des gaz parfaits pour l'air et C_p la chaleur massique à pression constante de l'air.

Température thermodynamique: Mesure absolue de la température et principal paramètre de la thermodynamique.